UCLA
UCLA Electronic Theses and Dissertations

Title
THz Imaging of the Cornea for Early Detection of Diseases

Permalink
https://escholarship.org/uc/item/9qm2f5dz

Author
Hu, Yong

Publication Date
2018

Peer reviewed|Thesis/dissertation

eScholarship.org Powered by the California Digital Library
University of California

UNIVERSITY OF CALIFORNIA

Los Angeles

THz Imaging of the Cornea for Early

Detection of Diseases

A dissertation submitted in partial satisfaction of

the requirements for the degree Doctor of Philosophy

in Bioengineering

by

Yong HU

2018

© Copyright by

Yong HU

ABSTRACT OF THE DISSERTATION

THz Imaging of the Cornea for Early Detection of Diseases

by

Yong HU

Doctor of Philosophy in Bioengineering
University of California, Los Angeles, 2018
Professor Warren Grundfest, Chair

With the development of Terahertz (THz) sources and detectors, the non-destructive scanning and imaging technique has gain popularity from various fields of applications, from astronomical sciences to product quality inspection, from security and defense applications to pharmaceutical and biomedical applications. Because of its sensitivity to polar molecules, like water, non-ionizing effect and moderate spatial resolution, THz imaging has drawn great attention from medical field, especially in mapping water distribution and migration in physiological tissues.

Given cornea's low physiologic variation and homogenous composition when compared to other tissue systems in the human body and its easy access with free-space THz beams, corneal tissue water content (CTWC) evaluation with THz waves becomes interesting and popular. As ongoing clinical studies show, a lot of corneal diseases and vision problems are accompanied with abnormal CTWC, appearing as swelling of eyes and blurring of vision, etc. A considerable amount of people all around the world are suffering from different types of corneal diseases. Fuch's endothelial dystrophy, for example, is affecting around 4% of population who are over 40 years old in the US. As endothelium begins to fail, cornea will get hyper hydrated and impair

vision. Late identifications usually requires surgery. Failure of corneal transplant is also believed to be preceded with edema, which means the abnormal CTWC. This makes CTWC mapping an attractive method for doctors to diagnose corneal diseases with. The lack of accurate, non-invasive tool for direct measurement of CTWC opens a great opportunity for THz imaging.

Based on the group's previous efforts, this thesis aims to develop a proof of concept of rapid scanning THz imaging system for CTWC measurement for study and early evaluation of corneal diseases. In this thesis, it details the modeling of cornea-THz interaction, optics design, system instrumentation, preliminary imaging and system analysis/characterization.

First, a classical electromagnetic model of multi-layer dielectric slabs were adopted for cornea-THz interaction. Observed the reflective signal response based on variations of CTWC and corneal central thickness (CCT) with sources centered at 100 GHz and 525 GHz respectively. Also explored the possibility of more accurate measurement combining magnitude and phase detection.

Second, explored the strengths and weaknesses of imaging with OAPs and found ways to use OAPs correctly. Based on this, the optics setup of a non-contact angular scanning imaging system was designed and fully simulated with ASAP. Much better image quality was achieved with this system compared to the previous system built by the group. Approaches of quasioptics, physical optics and Gaussian beam propagation method were used independently for analysis of the system and had a good agreement with each other.

Based on the optics design, a functioning THz imaging system was implemented afterwards. The electronic schematic of illumination source, detector, preliminary signal processing and data acquisition were explained. Carefully detailed mechanical design, machining and assembling of the system guaranteed the system to run as expected. Custom designed graphic user interface (GUI) enabled operators to control the system and acquire images with ease and efficiency.

System imaging quality and speed limit were characterized with preliminary images. The

coupling efficiency of the system were characterized with a brass ball and verified our previous simulation results, proved the system has a homogenous energy coupling efficiency across the effective field of view (FOV). Images with strips-attached brass balls and knife-edge measurement with hemisphere target ball characterized the spatial resolution to be around 1.3 mm with little distortion, agreed well with the predication made via different simulations. Images of cornea phantoms showed the capability of the system to identify abnormal geometry and water migration within the phantoms. The mechanical speed limit of the current system is 8 seconds per image and could be sped up to 1.3 seconds per frame with optimized motion pattern. The electronic setup is limiting the system's speed to 10 seconds per frame with fine resolution. We believe this optical setup will be able to provide images at video rate with better mechanical and electronic equipment in the future.

The dissertation of Yong HU is approved.

Maie A.R. St. John

Sophie X. Deng

Oscar M. Stafsudd

Zachary Deis Taylor

Warren Grundfest, Committee Chair

University of California, Los Angeles

2018

This dissertation is dedicated to my loving parents and older sisters. Your unwavering support and encouragement made this work possible. Thank you for believing in me.

TABLE OF CONTENTS

ABSTRACT OF THE DISSERTATION ii
TABLE OF CONTENTS vii
LIST OF FIGURES x
ACKNOWLEDGEMENTS xii
BIOGRAPHY xiv
CHAPTER 1: TERAHERTZ TECHNOLOGY BACKGROUND 1
1.1 Bridged Terahertz Gap 1
1.1.1 Terahertz Sources 1
1.1.2 Terahertz Detectors 3
1.2 Terahertz Systems 5
1.2.1 Passive vs Active 5
1.2.2 Time Domain vs Frequency Domain 6
1.2.3 Development of THz Detector Arrays 8
1.3 Terahertz Applications 9
1.4 Conclusion 11
CHAPTER 2: CLINIC BACKGROUND 12
2.1 Anatomy of the cornea 12
2.2 Related Diseases 14
2.3 Measurement Limitations 16
2.3.1 Central Corneal Thickness (CCT) Measurements 16
2.3.2 Mapping From CCT to CTWC 17
2.4 Opportunity for THz Imaging 20
CHAPTER 3: BACKGROUND WORK 21
3.1 In-vivo Animal Experiment 21
3.1.1 System Setup 21
3.1.2 Animal Experiment Design 23
3.1.3 Animal Data 24
3.1.4 Analysis 25
3.1.5 Discussion 26
3.2 Rectilinear Scanning System 27
3.2.1 Geometry of Human Cornea 27
3.2.2 Design Principles 29
3.2.3 System Setup 30
3.2.4 Imaging Data 32
3.2.5 Discussion 33
3.3 Conclusion 34
CHAPTER 4: EM MODELING OF CORNEA-THZ INTERACTION 35
4.1 Stratified Cornea Model 35
4.1.1 Assignment of Tissue Properties 35
4.1.2 Stratified Model Overview 36
4.2 Reflectivity with Different Sources 37
4.2.1 Source Setup 38
4.2.2 CTWC Distribution Profile 39
4.3 General Observation 41

4.4 Phase Detection Possibilities 46
4.5 Chalmers' work 49
4.5.1 Experiment setup 49
4.5.2 Results and Problems 50
4.5.3 New testing system for Chalmers 51
CHAPTER 5: THz Optics Design 53
5.1 Off-Axis Parabolic Mirrors 53
5.2 Beam Center Shift and Compensation 55
5.2.1 Single OAP System 55
5.2.2 Double OAP System 56
5.2.3 Compensated vs Uncompensated Complex Systems 57
5.3 Focal Length Influence on Imaging Behavior 62
5.3.1 Comparison On Different EFL Combinations 62
5.3.2 Depth of Field and Knife-Edge Measurement 65
5.4 Angular Scanning System Design 66
5.4.1 Design of Angular Scanning System 66
5.4.2 Simulation of Angular Scanning System 69
5.4.3 Comparison with Rectilinear Scanning System 71
5.5 Speed Estimation from Mechanical Point of View 73
CHAPTER 6: SYSTEM ANALYSIS 74
6.1 Quasioptical Analysis 74
6.1.1 Problem Setup 74
6.1.2 Quasioptical Computation: Spot Size 77
6.1.3 Quasioptical Computation: Coupling Coefficient 78
6.1.4 Quasioptical Computation: Radius of Curvature 78
6.2 Physical Optics Analysis 79
6.2.1 Physical Optics: Spot Size 79
6.2.2 Physical Optics: Coupling Efficiency 80
6.3 Gaussian beam propagation 82
6.4 Alignment Sensitivity Analysis 85
CHAPTER 7: SYSTEM INSTRUMENTATION 88
7.1 System Overview 88
7.2 THz source and Detector Setup 90
7.2.1 Source Setup 90
7.2.2 Detector 92
7.3 Mechanical Design of the System 93
7.3.1 Overview Design 93
7.3.2 Rotating Mirror Assembly 95
7.3.3 Linear Motion 97
7.3.4 System Assembling and Optical Elements Alignment 99
7.4 Rotary Motor Motion Control 102
7.5 Graphic User Interface (GUI) Design 103
CHAPTER 8: IMAGING FOR CHARACTERIZATION 105
8.1 Coupling Efficiency Characterization 105
8.1.1 System Setup 105
8.1.2 Imaging Results 106

8.1.3 Analysis 107
8.2 Spatial Resolution Characterization 109
8.2.1 Setup and Imaging Results 109
8.2.2 Analysis 110
8.3 Corneal Phantom Imaging 111
8.3.1 Setup and Imaging and Results 111
8.3.2 Analysis 113
8.4 Speed Estimation 114
8.4.1 Mechanical Limit 114
8.4.2 Electronical Limit 115
CHAPTER 9: CONCLUSION AND FUTURE WORK 117
9.1 Conclusions 117
9.2 Future Work 119
9.2.1 Speeding Up Further 119
9.2.2 Clinical Trials 119
9.2.3 Phase Detection 120
9.3 Final Words 121

LIST OF FIGURES

Figure 1. Natural sources of THz radiation 6
Figure 2. a) Typical terahertz pulse used in a time domain system; (b) Typical schematic of a time domain system setup 7
Figure 3. The anatomy of the human eye 12
Figure 4. Light micrograph of corneal layers 13
Figure 5. Comparison between healthy eye and diseased eyes. 15
Figure 6. A cross section of a recipient cornea with an attached posterior disc by anterior optical coherence tomography (AC-OCT). 17
Figure 7. CTWC and corneal thickness relationship. 18
Figure 8. Molecular modes and activity in the terahertz region of the electromagnetic spectrum 20
Figure 9. (a) Block diagram of 100 GHz sensing system. (b) Illumination geometry. 21
Figure 10. (a) Block diagram of 525 GHz sensing system. (b) Illumination geometry. 22
Figure 11. Flow chart of experiment procedure 23
Figure 12. How the rabbit was secured in place for measurement. 24
Figure 13. (a) Correlation between central thickness and millimeter wave signal; (b) Correlation between central thickness and THz signal. 24
Figure 14. Simulated reflectivity for mm wave and THz signals under three scenarios. 25
Figure 15. Decentration and astigmatism in corneal anatomy. 27
Figure 16. Influence of diseases on ROC deviation. 28
Figure 17. Scanning principle of the cornea using an OAP. 29
Figure 18. Complete optical setup of the rectilinear scanning system. 30
Figure 19. The developer is testing the rectilinear scanning system. 31
Figure 20. Images of different target balls for demonstration. 32
Figure 21. The imaged area of the eye and a typical image of the volunteer's eye. 33
Figure 22. Stratified model for cornea with depth dependent water content variation 37
Figure 23. E-field penetration into the corneal tissue at 100 GHz and 650 GHz. 37
Figure 24. Predefined EM source. 39
Figure 25. CTWC gradient models set for pinned front, pinned back and global model. 39
Figure 26. Reflectivity simulation of the cornea over different depth and water content at 100GHz 41
Figure 27. Replotted simulation with constant CCT and CTWC at 100 GHz 42
Figure 28. Reflectivity simulation of the cornea over different depth and water content at 525 GHz 43
Figure 29. Replotted simulation with constant CCT and CTWC at 525 GHz 44
Figure 30. Isotropic and gradient CTWC change with time. 46
Figure 31. Frequency response with different variation models 47
Figure 32. Detailed plot of the "Turning point" 48
Figure 33. Measurement setup in Chalmers' lab. 49
Figure 34. Measurement results of the frequency response with plastic backing. 50
Figure 35. Design of the new testing system for CUT. 51
Figure 36. Backing setup to mimic the aqueous humor of the eye. 52
Figure 37. OAP mirrors 53
Figure 38. Reflection of a Gaussian beam from an OAP 54

Figure 39. Demonstration of center shift of Gaussian beam from OAP 55
Figure 40. Two-OAP system beam center shift demo 57
Figure 41. Compensated VS uncompensated complex systems 58
Figure 42. Detector plane image comparison while aligned 59
Figure 43. Dynamic comparison while displacing imaging plane 61
Figure 44. Comparison panel with parameter legend 62
Figure 45. Aligned simulation results for different EFL comparison 63
Figure 46. Displaced simulation results for different EFL comparison 64
Figure 47. Experiment measurement of real system 65
Figure 48. Double mirror, angular scanning imaging system design. 67
Figure 49. System reconstruction in ASAP 69
Figure 50. Simulation results on angular scanning system 70
Figure 51. Complete simulation of rectilinear scanning system 71
Figure 52. Surf plots comparison between angular scanning and rectilinear scanning systems. . 73
Figure 53. Ray path diagram of the double mirror, angular scanning system. 75
Figure 54. Quasioptical and physical optics analysis results. 76
Figure 55. Physical optics simulation results. 81
Figure 56. Target alignment sensitivity analysis 87
Figure 57. Block diagram of prototype system for THz imaging 89
Figure 58. Power supply diagram and real system setup for the oscillator with driver. 90
Figure 59. Inner diagram of the amplifier multiplier chain. 91
Figure 60. Photos of subparts of THz source. 91
Figure 61. Responsivity curve of WR1.5ZBD. 92
Figure 62. SolidWorks model of the optical system. 93
Figure 63. Photo of Rotary motor, RSW60C-E03. 95
Figure 64. Assembly of 2-axis rotary stage and rotating mirror. 96
Figure 65. Holding frame for the rotary stage. 96
Figure 66. Sub-assembly of mirror, rotary stage and its holder. 97
Figure 67. (a) Rack-mirror-target assembly; (b) Detector mounted on multifunction bridge. 98
Figure 68. Align focusing OAPs using Thorlabs cubic cage and construction rods 99
Figure 69. Readily assembled angular scanning THz imaging system. 100
Figure 70. Connection schematic for LabJack Figure 70and X-MCB2. 102
Figure 71. GUI for the angular scanning THz imaging system 103
Figure 74. Mounting the target ball. 105
Figure 73. Imaging of a brass characterization ball 106
Figure 76. Review of coupling efficiency simulation results 107
Figure 77. Imaging results of hemisphere target ball. 109
Figure 78. Knife-edge response measurement for hemisphere target. (a) Response measurement in θ direction; (b) Response measurement in φ direction. 110
Figure 79. Review of spot size simulation results. 111
Figure 80. Visual image of the corneal phantom imaged. 111
Figure 81. Images of corneal phantom. 112
Figure 82. Comparison of imaging results under different scanning speed. 115

ACKNOWLEDGEMENTS

First of all, I'd like to thank my supervisors, Prof. Warren Grundfest and Prof. Zachary Taylor. Professor Grundfest provided me the great chance working in THz imaging. He trusted me and let me explore in the wide scope of THz imaging without restrictions in the beginning years and linked me up with the right people and resources for my research. The outstanding expertise and thoughtful instructions of Professor Taylor guided me into this fantastic THz imaging world. The 2-3 months' working experience in his house had been the most productive period of my PhD career and this good memory will last forever. I'm also grateful for his remote instructions even after he moved to Finland. Again, I'm so privileged to have learnt from their vision, expertise and the way they behave, and this will be a lifetime treasure for me.

I was very lucky to have a fantastic committee. Prof. Deng's crucial input from a medical scientist's point of view helped shape the project to its current stage. Prof. Stafsudd's expertise in optics and wave electronics, Dr. St. John and Prof. Ennis's guidance in medical imaging and clinical experiments were all tremendous help in finishing my research project and getting the PhD degree. I'm deeply grateful for them.

I thank Prof. Elliott Brown in Wright State University for having me studying and testing THz sources in his lab for half a month; and also thank Prof. Ben Wu and Prof. William Kaiser for having me doing research in their lab for a year and supporting me pursuing my own research interests outside the lab.

I gratefully acknowledge the former members of Terahertz team and all the members in Prof. Gundfest's lab. For all the names I've heard of but not all of whom I had the luck to meet in person, David Bennett, Priyamvada Tewari, James Garritano, Bryan Nowroozi, Neha Bajwa and Shijun Sung, I'm really grateful for the ground work they have set for me. Without them, my work wouldn't be possible. I also thank for the insightful discussions and good times with all the other lab members, George, Nathan, Will, Jason, Rory, Harrison. And my thanks also go to the

undergrads worked or working in the lab.

It was great luck to meet Rory and Jessica when we first started at UCLA. We supported each other, enjoyed happiness, shared sorrows together and now we are all about to graduate. I truly thank you guys. All the time we spent together made the days at UCLA brighter. The friendship will last forever.

My special thanks and deep love to my parents who raised me up and supported me pursuing my dreams overseas. Their love and care are being felt every minute even thousands of miles away. My deep love to my dear sisters, who always share my feelings and support me since I remember things. Without you, my life will be totally different. And my great thanks and love to my girlfriend, Chen, who accompanied me through the toughest days.

I also wish to thank many other people whose names are not mentioned here but this does not mean that I have forgotten their help.

At last, great thanks to UCLA!

For the dark and bright days,

Yong HU

Dec. 12, 2018 @ UCLA, Los Angeles

BIOGRAPHY

Yong HU received his bachelor of engineering degree in Technology and Instruments for Measuring and Control from Sichuan University, Chengdu, China, in 2011, where he won the award for Outstanding Diploma Thesis. He was offered a chance to continue studying with full scholarship as a master student in Dept. of Precision Instrumentation, Tsinghua University, Beijing, China. His research was mainly on diode laser frequency stabilization and atomic magnetometers. He received his Master of Science Degree from Tsinghua University, 2014. He went on to study in Bioengineering Department, UCLA, CA, since 2014 and received his Master of Science Degree in Bioengineering. He is now a PhD candidate in Bioengineering program with particular interests in terahertz(THz) imaging for medical applications. His research focuses on the development of THz instruments for hydration level detection of tissues, especially cornea and skins. He has developed a 2 dimensional scanning system for the skins and characterized the system properties for further use, and he also developed a fast-speed rotary scanning system specifically designed for human cornea. He started from scratch, simulated the optical setup of the system, designed and manufactured the mechanical parts, built/assembled specific circuits used in the system, coded motors for automation, developed graphical interface for users for controlling and data acquisition, characterized system properties and took preliminary images with the system. He also worked on other projects, like dynamic optical contrast imaging for tissue differentiation, vibroacoustographic system for tumor identification, human posture monitor and gnathoascoustic monitor. He aims to research on new technologies and develop new instruments to meet various clinical needs, while working closely with surgeons, for better patient outcome.

CHAPTER 1: **TERAHERTZ TECHNOLOGY BACKGROUND**

1.1 Bridged Terahertz Gap

Terahertz (THz, 10^{12} Hz) radiation, also called as T rays, is electromagnetic waves whose frequency falls between infrared radiation and microwave radiation. Specifically, we refer THz waves to the electromagnetic waves with frequency from 0.1 THz to 10 THz, or loosely with the wavelength from 3 mm to 0.3 mm[1]. THz waves used to be called as “THz gap”, due to the lack of effective ways generating and detecting electromagnetic waves in this region. Thanks to the technology advancement in photonics and electronics these years, the gap has been bridged. Compact THz sources and detectors are now commercially available to scientists and technologists in various areas, ranging from medicine, chemical, biology to pharmaceutical, environmental sciences, to security and archeology [2]. This dissertation will focus on Terahertz applications for medical imaging, especially on hydration level detection of skin and cornea.

1.1.1 Terahertz Sources

Terahertz sources have two main categories: electronic sources and photonic sources. Electron beam, solid state sources and frequency multipliers are most common seen electronic terahertz sources. And the most widely used photonic sources include optoelectronic sources, semiconductor lasers and gas lasers.

Electron beam sources can generate relatively strong terahertz waves. Backward Wave Oscillators (BWO), Travelling Wave Tubes (TWT) and Gyrotrons are some representative free electron beam sources to generate terahertz waves since mid of last century. These methods are based on the interaction of strong magnetic field and high energy electron beams inside resonant cavities or waveguides. Energy transfer happens between the electron beams and magnetic fields[2][3]. High power Gyrotrons in the order of kiloWatts in the terahertz spectrum have been

reported and reviewed [4], [5]. BWOs can generate terahertz signals with moderate power level (1~100 mW) in sub-THz and terahertz region[6]–[8]. Even the output power and frequency flexibility seem attractive, the size, complexity and cost of these systems still remain big problems for most terahertz applications.

Far Infrared (FIR) gas lasers and quantum cascade lasers (QCL) are two typical THz lasers that have been developed. Gas lasers have been first investigated in the 1960s and it has experienced modest development these years. They provide tunable spectrum over 0.3 to 5 THz with the power around 100 mW[8], [9]. QCLs are relatively newly developed THz sources and have evolved rapidly. The source is capable of delivering mW level of power or higher at various frequencies from 1.2 to 5.6 THz[8], [10], [11].

Laser driven terahertz emitters, also known as terahertz photoconductive antennas (THz-PCAs), are a type of widely used terahertz source in both scientific and industrial applications. This type of sources can fall into three main categories. The first kind uses femto-second pulse laser to excite the gap between closely spaced electrodes on a photoconductor switch (like ErAs:GaAs active photoconductive layer embedded in a resonant optical-cavity structure) to generate carriers. Under the application of a biased voltage, 10~100 volts, the carriers will result in a current transient, which afterwards is coupled to an RF antenna and radiates in a wide band at terahertz frequencies[8], [12], [13]. Another type is using photomixers. In this approach, two lasers with the frequency difference in the THz range, spatially overlapped in free space or fiber, are focused onto a photoconductor with biased voltage. Photocurrent is induced under the excitation of the lasers and is also coupled to an RF antenna to emit THz waves with the laser frequency difference. This type of sources usually have a narrow spectrum and the frequency could be easily adjusted by changing the frequency difference of the lasers. [13], [14]. For above two types, the most reported power lies in the order of μW or tens of μW. There are also labs reported several mW terahertz output[15][16][17]. The third type is using femtosecond pulse lasers to excite electro-optic crystals to get terahertz radiation. In this case, higher frequency could

be obtained because of the fast response of the crystal. Power on the order of nW has been reported[8], [18], [19]. Laser driven terahertz emitters are widely used because of its availability, but the relatively low power and difficulties in laser alignment still hinder its wider applications. It is good to see some companies have their compact, easy to use products on market [20], [21].

Solid state oscillators are also used as terahertz sources. However, due to the transit time if carriers through semiconductor junctions, the frequency is always limited. Gunn and IMPATT are two representative sources widely used. These devices could be operated in room temperature to generate continuous waves with a narrow linewidth, but the power will decrease rapidly with a rate of $1/f^2$ beyond 100 GHz. Frequency multipliers are then often used to achieve higher frequency output from 200 GHz all the way up to 2.5 THz. The combination of solid state oscillator and frequency multiplier could provide relatively high power (mW level) terahertz output in a large range[8], [22]–[24]. These products have long been available on the market.

Based on the frequency range, output power, availability and cooperation with other labs, the THz sources in our lab are mainly laser driven photoconductive switches and the combination of oscillator and frequency multipliers.

1.1.2 Terahertz Detectors

The development of terahertz detectors has been by the side of terahertz sources all the time. Highly sensitive terahertz detectors have long been developed with cooling techniques. However, room temperature terahertz detectors with high sensitivity are still demanding and challenging. Here, I'm going to briefly review some of the typical detection techniques.

Thermal detectors directly measure terahertz signals by using temperature sensitive materials and converts the THz EM to measurable electrical signals. The output of thermal detectors is generally proportional to the square of the incident EM field, so they are also called square-law devices. The typical thermal detectors are Golay cells, Pyroelectric detectors and Bolometers. Golay cells absorbs the THz EM waves with infrared materials, heats up the gas in

an enclosed cavity and in turn causes the deformation of the flexible membrane of the cavity. The deformation is detected with a photodiode and a light source. Gloay cell is slow in response but it is still widely used because of its high sensitivity and room temperature using environment[18]. Other thermal detectors work in similar ways. In pyroelectric detectors, the THz EM waves changes the dielectric constant of a materials inside a voltage biased capacitor and the produces a measurable current. In bolometers, an absorber material is attached to a resistance thermal meter and converts incident radiation to measurable resistance. All the thermal detectors only measure the amplitude information and leaves out the phase information.

Another type of detectors are laser driven detectors, the counter-applications of optoelectronic sources. For the photoconductive antenna detectors, the THz EM waves and a synchronized laser incident on a voltage biased antenna and generates a photocurrent which is proportional to the amplitude of the incident THz wave. For the electro-optic detectors, the terahertz waves and a synchronized laser overlap spatially and propagate in the same direction. The THz EM wave works as a static EM field and alters the polarization state of the laser beam inside an electro-optical crystal. A quarter wave plate and polarization beam splitter are used to split the lasers into two, which are detected with a balanced detector and the induced current is proportional to the amplitude of the incident terahertz waves. By varying the relative arriving time of the THz wave and laser pulse, the phase information can also be extracted, so for the optoelectronic techniques, both the amplitude and phase information are preserved.

Heterodyne receivers amplify the input terahertz signal in a certain temporal window given by a local oscillation signal in a nonlinear mixer device such as a Schottky mixer. We call the resulted signal as intermediate frequency (IF) signal. The IF signal is then amplified, low-pass filtered and processed with following electronic setups. This type of detectors has very high sensitivity and also detect both amplitude and phase information.

In our lab, Golay cell is often used for calibrating the power of the THz sources, photoconductive antenna detector and Schottky detectors are used in different setups for different

applications. We will talk in details in our system setup chapters.

1.2 Terahertz Systems

Terahertz imaging systems have been setup using different methods, with or without a illumination source, time domain detection or frequency domain detection. Sometimes, we also talk about the system in the way how it acquire signals, one detector scanning system, 2-dimentinal array detection or the combination of both, 1-d array scanning system. No matter what implementation of the system is, the brightness of the source and the sensitivity/responsivity of the detector are always of great concern. We will talk about the different setups with these concerns in this section.

1.2.1 Passive vs Active

Electromagnetic radiation is emitted in all frequencies by all matters, and no exception for THz band radiations. The blackbody radiation theory well describes the relationship between the radiation frequency and the matter temperature. As reprinted in Figure 1 [25], THz radiation is very weak in the natural environment, but cold matters within ~10K to ~100K have most of their radiation in the THz region. This is of great interest of the astrophysics, for the cosmic background radiation has cooled down to below 3K from the very first Big Bang, and provides great opportunities for observing the universe. The fact that THz frequencies is also rich in molecular and atomic fine structures, e.g. the -CO and -OH structures, provides another great window observing the world.

Passive THz imaging images with the radiation emitted from or environment radiation reflected by an object, while active THz imaging technique detects the transmitted or scattered THz signal from an illumination source. THz passive imaging requires no expensive THz source and this makes it a great advantage over active imaging. However, because of the extremely weak signal it needs to detect, it usually has a much higher standard of sensitivity for the

detectors, which often need to work in cryogenic environment[25]. Although it is of great importance to utilize the natural emissions, especially for astronomical observations, THz illumination is more generally employed in different applications.

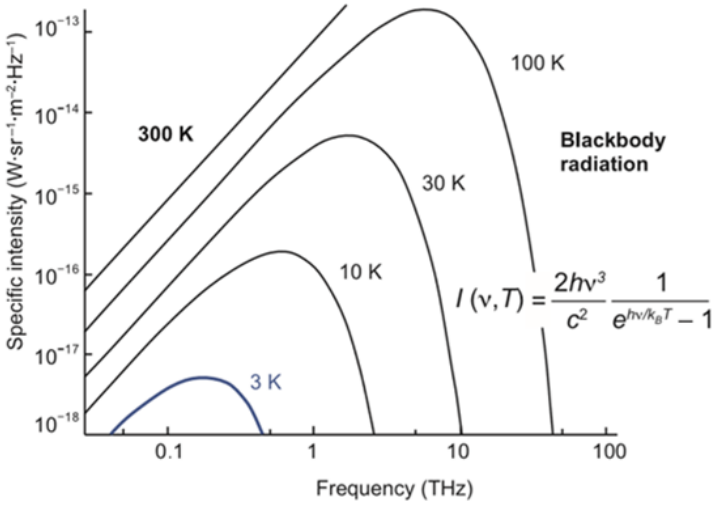

Figure 1. Natural sources of THz radiation

1.2.2 Time Domain vs Frequency Domain

Time domain and frequency domain are originally concepts borrowed from electrical engineering field. Time domain refers to analysis of functions or signals with respect to time, and frequency domain to frequency. Since terahertz waves are used a lot in spectrum analysis, naturally came out the concepts of time domain spectroscopy (TDS) and frequency domain spectroscopy (FDS). There is a common misunderstanding that thinks pulsed terahertz detection is the synonym of THz-TDS[26].

Time domain spectroscopy not only requires a pulsed source but also needs a synchronous pulse for detection. Terahertz waves stimulated with femtosecond (1 fs = 10^{-15}s) lasers, usually have a spectral span from below 100 GHz to over 5 THz. With a synchronous optically-gated detection, not only the sensitivity is orders higher but also makes the real and imaginary measurement possible at the same time. As reprinted in Figure 2 [27], in a time domain spectroscopy system, the emitter and receiver are usually identical photoconductive antennas

driven by synchronous femtosecond lasers. Laser beam from the laser is split into two, one is used to drive the emitter and generate the terahertz waves, the other beam passes through a mechanical delay line and incidents on the receiver antenna. The terahertz wave generated from the emitter travels through the optical setup, transmits through or reflects on the target, travels through the optics and shines on the receiver hence induces photocurrent. By adjusting the relative phase of the probe laser beam and the terahertz wave, the sampled photocurrent could be Fourier transformed to yield the power spectrum across the THz frequency region, hence providing the spectroscopy information of the target sample.

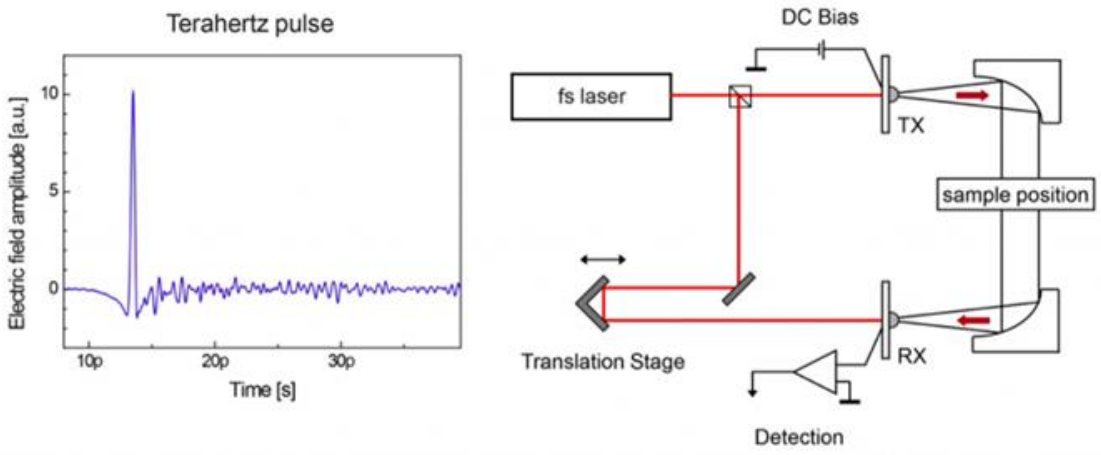

Figure 2. a) Typical terahertz pulse used in a time domain system; (b) Typical schematic of a time domain system setup

Because of the potential to provide spectroscopy information, THz-TDS has been very popular among researchers. However, due to the utilization of external delay lines and the significant time required for acquisition, the speed of THz-TDS is relatively slow. Although groups have tried using fiber-stretcher based delay lines[28], different sampling methods[28] or faster scanning system[29], time domain systems still need to be faster, especially for clinical usage.

Frequency domain spectroscopy utilizes a continuous frequency-tunable THz source to plot spectroscopy information of the target[30]. The speed of measurement and the frequency resolution are also limited.

However, in a lot of applications, we don't necessarily need all the spectroscopy information,

we might only want the THz-object interaction behavior in a certain frequency (range). For example, water is involved in most of the biological process and water's strong absorption of terahertz light provides us a way to evaluate tissue water content in different scenarios. In some of those scenarios, the whole spectroscopy information is not necessary. Instead, we are more interested in the tissue-THz interaction, absorption or reflection, across a certain frequency range. In such occasions, it's unnecessary to distinguish time domain or frequency domain, but it does not bother us using the right techniques to extract information that we need. A good example in our lab is, we are using raster scanning system and time domain setup to extract reflected intensity signal with a fixed delay line[31], [32].

1.2.3 Development of THz Detector Arrays

As imaging techniques using scanning method are always time consuming, it is necessary to develop room temperature detector arrays for real time imaging to reach its full potential. With the development of high power terahertz sources, the shift from single detector raster scanning to static array detection is becoming possible.

1.3 Terahertz Applications

Due to its non-ionizing nature, partial absorption effects and dielectric properties, terahertz technology has gained numerous attention in various fields, such as cosmic science[33], [34], non-destructive testing[35][36],defense and security[37], [38]. In this thesis, I'm going to mainly focus on the biological and medical applications.

Development of terahertz techniques, especially the sensitive heterodyne spectroscopy provides an effective way to map remote objects. For the detection of thermal radiation in planetary and astronomical sciences, distribution of gas molecules in the stratosphere, and investigation of planetary atmosphere, terahertz imaging is becoming a more important tool these years. Passive imaging which is mostly applied here relies heavily on the sensitivity of the detectors. Therefore, terahertz band low noise detectors are the key part in these applications.

Terahertz wave's penetration power, its contrast ability and non-ionizing property make it very promising in the non-destructive testing of object made of semiconductor, polymers or ceramics. Pulsed imaging technique is mostly applied here. By measuring the time-of-flight change caused by the dielectric property differences of the semi-transparent object, the structure of the target could be resolved. The detecting could be performed in either transmission or reflection setups.

The non-destructive testing ability could be naturally borrowed to security and defense applications. Many materials of interest for security applications such as explosive and biological agents have their unique fingerprints in THz spectrum and hence could be identified. Therefore, THz imaging could easily be used to detect dangerous weapons underneath clothes or drugs that are hidden in visible-opaque materials such as paper/plastic envelope or boxes. Standoff THz body screening at metro stations and airports are already in use or soon to be used by utilizing arrays of Schottky diodes or heterodyne detection[39], [40].

Terahertz applications in biomedical fields are greatly motivated by the following facts: a).

Terahertz waves are low energy photons and its non-ionizing property makes it an ideal candidate for medical applications; b). Terahertz waves are extremely sensitive to water, which is an important constituent of biological structures and which is also involved in majority biological activities.; c). Potential resonance in biomolecules, such as intramolecular vibrations and intermolecular interactions, which results in unique spectral lines that could be used for constituent identification. Since the first time-domain terahertz image of a tree leaf was reported in 1995[41], terahertz applications in biomedical fields have gained great interests. Scientists from different groups have tried to diagnose breast cancer, skin cancer and oral cancer with terahertz [42], [43],[44]; Diabetic foot syndrome has been imaged by detecting the hydration level of the foot skin[45]; Scar healing was observed with terahertz even when the scar is invisible by eye[45]; Skin flaps was explored by our group and showed the promise in early assessment of flap viability[46]; Our group has started exploring the terahertz imaging of the cornea by detecting the water content as early as 2011[46], and following studies showed great potential for early detection of corneal diseases[47]–[51].

Although improvements have been made in understanding the relationship between terahertz signal and biological mechanism, there still could be a lot to explore. On the other hand, efforts are being made to develop faster imaging system and to get better resolution images. One of my supervisor, Zachary Taylor, always tells me when it comes to biomedical imaging for terahertz, it is more of a instrumentation problem other than a source/detector problem, so efforts have continuously been made in perfecting the system design for different applications. Same as in this thesis, we developed a system for cornea hydration level detection and mainly focus on two questions: how is terahertz signal reflecting the hydration level? and how to make the system faster with better resolution?

1.4 Conclusion

In his chapter, we reviewed the background of terahertz technology. We talked about the bridged THz gap from the different types of THz sources and detectors, explored different system setups of different terahertz applications, compared passive versus active imaging and time domain versus frequency domain. We also briefly reviewed the various applications. In the following part of the thesis, we will talk about my research on the corneal hydration level detection in details.

CHAPTER 2: **CLINIC BACKGROUND**

2.1 **Anatomy of the cornea**

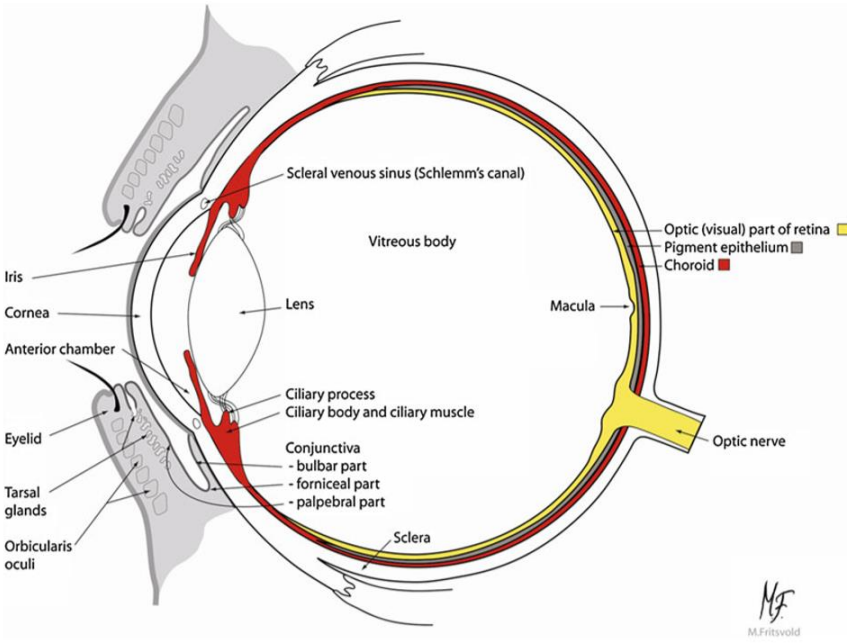

Figure 1. The anatomy of the human eye

As shown in Figure 1, the cornea is the clear front surface of the eye[52]. It sits on top of the iris and pupil, and allows light to pass through and provides around 65 to 70 percent of the refractive power of the eye. Typically, the total refractive power of the eye focused at infinity is between 60 to 65 diopters (D) and the cornea contributes 43 to 48 D to it. A typical cornea measures about 10.6 mm vertically and 11.7 mm horizontally, when viewed from the front. But it appears circular when viewed from the behind and has a uniform diameter of 11.7 mm. The center thickness of the cornea is around 550 microns [53]. The very front of the cornea is covered by a thin layer of tear film, which is replenished by blinking, reflex tearing and some other mechanisms. And on the bottom of the cornea is a body of water, which is called the aqueous humor.

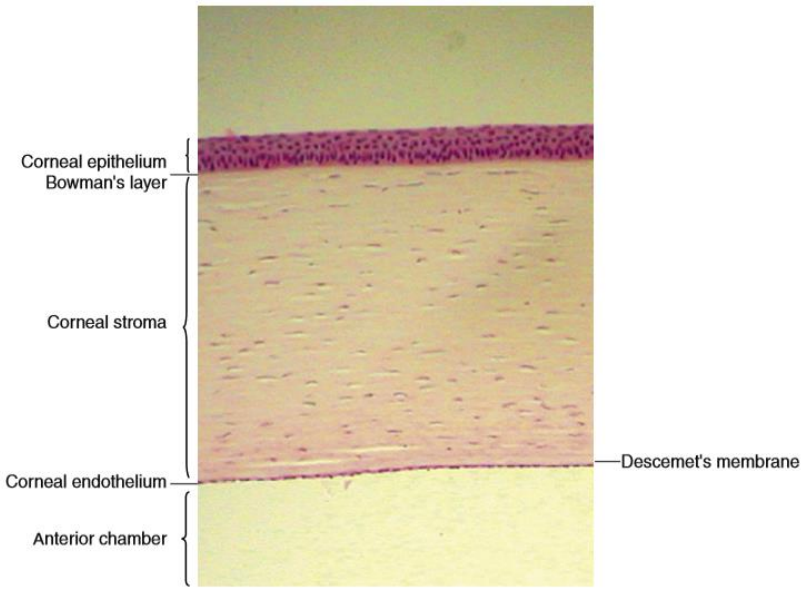

Figure 2. Light micrograph of corneal layers

As shown in the light micrograph of corneal layers in Figure 2[54], from front to back, there are five layers in the cornea: epithelium, Bowman's layer, stroma, Descemet's membrane and the corneal endothelium. The corneal epithelium is about 5 to 6 cells thick (50-60 μm) but responsible for a great part of the focusing power of the corneal, hence that of the eye. Bowman's layer is very thin layer of dense fibrous sheet of tissue connecting the epithelium and the stroma. It only measures about 8 to 14 microns. The corneal stroma consists about 90 percent of the total thickness of the cornea (450-500 μm). It is composed of 200 to 300 layers of regularly arranged 2 μm thick lamellae collagen fibrils[55]. The regular arrangement and spacing between the fibrils are the key to the transparency of the cornea. The Descemet's membrane is about 5 to 15 μm thick (gradually thickens as age grows) and separates the stroma and endothelium layer. The endothelium is innermost monolayer of the cornea and the back side of the endothelium is bathed in the aqueous humor, a body of water fills the space between the cornea and the iris and pupil. The ion channel actively transport water from the cornea to the aqueous humor. It's main function is to keep the cornea in a relative dehydrated state and this is key to maintain corneal transparency.

2.2 Related Diseases

In order to maintain the transparency and shape of the cornea, the hydration level of the cornea, corneal tissue water content (CTWC), is carefully regulated to a narrow range, 75% to 80% by volume. The epithelium layer provides a smooth surface so that the tear film can spread out evenly across the outer layer of the cornea. The smooth surface thus helps minimizing the incident light scattering. Dry eyes, which typically begins in the tears gland and eyelids, can damage the epithelial layer and cause eye discomfort and vision weaknesses.

The endothelium layer is responsible for regulating fluid and solute between the aqueous humor and the stoma. Unlike the epithelium layer, the dead endothelium cells are not replaceable and the left ones are stretched to covered the dead cells' space. Endothelial cell densities drops from 3000 to 4000/mm^2 at birth to 2000/mm^2 as age grows old. Studies show that a density less than 800/mm^2 is not enough to keep the water transportation power to regulate the water content to the desired range, hence the cornea becomes oedematous[53].

In ophthalmology, a lot of corneal disorders could cause the dysfunction of the endothelium layer. Amongst them, Fuchs' endothelial dystrophy (FED), the progressive accumulation of focal excrescences with stromal edema, is a primary disorder of the corneal endothelium that could lead to corneal edema and damage of vision. This disease usually happens in people's fifth to seventh decades of life, and the percentage reaches up to 3.9% of people over their 40 years of age[56]. Other endothelial dystrophies include posterior polymorphous corneal dystrophy, Chandlers' syndrome, but quite less common[55], [57].Several inflammatory process can as well lead to corneal edema. Endotheliitis associated with herpes-viruses, the most common one, is an immune reaction after the episode of infectious keratitis[52]. Ocular surgery can immediately lead to corneal edema or years after. During surgeries like cataract surgery, laser refractive surgery and corneal graft, endothelial damage caused by ultrasound, laser, toxic substances and stripping of Decemet's membrane could all cause corneal edema. Even the surgery techniques and tools

have improved a lot, visual damage or loss still happens after routine or complicated ocular surgery[53].The other reasons that could cause corneal edema include trauma, toxins and etc..

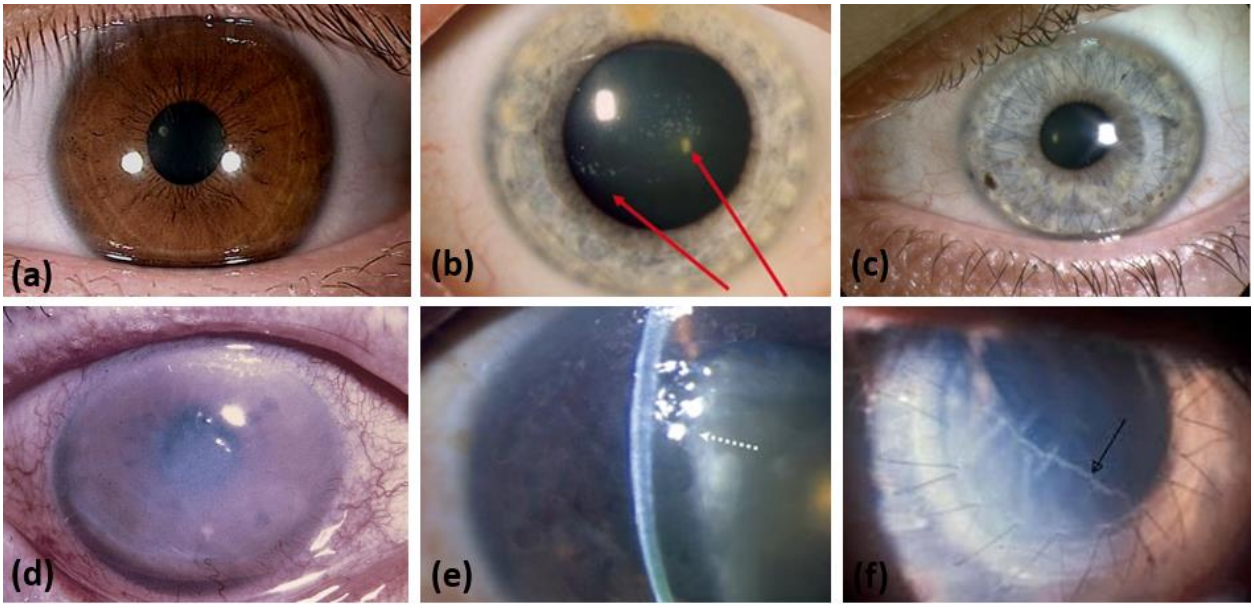

Figure 3. Comparison between healthy eye and diseased eyes.

(a). Healthy eye; (b). Map-Dot-Fingerprint (epithelial basal membrane) corneal dystrophy; (c). Successful corneal graft;(d). Eye with Keratitis; (e). Stage III Fuchs' endothelial dystrophy (FED); (f). Failed corneal graft.

The deterioration of epithelial or endothelial can both lead to loss of water regulating capability and thus corneal edema happens. Corneal edema can cause haloes around light, eye discomfort or pain, and is a contributing factor to the development of corneal opacity. If it is not treated properly, further vision impairment is likely to happen. The end result of majority patients with Fuchs' dystrophy is corneal graft surgery. The bad news is the graft surgery cannot be guaranteed 100 percent successful, with a rejection rate at 5% for low risk grafts and 35% for complicated high-risk grafts[58], [59]. See a comparison between a healthy eye and a diseased eye with edema in Figure 3 (a) and (d)[57]. Both epithelial and endothelial dystrophies, edema is obviously seen in figure (b) and (e). As shown in Figure 3 (c) and (f), we can see the obvious difference between a successful and failure corneal draft surgery. In the latter one, the transplant is rejected by the host.

In such conditions, abnormal CTWC can be an important indicator[60]. Like in corneal graft

surgeries, immune rejection is one of the main reasons for graft failure, and is usually preceded by the formation of edema. Otherwise, if the CTWC returns to a normal state it is an indication of the reversibility of a rejection event. Early detection of abnormal CTWC is critical for the decision of intervention at the early stage of corneal rejection, thus improving the survival rate of rejected grafts. Late decisions often lead to graft failure. The capabilities of detecting water content of the corneal also provide a powerful tool to investigate the formation, development and mechanism of corneal disorders.

2.3 Measurement Limitations

Technologies, like optical coherence tomography, ultrasound and slit lamp, could provide us important biometric data of corneal, but the estimation of CTWC still remains hard and inaccurate, let alone the accurate, direct, non-invasive in-vivo corneal water content measurement. New technologies are still yet to be developed.

2.3.1 Central Corneal Thickness (CCT) Measurements

The most popular way to get the corneal hydration in clinic is to map from the central corneal thickness (CCT). The tools used for CCT measurement is called pachymetry, including optical pachymetry, ultrasound pachymetry, Scheimpflug imaging, optical coherence tomography (OCT), and even magnetic resonance imaging [61], [62]. Different tools are selected for different occasions based on the factors like diseases, patient age and gender, refractive error, etc.. The two most used pachymetry are Optical Coherence Tomography (OCT) and Ultrasonic Pachymetry (USP). Ultrasound Pachymetry requires topical anesthesia and its accuracy heavily depends on the perpendicularity of the ultrasound probe to the corneal. The standard deviation of the measurement could reach about 3 μm, but the contact method, possible bias due to the instill of anesthesia are the obvious short comings. OCT is now widely used for imaging anterior segment in ophthalmology departments because of its non-contact type. Data reconstruction

allows slices of anterior segments with a resolution of 5 μm[53]. Figure 4 [57] shows a cross section of a recipient cornea with an attached posterior disc by anterior optical coherence tomography (AC-OCT). The tissue penetration is about 6 mm and could be used to assess the remainder of anterior segment for patients with corneal scars. Studies showed that USP and OCT measurements usually have good correlation[63], [64].

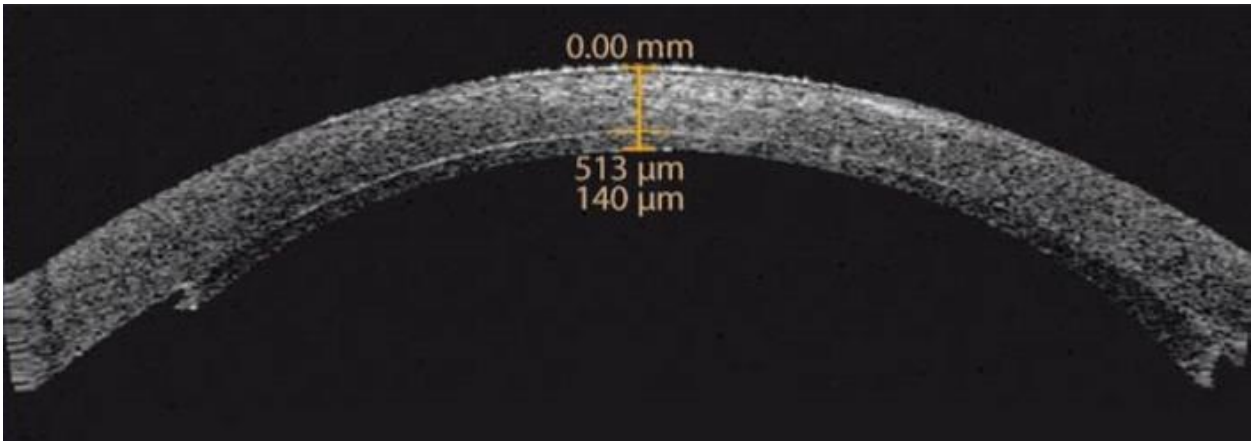

Figure 4. A cross section of a recipient cornea with an attached posterior disc by anterior optical coherence tomography (AC-OCT).

2.3.2 Mapping From CCT to CTWC

Limited researches have directly explored the corneal hydration level, especially in-vivo data. The most complete in-vivo dataset our group could find was from ten rabbit eyes using confocal Raman spectroscopy[65]. The almost linear change from 83% at the endothelial layer to 77% at the epithelial layer seems to match the steady-state diffusion equation with the boundary conditions of water source and evaporation at two boundary layers respectively. However, the fluence energy level used in the experiment, over 1600W/cm^2, is likely to damage the cornea, thus the reliability of the data is questioned.

The linear assumption from the central corneal thickness to water content of cornea was first established as CCT = 0.09+0.142*H from a study in 1965[66]. The equation adopted by our group is :

$$H = \frac{m_{H_2O}}{m_{H_2O} + m_{dry}} = \frac{CCT - 0.091}{CCT + 0.051} \quad (1)$$

Equation (1) is plotted in Figure 5 as the red line. A linear fit is plotted as the black dotted line within the physiologically relevant range, shown as gray shaded area. The slope of the fit is about 40%/mm. However, studies also show that age gender, ethnicity and even different time measured in a day could all influence corneal thickness values, and a variance of 11% is still considered healthy[62]. Some scenarios also challenge the linear fit of the equation. As we know, some people have a corneal thickness maybe smaller than 450 microns but still considered as healthy, but according to this equation we will get a CTWC of 71.6%, which is definitely wrong. This shortfall is well observed and understood by physicians. Another example people always use is the thickness of a dehydrated cornea. Based on the linear fit of the hydration predication, we will have a thickness of 90 microns for a 100% dehydrated cornea, which contradicts with the reported data of ~200 microns[62].

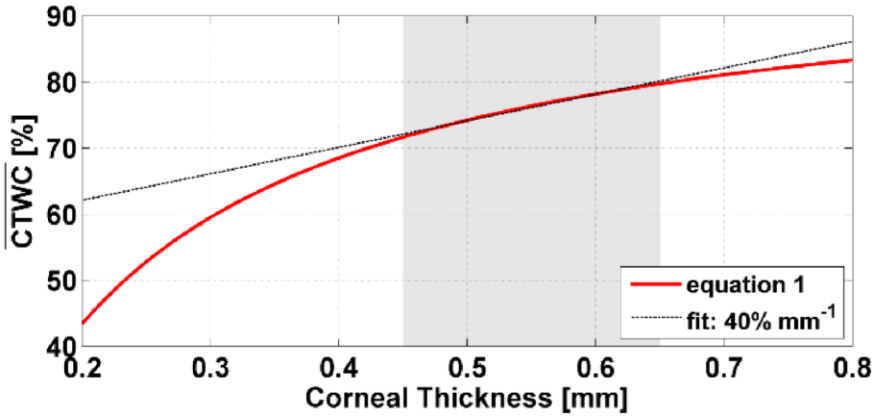

Figure 5. CTWC and corneal thickness relationship.

As a result, despite that very accurate thickness measurement could be obtained using various pachymetry, the inaccurate prediction from CCT to CTWC still hinders the application of this method. Numerous studies verified the inconsistency between measured CCT and predicted CTWC in different conditions such as graft rejection, Fuch's Dystrophy and Keratoconus[62], [63],

[67], [68]. Therefore, the measurement of corneal hydration level still remains both a clinical and research problem.

A lot of other researchers have tried to obtain the CTWC through different methods as well. Brian Fisher and N. Bauer tried to use confocal Raman Spectroscopy to assess the transient hydration changes and hydration gradient across the cornea respectively [69], [65]; Sung W. Jeon used dual-wavelength optical coherence tomography to image the corneal hydration[70]; Henning Aurich tried continuous measurement of corneal dehydration with online optical coherence pachymetry[71]; other methods including atomic force microscopy and near infrared reflectometry [72]. A handheld corneal hydrometer is even reported[73]. Of all the listed methods, only Raman Spectroscopy could provide absolute water content value. However, the scattering power is so limited to the wavelength used, thus unacceptable laser power is required.

Since many corneal disorders are characterized by an abnormally high CTWC. It makes CTWC an attracting target that doctors want to explore, which might help diagnose corneal disorders. In some extent, CTWC measurement not only allows doctors to see the diseases but also to predict potentially tissue damages.

2.4 Opportunity for THz Imaging

As we discussed in the chapter of THz background, we know that THz waves are sensitive to polar molecules, like water which consist of a big portion of cornea tissue. Plus the non-ionizing effect, submillimeter lateral and axial resolution and minimal scattering in biologic tissue, it has drawn great attention from the medical field. The easily accessible tissue of the cornea also offers a unique opportunity for TWC mapping given its low physiologic variation and homogenous composition when compared to other tissue systems in the human body. Especially, cornea is a thin film at THz frequency, and presents a distinct etalon effect, which could help extract water content gradient in the thickness dimension.

On the other hand, other frequency region could not work here for different reasons. For example, UV lights is likely to cause DNA damage because of its high photon energy; long time evolution has made cornea tissue optical properties vary little in visual light region, thus no useful information could be obtained; when it comes to near infrared, the scattering effect will dominant over transmission and reflection.

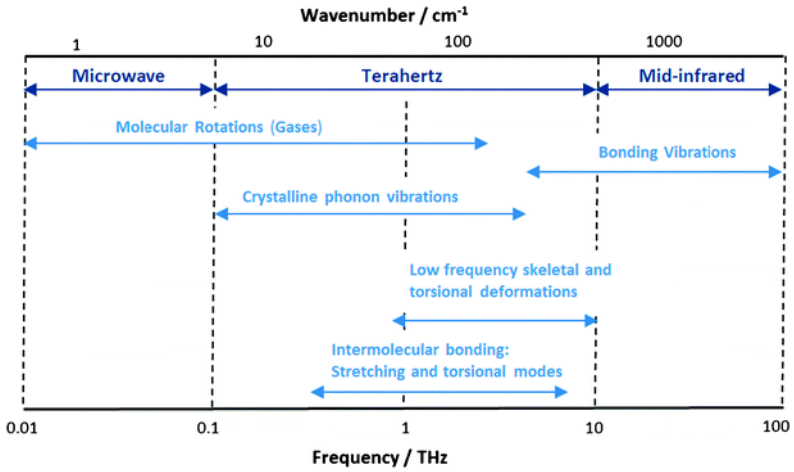

Figure 6. Molecular modes and activity in the terahertz region of the electromagnetic spectrum

The lack of efficient, non-invasive and direct measurement of CTWC presents a great opportunity for THz sensing and imaging techniques.

CHAPTER 3: **BACKGROUND WORK**

3.1 In-vivo Animal Experiment

Based on groups' previous phantom, ex-vivo experiments, the group felt necessary to move on to in-vivo animal study, as in ex-vivo studies, no matter how carefully the samples were prepared the corneal properties were changed. For example, backside of cornea on excised eyeball will get hyper hydrated because of the failure of endothelium layer's regulation between anterior chamber and stroma, while front side will get super dry because of exposure to the air. Direct in-vivo data is necessary for evaluating the imaging capability of THz technique.

3.1.1 System Setup

Two systems of frequencies centered at 100 GHz and 525 GHz were built by the group. The first system had a Gunn diode as source which operated at 100 GHz and had a Pyroelectric Detector. As shown in Figure 7 (a), the source was frequency modulated over a range of 3 GHz at the rate of 1 kHz. An amplitude modulation was also applied to the source and the modulated signal from the detector was fed into a Lock-in Amplifier (LIA) for demodulation and low-pass filtering.

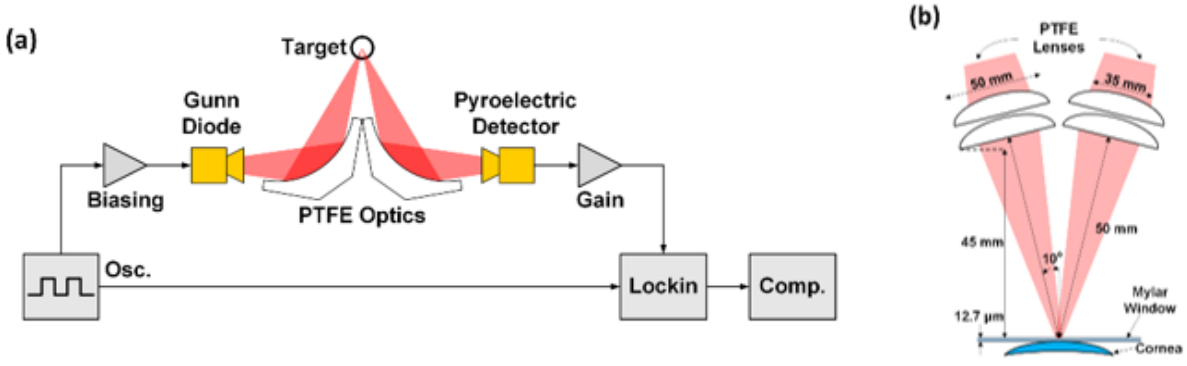

Figure 7. (a) Block diagram of 100 GHz sensing system. (b) Illumination geometry.

As the center frequency was around 100 GHz, the wavelength of the wave is around 3 mm, so the group was only able to get a focused spot size of 4.5 mm, which was meaningless to do

any imaging over the cornea. Thus, this system was only used to do a point measurement in the center of the cornea. As shown in Figure 7 (b), a mylar window was placed on top of the cornea, a PTFE lens was used to focusing the millimeter wave to the target and another PTFE lens was used to collecting reflected signal.

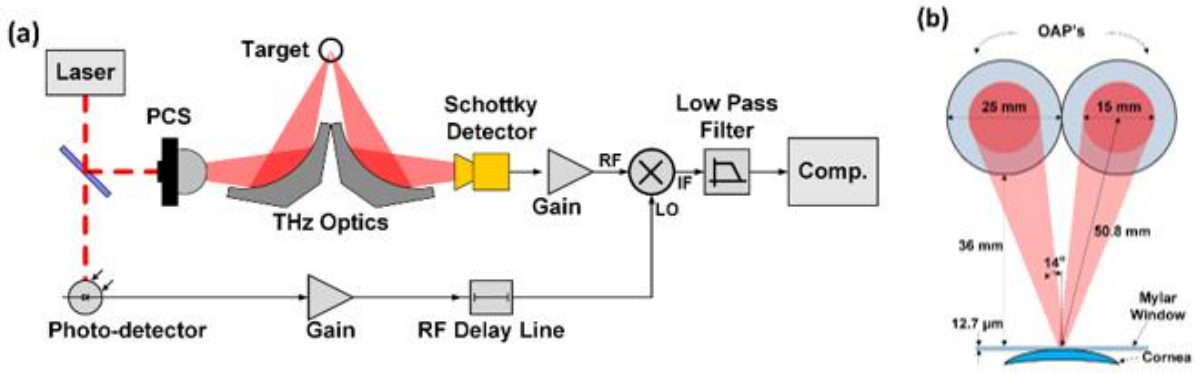

Figure 8. (a) Block diagram of 525 GHz sensing system. (b) Illumination geometry.

The second system used a photo conductive switch (PCS) driven with a femto laser at 780 nm to generate a broad band THz wave centered at 525 GHz. This system had been applied to many different studies[31], [49], [74]. This system schematic employed a gated detection, where the rectified signal from the Schottky detector was multiplied with the synchronized laser-pulse-induced gating signal and then low pass filtered, and greatly enhanced the signal to noise (SNR) ratio of the measurement.

The cornea also had a mylar window stacked above. Two OAPs with diameter of 25.4 mm and effective focal length (EFL) of 50.8 mm were used for focusing light to the target and collecting energy reflected from the target just as the PTFE lenses did in the first system. The OAPs were tilted a little bit towards each other so that their focal points would overlap.

3.1.2 Animal Experiment Design

The study was approved by the University of California's Institutional Animal Care and Use Committee (IACUC). Considering the similarities in size, shape and CTWC, 5 white New Zealand male rabbits were selected as the experiment models.

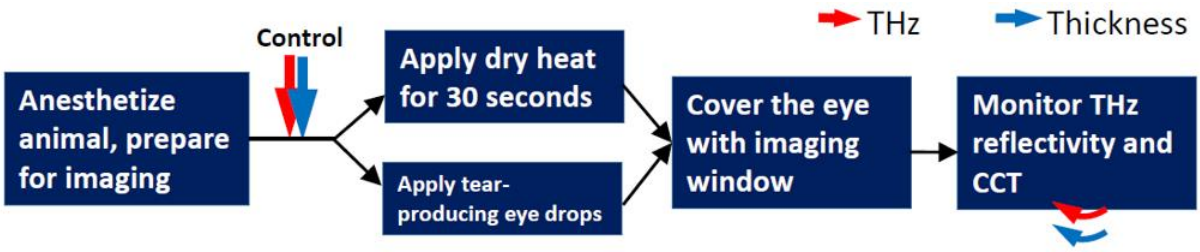

Figure 9. Flow chart of experiment procedure.

As shown in flow chart of experimental procedure in Figure 9, each animal was anesthetized in the beginning of experiment. This experiment has 2 sets of measurement. In the first set of measurement, the right eye of the rabbit was kept open and dry heat blow was applied to the eye for 30 seconds. A 12.7 micrometer Mylar window was lowered to the cornea's surface to secure it in place and make sure it was horizontally positioned. First, the probe tip of an ultrasound pachymetry was placed directly on the top of window to get the thickness readings of the cornea. There were 5 individual readings taken and averaged as the final recording. The substrate thickness was subtracted from the readings. Second, the reflectivity signal of the 100 GHz system then was recorded as described above. The integration time of the lock-in amplifier was set to be one second. Third, a 20 mm by 20 mm FOV was imaged with the step size of 0.5 mm with the second system.

In the other set of measurement, the right eye of rabbit was opened and applied with producing eyedrops instead of dry heat air flow. The following steps kept the same as in the first measurement. Figure 10 Shows how the rabbit was secured in place for measurement during experiment.

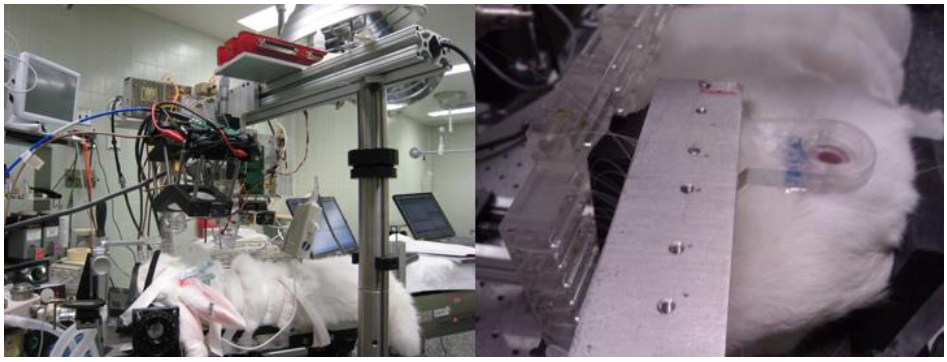

Figure 10. How the rabbit was secured in place for measurement.

3.1.3 Animal Data

Figure 11 shows correlation between central thickness and mm waves in (a) and shows correlation between central thickness and terahertz signal in (b). As in (a), we can see statistically significant increases in signal from all 5 rabbits, the positive correlation between CCT measurement and 100 GHz reflective signal suggested the increase in corneal tissue water content. However, the different slops suggested this measurement was still contrast measurement instead of absolute measurement.

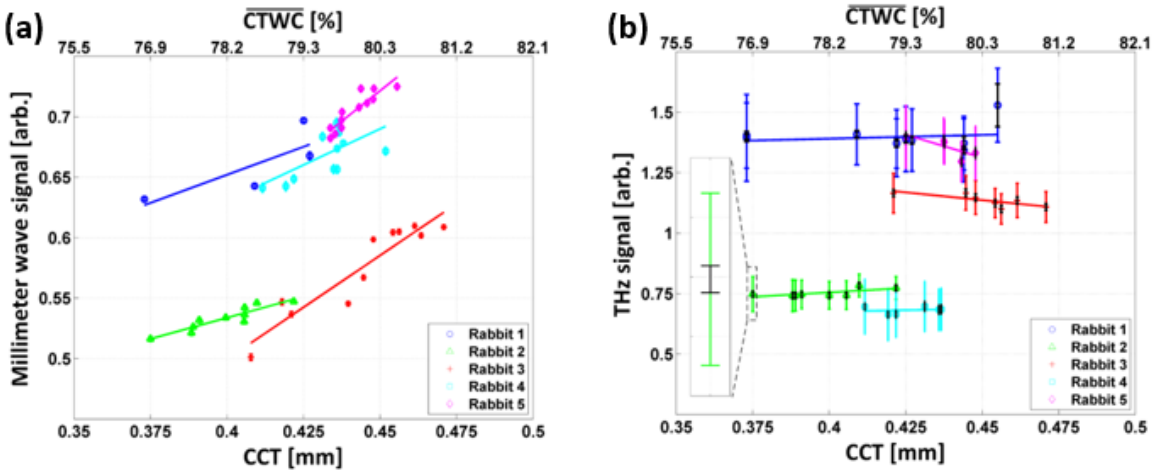

Figure 11. (a) Correlation between central thickness and millimeter wave signal; (b) Correlation between central thickness and THz signal.

In figure (b), we cannot see any significant correlations between central cornea thickness values and the collected THz signals. As the CCT increased, the reflectivity signal remained fairly stable and it even dropped a little bit in two rabbits.

3.1.4 Analysis

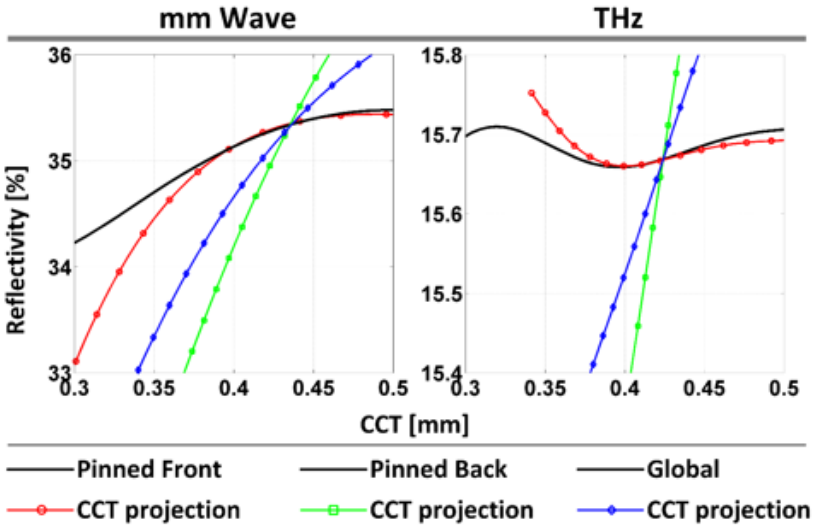

Figure 12. Simulated reflectivity for mm wave and THz signals under three scenarios.

In clinical, people treat CTWC variations as an average change across the whole thickness dimension. However, it is more likely that only the front side is going to change in a dry eye or our above experimental protocol while the endothelium still functions properly; and the front side keeps constant while back layer starts to get super hydrated in endothelial failure cases; the hydration level will more likely have global change in the end point for the Fuck's dystrophy. In the experiment, the healthy rabbits were more likely to maintain a constant hydration level at the endothelial layer; however, as the Mylar window blocked the natural contact between eyelid and air, the water content was likely to be perturbed.

As in Figure 12, the group simulated reflectivity for mm wave and THz signals under above mentioned three scenarios: the pinned front, pinned back and global hydration change. In the figure we can see the mm wave simulation agreed well with the experimental data, reflectivity

increased while the thickness increased. However, for the THz case, the relatively flat experimental data suggested that we either had a pinned front case or the corneal tissue content didn't change while the thickness changing.

3.1.5 Discussion

The group's in-vivo experiment demonstrated the ability of millimeter wave and terahertz systems for sensing hydration level change. The millimeter wave and thickness measurement had positive correlation, while the insignificant correlation between terahertz wave and thickness value allowed to deduce how the cornea tissue was perturbed and what change could be observed for different hypothesizes. The experiment also confirmed that the cornea is an etalon for the Terahertz wave and lower frequencies seems to be able to see deeper into the eye compared to higher frequencies.

The interpretation of the reflectivity into the absolute water content was quite challenging, as finding the exact overlap for the focal plane of the system and the animal cornea was extremely hard with so limited time window during the experiment. Another big challenge was the contact window placed on the cornea inevitably perturbed the hydration level of the cornea as well as changed the thickness of the cornea no matter how carefully the window was lowered down to minimize the static force. Even all the confounders in the experiment could be figured out, the contact window must be removed.

Therefore, a non-contact, windowless measurement system must be developed not only for the accuracy of measurement but also for the comfort of patients. Based on this conclusion, the group decided to build a next generation non-contact cornea imaging system.

3.2 Rectilinear Scanning System

3.2.1 Geometry of Human Cornea

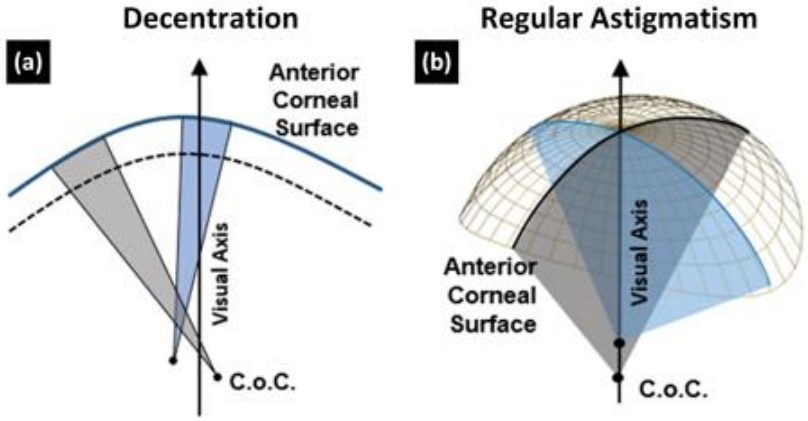

Figure 13. Decentration and astigmatism in corneal anatomy.

Before designing any non-contact imaging system, the very first question the group needed to ask was how spherical the eyes are? Luckily, several studies had given the answers [75]–[77].

As Figure 13 and Figure 14 show, decentration and astigmatism exist in both healthy and diseased eyes. For a healthy eye, the decentration causes a deviation of displacement of radius of curvature (RoC) of around 0.05 mm, while regular astigmatism is a little higher at 0.08 mm and the total contribution of some other factors is around 0.015 mm. If measured by the wavelength of a terahertz wave at 650 GHz, it is a total variation of ±0.21 λ over the whole size of cornea of 17.32 λ, which means a 1.21% variation of the whole geometry.

Keratoconus is when the cornea thins out and bulges like a cone. In this case, the mean RoC displacement caused by decentration, astigmatism and other factors are around 0.4 mm, 0.35 mm and 0.08 mm. We can still compare them to the wavelength of a terahertz wave at 650 GHz, it is a total variation of ±1.16 λ over the whole size of cornea of 17.32 λ, which means a 6.69% variation of the whole geometry.

For the eyes that had grafted surgery, the mean RoC displacement caused by decentration, astigmatism and other factors are around 0.3 mm, 0.35 mm and 0.08 mm. When compared to the wavelength of a terahertz wave at 650 GHz, it is a total variation of ±1.01 λ over the whole size of

cornea of 17.32 λ, which means a 5.83% variation of the whole geometry.

As a result, corneal geometry presents a shape of sphere, and has very small variations between individuals, usually smaller than a quater wavelength of THz in healthy eyes and around one wavelength in diseased eyes. Compared to the dimension of target and beam size, these deviations are negligible, so we can treat the cornea as a perfect sphere in our study, which could make the group's study and instrumentation much easier.

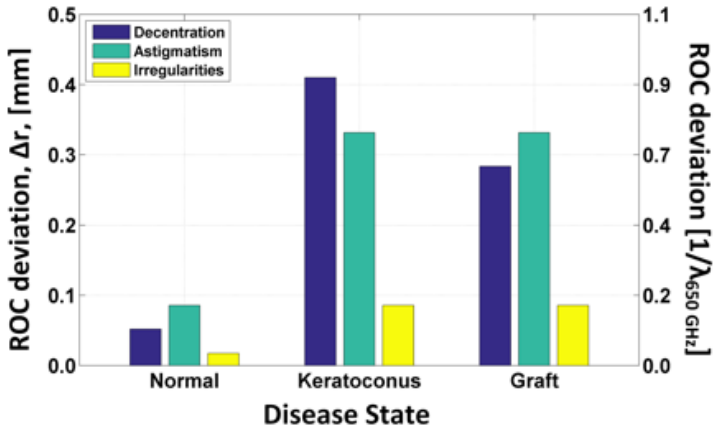

Figure 14. Influence of diseases on ROC deviation.

3.2.2 Design Principles

Since the cornea could be treated as a perfect sphere with our illumination source, the design is becoming easier. As shown in Figure 15, an off-axis parabolic reflecting mirror (OAP) was used to complete the non-contact scanning of the cornea.

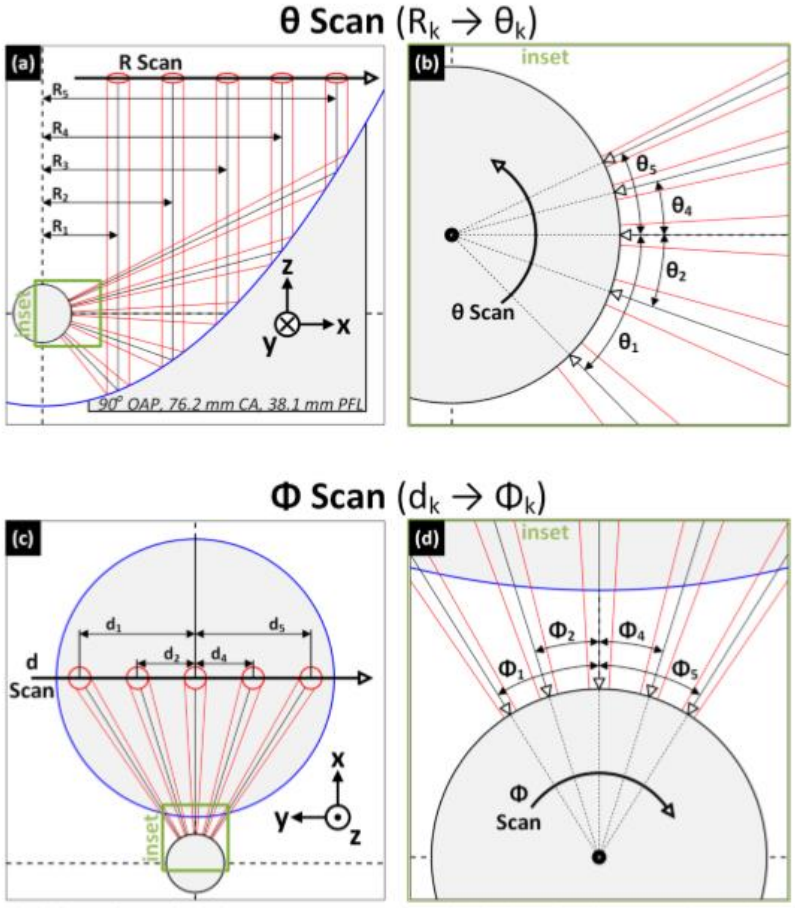

Figure 15. Scanning principle of the cornea using an OAP.

In this design, the sphere target, cornea, is placed at the focus of the OAP. This method performs a transformation between a polar coordinate system and a Cartesian coordinate system via the projection of a parabolic surface. A collimated beam coming from the clear aperture of the OAP along the optical axis interacted with the parabolic surface and is redirected towards the center of the target. The translational movement of the collimated beam on the aperture plane is converted to the angular scanning across the surface of the target. As in the setup plotted above,

the translational scan in the x direction is converted the angular scan in θ direction, and scan in y direction to angular scan in φ direction.

3.2.3 System Setup

The whole system is consisted of mainly three parts, the transceiver subsystem, the scanning subsystem and the imaging mirror. The transceiver subsystem helps collimating the diverging beam from the source and provides it to the subsystem of the rectilinear scanning, as well as collecting energy from the collimated reflected THz wave and focus it to the detector. The 50/50 beam splitter helps the detector and source to co-use the optical path from the scanning mirror to the target. The scanning subsystem is converting the translational scan in the clear aperture plane into angular scanning centered at the focus of the objective OAP by the mechanical scans of the two flat mirror in x and y directions. A big OAP is working as the target mirror and the target is positioned at its center.

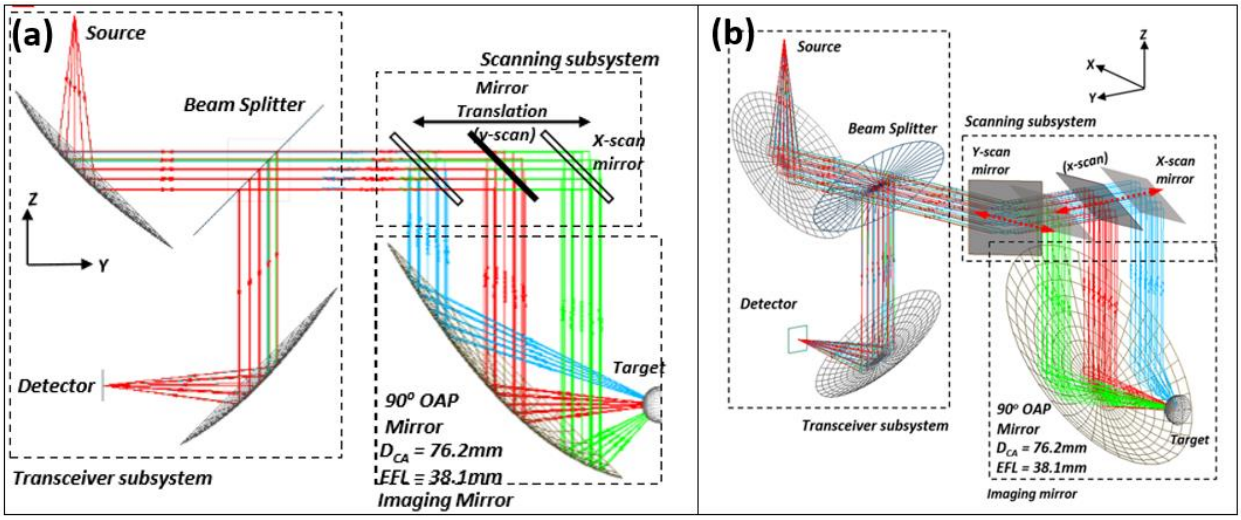

Figure 16. Complete optical setup of the rectilinear scanning system.

A system was implemented as in Figure 17. An amplifier-Multiple Chain (AMC) (Virginia Diode, VA) and a WR1.5 wave-guide mounted zero biased Schottky diode (ZBD) (Virginia Diode, VA) were used as THz source and detector. To get rid of the possible standing waves during the

measurement, the source was frequency modulated over ~2 GHz, providing a wide enough bandwidth to cancel the etalon effect of the whole optical path, at a rate of 100 kHz. The source was also amplitude modulated with the TTL output from the lock-in amplifier (LIA) at a frequency of 900 Hz and the detection signal was fed to the LIA and acquired with LabJack using MATLAB.

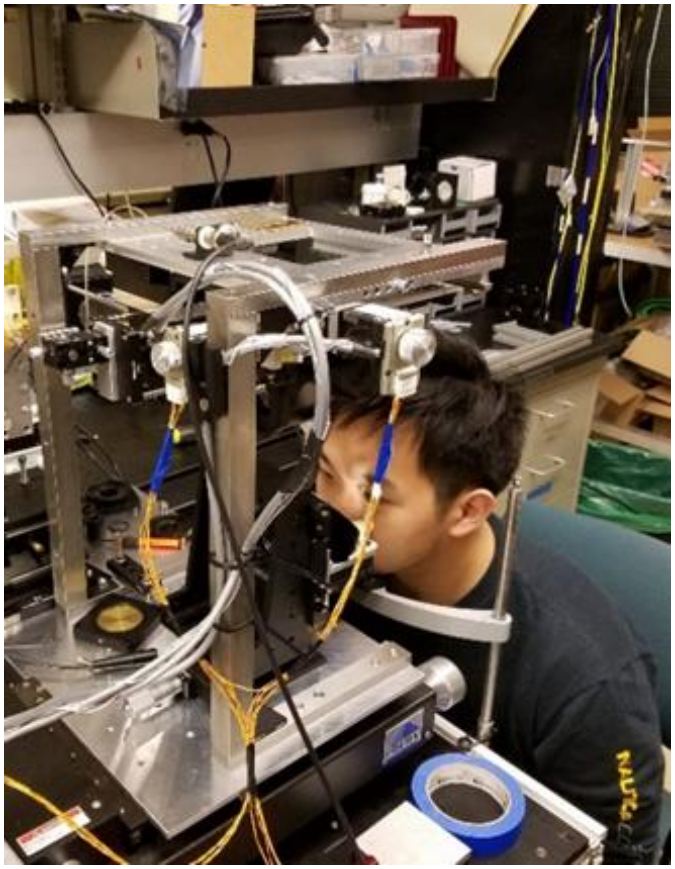

Figure 17. The developer is testing the rectilinear scanning system.

3.2.4 Imaging Data

The system was first tested with a Brass ball to verify its coupling efficiency across its field of view, and with a polypropylene ball with aluminum strips attached in different orientations, a checkerboard ball made of brass and polypropylene to verify the spatial resolution and sampling distribution across the whole field of view. The results were displayed in Figure 18. The first row displays the visual images of the targets, the second row shows the 2D raw data and the images in the third row were registered to a 3D sphere.

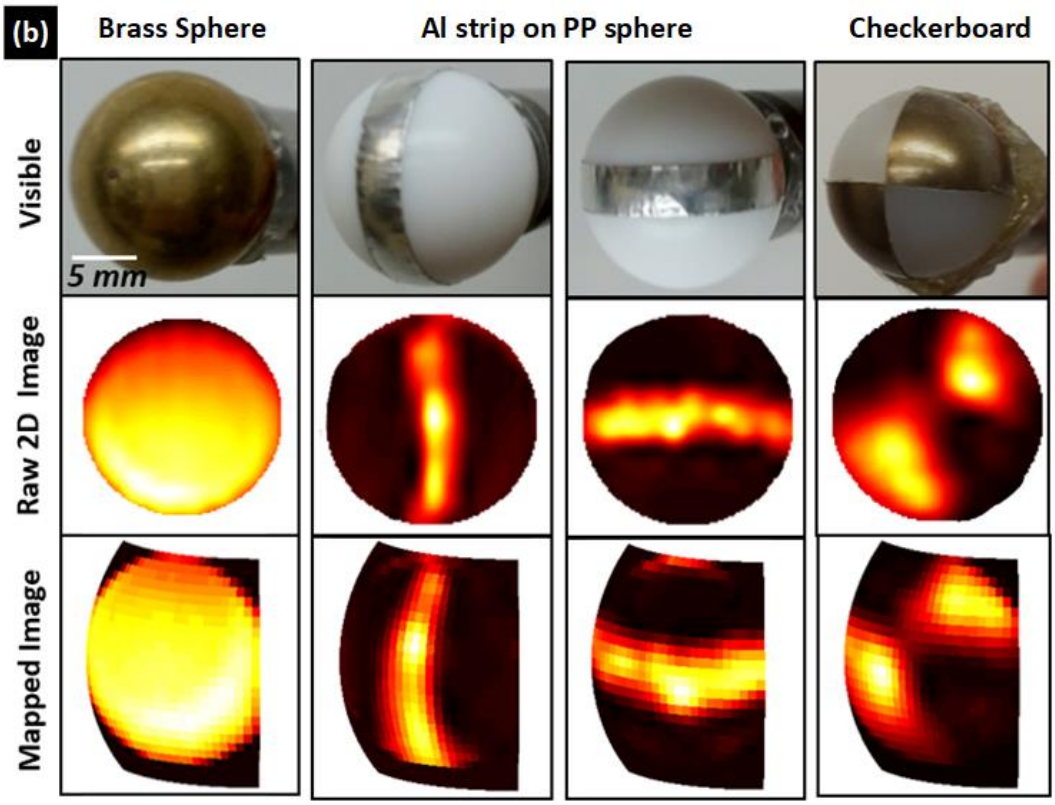

Figure 18. Images of different target balls for demonstration.

About ten volunteer eyes were imaged as the preliminary human data. The subject was asked to rest their chin on a chin rest frame and stare at a white ring that was for alignment. After the operator align the eye to the target mirror manually, each image could take about 20 to 60 seconds to finish. In a complete scanning process, the x mirror took one step while the gap between y mirror's complete scans in different rows. While the canning changing lines, the

volunteer could blink their eyes to keep themselves comfortable.

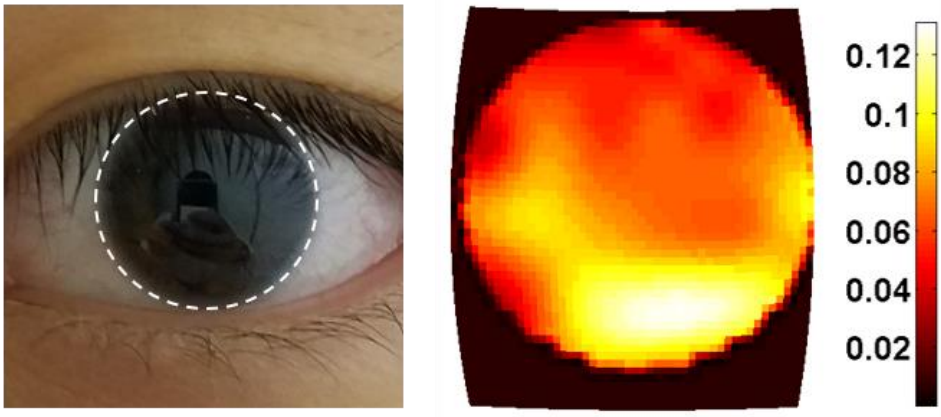

Figure 19. The imaged area of the eye and a typical image of the volunteer's eye.

3.2.5 Discussion

As in the images of different target balls for demonstration, the image of the brass sphere displays an increase of copping efficiency from top to the bottom which is consistent with the group's previous simulation prediction. The image looks symmetric in the other direction. From the image of the polypropylene ball with aluminum strips attached we can see an oblivious widening effect of strip from the top to the bottom with some local intensity extrema, which is also consistent with the expectation of spot size increase in the top to bottom direction.

The images of the volunteer eyes were the first ever in-vivo THz images of human eyes taken. However, maybe because all the volunteer eyes were in healthy condition, or maybe due to the data was screened by some confounders, like the tear film, the ten eyes looked nearly the same with the system. Comparisons between healthy eyes, diseased eyes or even corneal transplanted eyes were needed for further investigation of the system's capability. However, the scanning time needed for each scan really killed this possibility to be tested in a real clinical environment.

3.3 Conclusion

Tremendous efforts have been made to explore the possibility of THz imaging technique in corneal hydration level detection by our group. The animal study showed that cornea acts as an etalon under the THz wavelength, which further strengthened the confidence of THz's capability of extracting the cornea's water content. The development and testing of rectilinear scanning system verified the feasibility of treating the cornea as a perfect sphere for imaging. Especially, the first ever human cornea imaging with THz was very exciting. The tricks of non-contact angular scanning of cornea and how to convert rectilinear scan to angular scan were also inspiring for future system design and instrumentation.

Despite the achievements, there were still some problems need to be addressed on the rectilinear system. First, the variation of spatial resolution and nonhomogeneous coupling efficiency across the FOV obviously could influence the imaging quality. Second, since the system is very sensitive to the alignment of the target, patient movement is another confounder that could possibly ruin the measurement. Third, tear film might be blocking the THz wave and make it hard to get any meaningful data. A measurement combination of amplitude and phase detection might be able to help overcome the ambiguity in the experiment. More importantly, the top weakness of the rectilinear scanning design is the relatively large transverse displacement necessary to scan a comparatively small angular FOV on the cornea. This relationship creates a limitation on image acquisition rate that may hinder translational feasibility.

A non-contact THz imaging system with more efficient scanning mechanism and better imaging quality is necessary.

CHAPTER 4: **EM MODELING OF CORNEA-THZ INTERACTION**

4.1 Stratified Cornea Model

4.1.1 Assignment of Tissue Properties

As we know, there are five layers in the cornea from font to back. The relatively thick layers are cornea stroma, epithelium layer and endothelium layer, especially the stroma layer forms about 90 percent of the total thickness. It is composed of 200-300 layers of regularly arranged lamellae fibrils. The stroma layer, epithelial, endothelial layer and other two layers are all optically smooth and has very little scattering effect under THz wavelengths. People believe that the cornea tissue water content only varies according to the depth, and keeps constant in the transverse direction.

Therefore, the cornea could be treated as stratified layers, whose water content changes in the depth direction while keeps constant inside the same layer. We employ a classical electromagnetic model of multi-layer dielectric slabs, whose dielectric constant is defined by the varying tissue water content.

As the stoma consists most of the cornea thickness and the stoma is mainly water and collagen, we can use the Bruggeman model [78], [79] to compute the effective dielectric constant of each layer of the cornea tissue, as below:

$$\mathrm{p}_{w,i}\left(\frac{\hat{\varepsilon}_i - \varepsilon_w}{\varepsilon_w + 2\hat{\varepsilon}_i}\right) = \left(\mathrm{p}_{w,i} - 1\right)\left(\frac{\hat{\varepsilon}_i - \varepsilon_c}{\varepsilon_c + 2\hat{\varepsilon}_i}\right) \tag{2}$$

Where $\mathrm{p}_{w,i}$ is the water volume fraction in each layer, ε_c is the dielectric constant of collagen. Dielectric constant of water could be computed with Double Debye model [80], in equation (3):

$$\varepsilon_w(\mathrm{f}) = \varepsilon_\infty + \frac{\varepsilon_0 - \varepsilon_1}{1 - \mathrm{j}2\pi\,\mathrm{f}/\mathrm{f}_1} + \frac{\varepsilon_1 - \varepsilon_\infty}{1 - \mathrm{j}2\pi\,\mathrm{f}/\mathrm{f}_2} \tag{3}$$

Where ε_∞, ε_0, ε_1, f_1, f_2 are dielectric constants and relaxation frequencies and could be found in [80]. The optical path length is defined as equation (4), where θ_i is the incident angle to each layer, λ is the wavelength of THz.

$$\delta_i = \frac{2\pi}{\lambda} l_i \sqrt{\hat{\varepsilon}_i} \cos(\theta_i) \tag{4}$$

We can have the recursive reflectivity with the computed Fresnel coefficients using equations (5) and (6).

$$\rho_i = \frac{\sqrt{\hat{\varepsilon}_{i-1}} \cos(\theta_{i-1}) - \sqrt{\hat{\varepsilon}_i} \cos(\theta_i)}{\sqrt{\hat{\varepsilon}_{i-1}} \cos(\theta_{i-1}) + \sqrt{\hat{\varepsilon}_i} \cos(\theta_i)} \tag{5}$$

$$\Gamma_i = \frac{\rho_i + \Gamma_{i+1} e^{-j2\delta_i}}{1 + \rho_i \Gamma_{i+1} e^{-j2\delta_i}} \tag{6}$$

4.1.2 Stratified Model Overview

As the Bowman's layer and Descemet's membrane are only around 10 microns in thickness which is negligible compared to the THz wavelength, only the epithelium, stroma and endothelium are marked in the model setup in Figure 20. The cornea is discretized into N layers of media whose dielectric constants are homogenous and dependent on the water content of each layer. The optical property of each layer could be calculated accordingly. Note one point here, the tear film is treated as another independent thin layer of water on top of the cornea layers, and the aqueous humor is modeled as water backing beneath the layers. Γ_1 is the first layer reflection coefficient of the cornea and Γ_{N+1} is the Fresnel coefficient between the last layer of cornea and the aqueous humor. The bottom of the picture displays the depth dependent water variation which was obtained from 10 rabbit eyes using Raman spectroscopy [65].

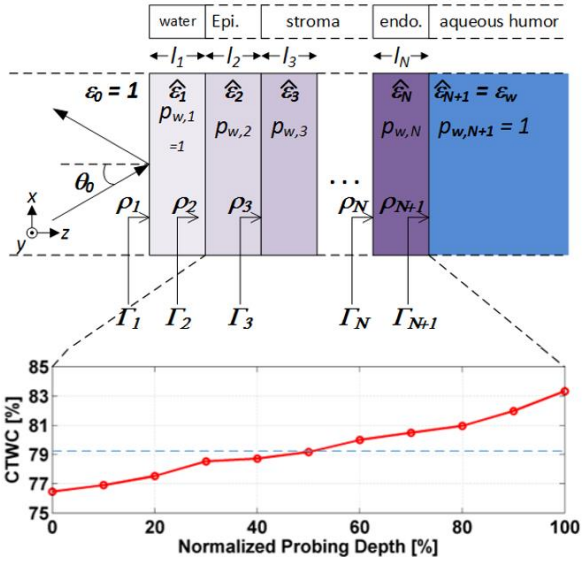

Figure 20. Stratified model for cornea with depth dependent water content variation

4.2 Reflectivity with Different Sources

As shown in Figure 21, as frequency increases, the absorption of e-field by the cornea increases and this results in a bigger attenuation of the signal and smaller penetration depth. Due to the strong absorption, the majority reflected signal will be from the tear film and epithelium. For lower frequencies, the wave is more likely to penetrate deeper and see the back of endothelium layer than higher frequencies whose energy tends to die out in the stroma before reaching endothelium layer. If the electromagnetic wave can travel deep enough, the aqueous humor will act like a lossy back and the spectral response will be dependent on the thickness of the cornea and presents an etalon effect.

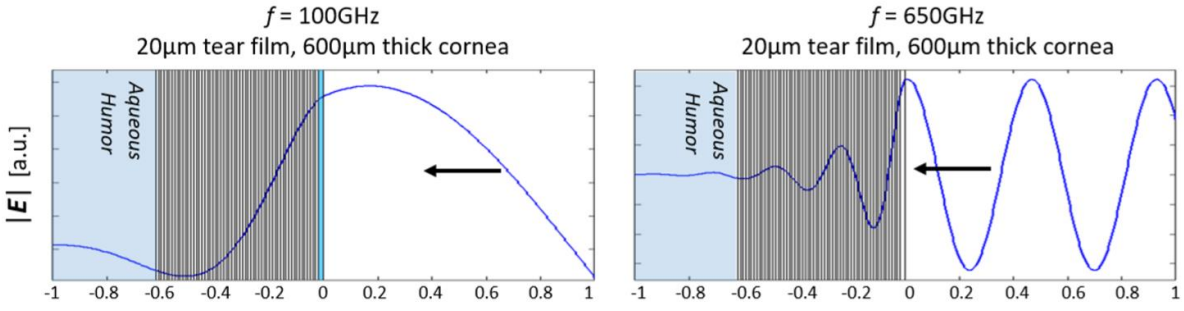

Figure 21. E-field penetration into the corneal tissue at 100 GHz and 650 GHz.

The reflectivity of the cornea is modeled with a broadband measurement. In the modeling, we can treat the reflectivity as the total reflected signal collected with the detector by the signal could be collected with direct measurement over the effective spectrum range of the source, as in equation (7):

$$\mathcal{R}_n(p,d) = \frac{\int_{\Omega_f} S_s(f) S_D(f) |\Gamma_0(p,d,f)|^2 df}{\int_{\Omega_{f,n}} S_s(f) S_D(f) df} \tag{7}$$

Where $S_s(f)$ is the source power spectral density, $S_D(f)$ is the detector spectral responsivity and p is the tissue water content and d is the thickness of corneal thickness.

In the complete modeling, there are several variables we can always play with. They are the average tissue hydration content, the hydration gradient, tissue thickness, tear film thickness and of course the source properties. In this section, we explored the spectral response with different sources over different gradients of water content distribution.

In the following simulation we explored the reflectivity with different cornea thicknesses and hydration levels. It would be difficult to have a 2D presentable result over the whole spectral range with two additional variables, CTWC and CCT. Therefore, we here use two predefined sources centered at 100 GHz and 525 GHz respectively.

4.2.1 Source Setup

As shown in Figure 22, the two predefined sources model the sources used in the two systems used for the in vivo animal study, one centered at 100 GHz and the other at 525 GHz. For both of the sources, different quality factors (Q=5, 50) are used to simulate a broad band and narrow band scenarios. Assuming a Gaussian profile for power spectral density, the center frequency is defined as $f_{0,n}$, and quality factor as Q_n $(n = 1,2)$, we will have the source band as

$$\Delta f_n = \frac{f_{0,n}}{Q_n}, \ \sigma_n^2 = \frac{\Delta f_n^2}{4\ln(2)}, n = 1,2 \tag{8}$$

The source spectral equation will be:

$$S_n(f) = \exp\left(\frac{(f - f_{0,n})^2}{\sigma_n^2}\right) \tag{9}$$

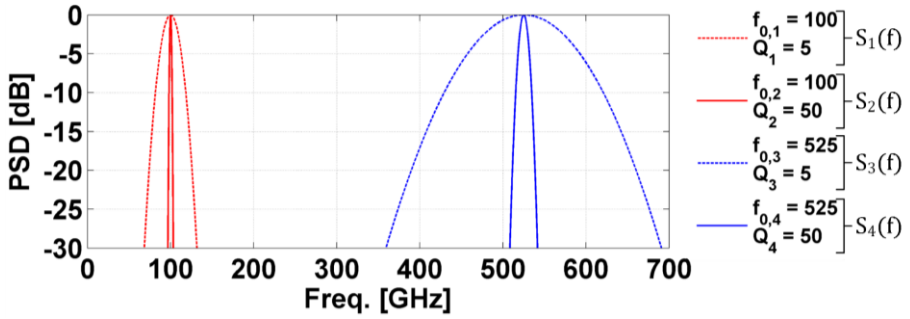

Figure 22. Predefined EM source.

As in this simulation, we have the predefined source, we don't have to count for the source power spectral density and can just remove it from the integration when calculating the reflectivity, the equation will be modified to:

$$\mathcal{R}_n(p,d) = \frac{\int_{\Omega_{f,n}} S_n(f)|\Gamma_0(p,d,f)|^2 df}{\int_{\Omega_{f,n}} S_n(f) df} \tag{10}$$

4.2.2 CTWC Distribution Profile

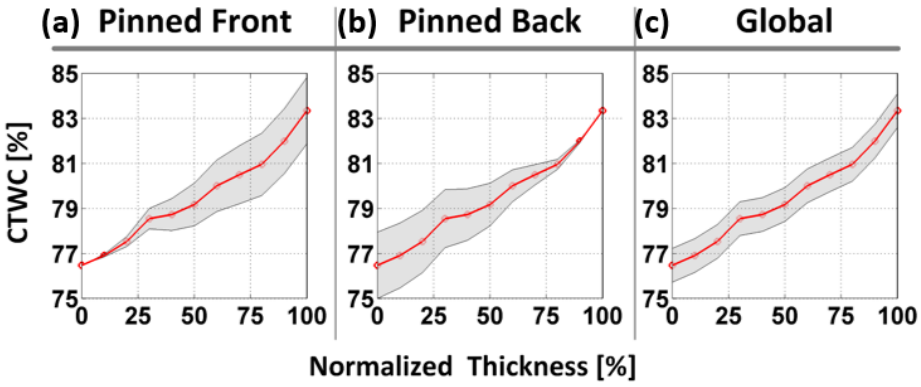

Figure 23. CTWC gradient models set for pinned front, pinned back and global model.

Current clinical practice trends to treat CTWC as an average change in hydration, however it is more likely that different occasions will have different variation parameters. For example,

endothelial dystrophy is due to the failure of endothelial layer and the cornea gets hyper hydrated from the end layer while the front layer keeps steady in the beginning, more likely a pinned front model as illustrated in Figure 23 (a). Dry eyes and the case in our animal experiment blew with air tends to fit the pinned back model better, where front layer water content changes while back layer stays constant, as shown in Figure 23 (b). Figure 23 (c) shows the global changing case like at the end point for Fuch's dystrophy. In the figure, the red line is the baseline of water content at different depth and the shaded grey area defines the variation range of the water content at different depth for different models.

The water gradient models are modeled with following equations:

$$g(x,\alpha) = \alpha\left(e^{x/\sigma} - 1\right),\ \sigma = \frac{100}{ln(2)} \tag{11}$$

$$H_{front}(x,\alpha) = p_w(x) + g(x,\alpha) \tag{12}$$

$$H_{back}(x,\alpha) = p_w(x) + g(100 - x,\alpha) \tag{13}$$

$$H_{global}(x,\alpha) = p_w(x) + \alpha\left[\frac{1}{ln(2)} - 1\right] \tag{14}$$

Where x is the normalized depth in percentage of the cornea, from the front side epithelium of 0% to back side at the aqueous humor of 100%; $p_w(x)$ is set to be the baseline water content at depth of x, plotted as the red line in the model figures; α is the water variation parameter, defines the range of the water content variation.

4.3 General Observation

The simulation results for 100 GHz are displayed in Figure 24. The three water distribution models and two different quality factors yielded six figures of each. The x axis represents the corneal thickness, from 0.2 to 0.8 mm and y axis is the average CTWC value from 75% to 85%. The reflectivity is displayed with the same color bar among all the figures.

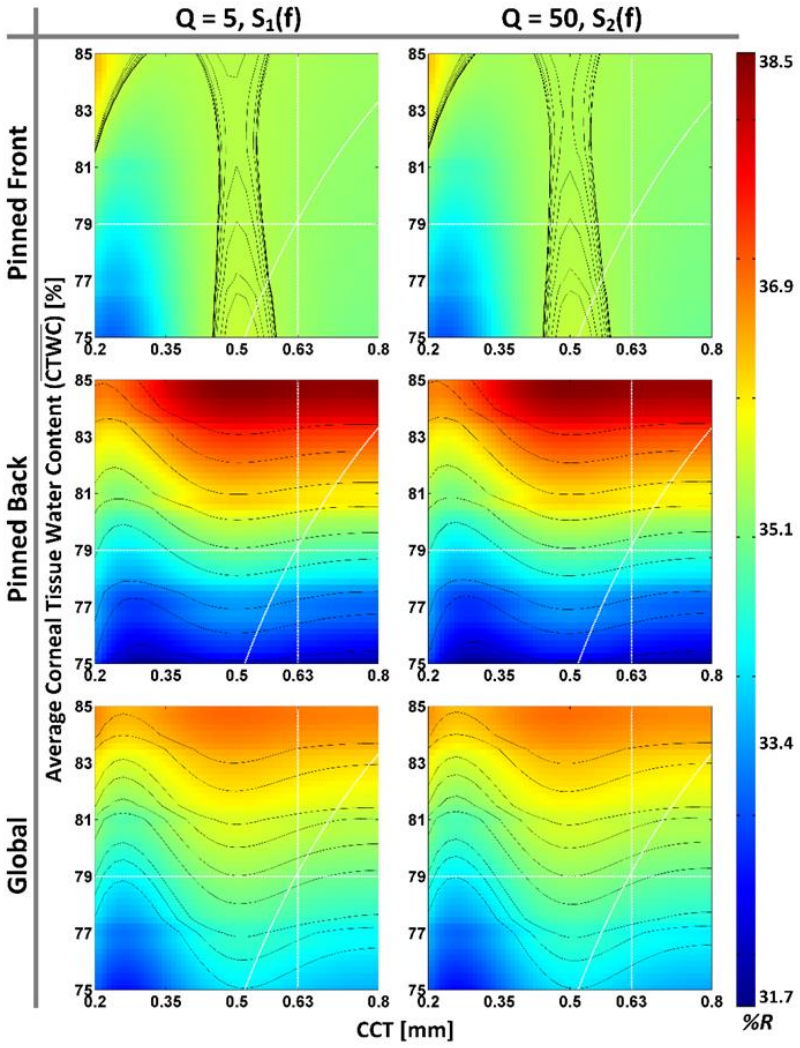

Figure 24. Reflectivity simulation of the cornea over different depth and water content at 100GHz

The black contours represent the same reflectivity with some typical values for a better grasp of how it is changed with water content and thickness. The white horizontal line draws out the simulation when CTWC is fixed at 79%, the typical value in human eyes, and how the

reflectivity changes with CCT; and the vertical while line helps draw out the simulation when CCT is fixed at 0.63 mm, the typical CCT of human cornea, and how the reflectivity changes with CTWC; the white curve is for the scenario that CCT changes together with CTWC, the curve is plotted with equation **Error! Reference source not found.**.

As is the figure, the color bar ranges from blue to red, representing reflectivity from 31.7% to 38.5%. Pinned back model has the most significant change with the variation of CTWC along the whole simulated CCT; global model is still obvious but not as strong as it is with the pinned back model; and the pinned front has the most insignificant changes with CTWC variation. It is likely that the reflecting signal mostly happens at the top of the first layer since the front side CTWC had the most influence on the results. All the simulations show that the relationship between reflectivity and CCT at constant CTWC is not monotonic. And the changing speed with CCT is much slower than that with CTWC.

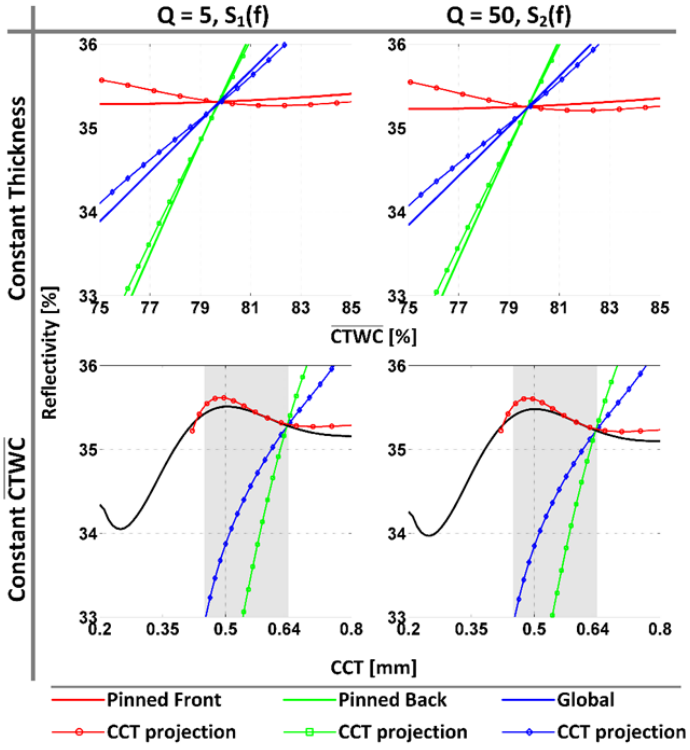

Figure 25. Replotted simulation with constant CCT and CTWC at 100 GHz

To better display the trend of simulation results, the simulations are replotted in Figure 25. With the constant thickness plots, we see rapid increase in reflectivity as the CTWC increases in pinned back and global cases while it shows as a flat curve for the pinned front model. With the constant CTWC plots, pinned back and global curves are monotonically increasing as CCT increases in the shaded area which indicates the thickness range of human cornea; and pinned front still has a non-monotonic curve within the range. There is no obvious difference between different Q factors observed.

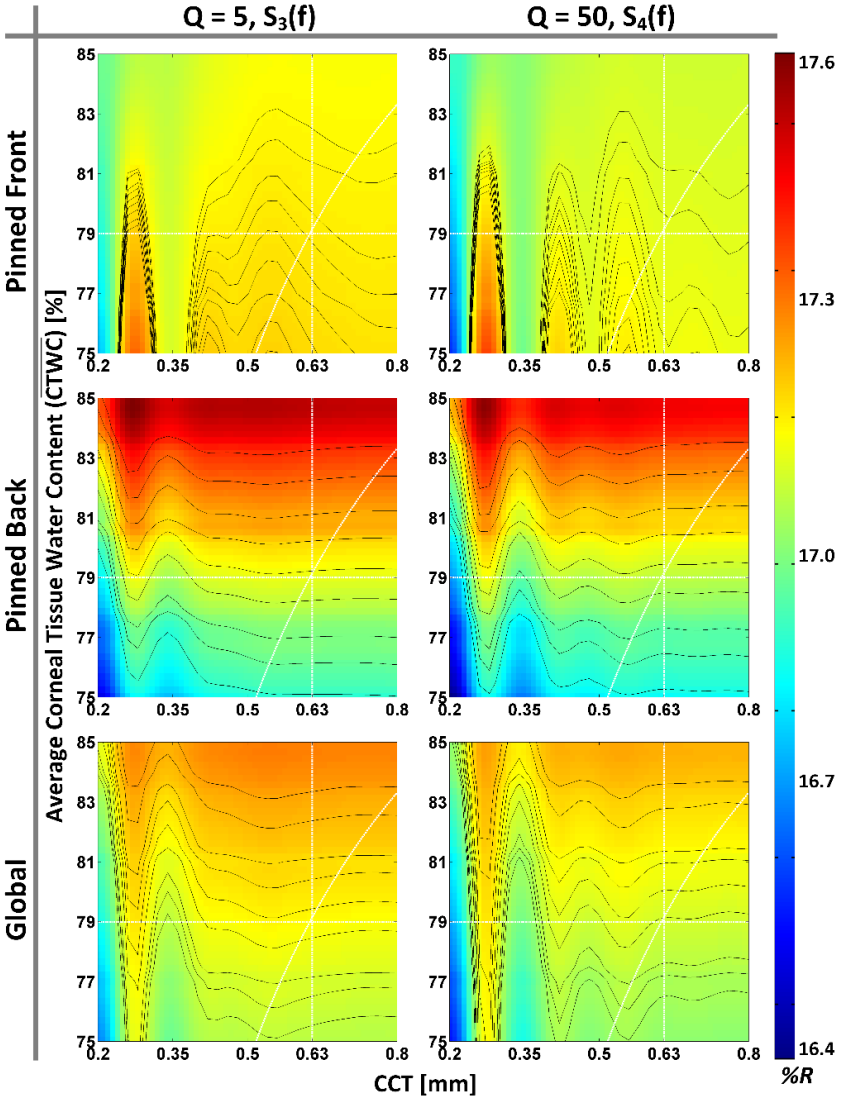

Figure 26. Reflectivity simulation of the cornea over different depth and water content at 525 GHz

The simulation results for 525 GHz are displayed in Figure 26. Similar to the results showed for 100 GHz, the x axis represents the corneal thickness, from 0.2 to 0.8 mm and y axis is the average CTWC value from 75% to 85%. The reflectivity is displayed with the same color bar among all the figures, blue to red as from 16.4% to 17.6%. The black contours, white lines are the same as they are in the 100 GHz simulation plots.

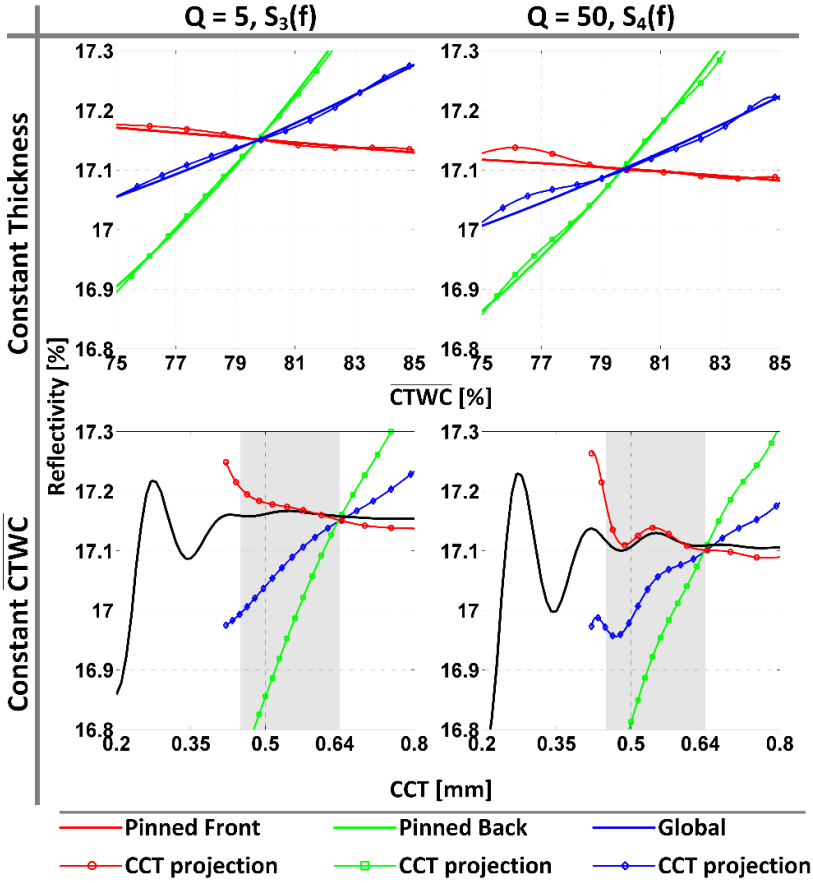

Figure 27. Replotted simulation with constant CCT and CTWC at 525 GHz

Results are replotted in Figure 27 with constant CTWC and CCT respectively. As the simulation shows, pinned back model still has the most significant change with the variation of CTWC along the whole simulated CCT; global model and pinned front model also both have obvious change with the variation of CTWC. However, the pinned front model has opposite trend from the other two models. It's likely that the reflectance still mainly takes place at the top of the

first layer. Pinned front water content dominates total reflectance energy. As the average CTWC increases, the absorption of energy by the first layer also increases and relatively the reflectance decreases. This phenomenon should have appeared in both 100 GHz and 525 GHz. However, water has much stronger absorption of 525 GHz waves than 100 GHz, so it makes sense that this negative trend is much stronger in 525 GHz. The stronger absorption is further confirmed with the stronger total reflectivity in 100 GHz simulation.

In the constant CTWC plot in Figure 27, we see periodic variations as the CCT increases, which should be caused by the etalon effect of the cornea. As the wavelength of 525 GHz (~0.272mm) is much shorter than that of 100 GHz (1.03), multiple wavelengths could appear in the thickness of the cornea (~0.6 mm) and results in a more distinct dark and bright effect as the CCT increases. And this time, waves with bigger Q values obviously had much stronger etalon effect.

This simulation verified the in-vivo experiment with rabbits.

4.4 Phase Detection Possibilities

Conventional THz thin film measurement treats water content as isotropic or uniform throughout the film thickness, which believes corneal tissue water content at every depth is changing with the same speed. However, drying dynamics is likely to create gradient from front to back. Since the front side is exposed to air, the evaporation tends to cause lower water content at the front side first and then gradually to the back side, gradually forming gradient across the depth, which is similar to the hypothesized CTWC gradient. We simulated these two models as plotted in Figure 28.

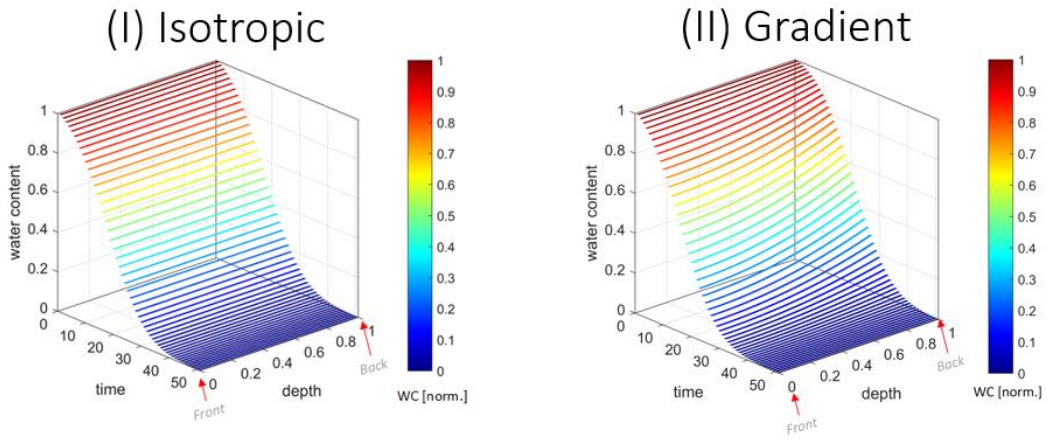

Figure 28. Isotropic and gradient CTWC change with time.

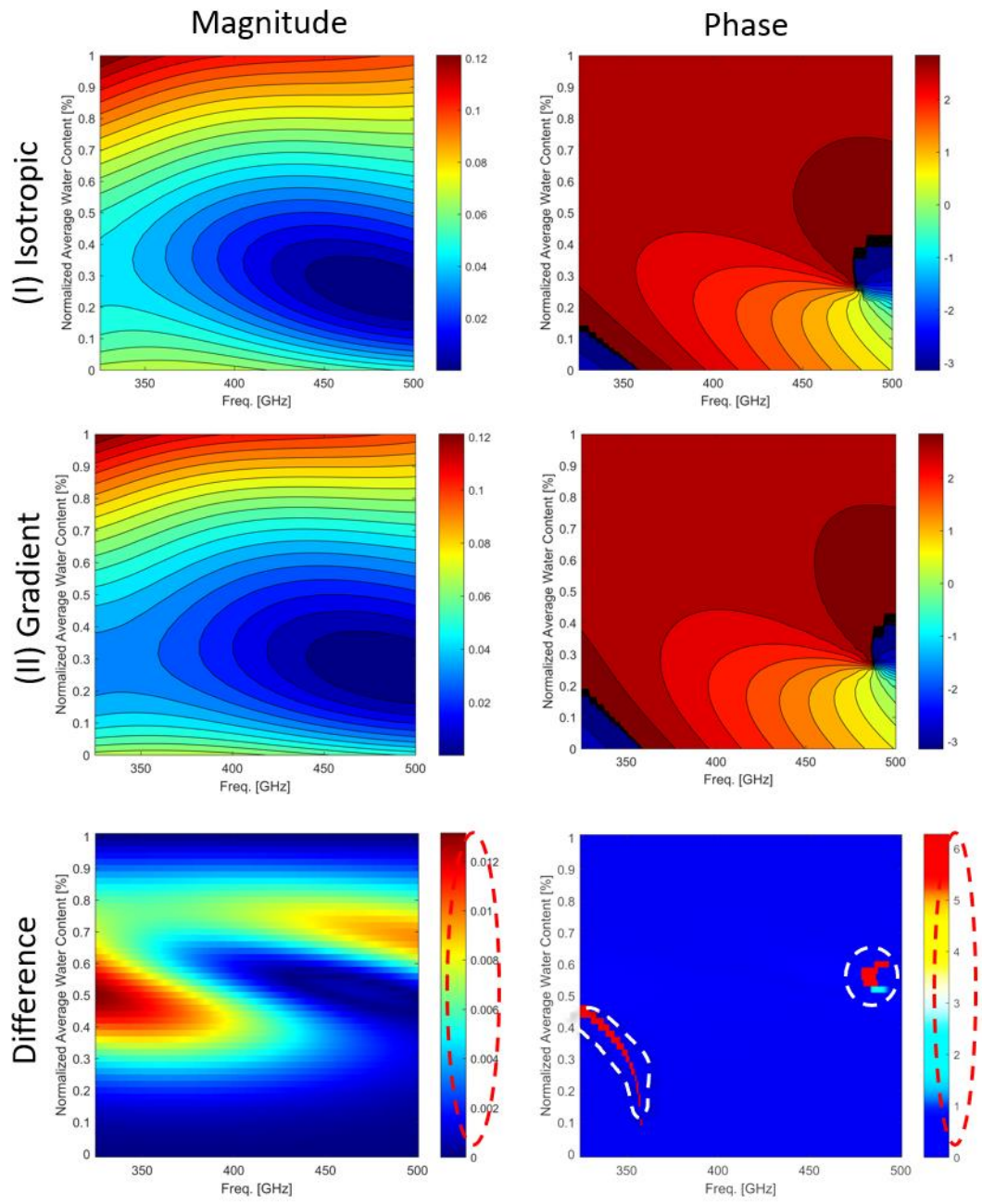

Figure 29. Frequency response with different variation models

In Figure 28, both models start with the extremum of 1, which indicates pure water scenario, and end at the extremum of 0, which stands for totally dry tissue. However, the drying processes are different. In the conventional isotropic model, as time goes by , the tissue dries up with the same speed across the whole depth. That is to say, the water content of the front and back side

always keep the same and dries out at the same time. Compared to that, in the gradient model, the front side starts to lose water content and then the water content on back side starts to drop with a slower speed. It will wait for some time for the back side to dry out after the front side water content already reaches water content of 0%. The question is, is it possible to delineate between isotropic and gradient distributions in our simulation or even experiments?

We did the simulation and plotted out the results in Figure 29. Both the magnitude and phase information were simulated. The first row in the figure is for the isotropic model, the second row is for the gradient model and the subtraction was plotted in the third row. In both the magnitude and phase plot, the x axis is the frequency ranging from 300 to 500 GHz, y axis is the normalized water content ranging from 0% to 100% and blue to red color represents 0 to 0.12 for magnitude value of the reflectivity and -π to π for the phase value respectively for both models in isotropic and gradient distribution. In the subtraction plots, the color bar range from blue to red is dependent on the values resulted in.

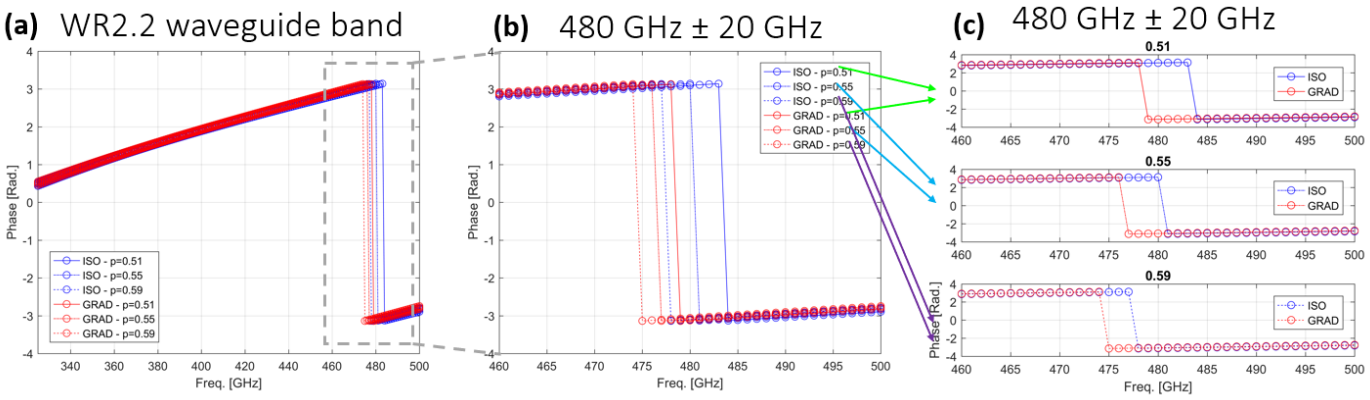

Figure 30. Detailed plot of the "Turning point"

We don't directly see too much difference between the two models in either magnitude map or the phase map. However, as we subtracted the value of the gradient model from that of the isotropic, we see a band of difference across the whole simulated frequency range. The magnitude frequency difference ranges from 0 to 0.012, which is too small for any useful

identification. We have very limited sensitivity from the magnitude map to figure out which model it is. The phase map is a totally different story. The subtraction yielded a strong and abrupt variation on the plot. The sensitivity of the phase measurement is about 2.5 orders stronger than that of the magnitude map.

If we zoom in for details around the frequency of 480 GHz, which is covered in WR2.2 waveguide band, in Figure 30, we can see the details more clearly. As in figure (b) and (c) show, the abrupt turning points appear at different frequencies for different water content and different models. The frequency difference for different water content is about 1 GHz/% and 5 GHz/% for isotropic and gradient models, which should be easy to spot in experiment.

4.5 Chalmers' work

4.5.1 Experiment setup

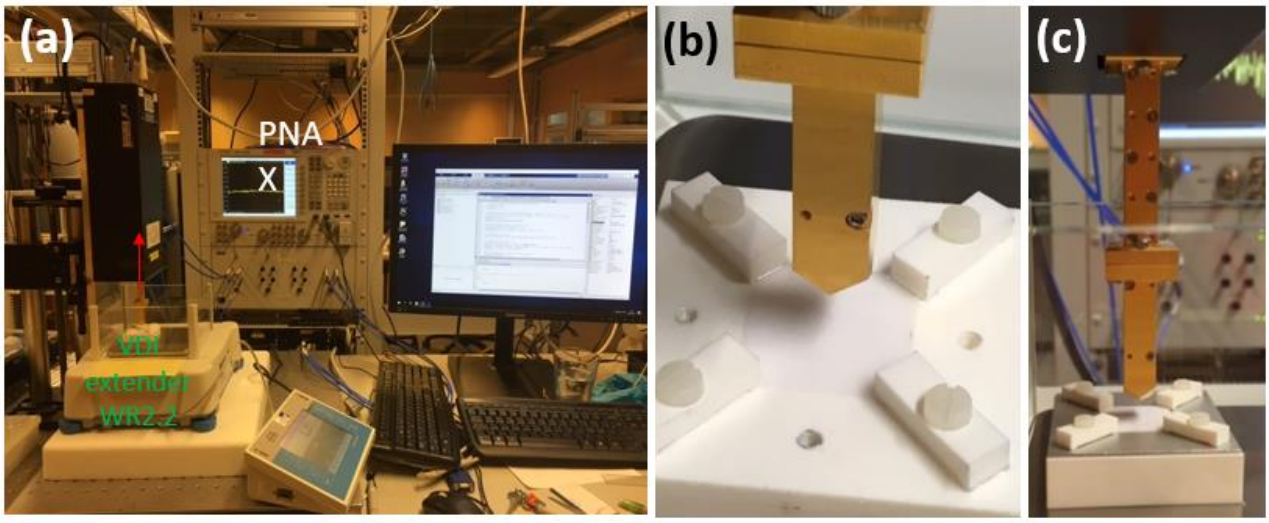

Figure 31. Measurement setup in Chalmers' lab.

So, is it possible to delineate the two distributions with the phase information of the frequency response in experiment? Our collaborators at Chalmers University of Technology (CUT), Sweden, are working on this to help us figure it out.

In their experiment, a programmable network analyzer (PNA) and a VDI extender WR2.2

were used as in Figure 31 (a). A piece if tissue was immersed with about 225 mg of tap water as the studying sample and left to dry in lab environment. The PNA was able to generate and detect a wave with the frequency ranging from 325 GHz to 500 GHz. Calibration plane was placed at the rectangular waveguide, just before the antenna. The antenna-sample distance was set to be about 6 mm while measurement. Measurement was done with a metal and plastic baking separately, as in Figure 31 (c) and (b).

4.5.2 Results and Problems

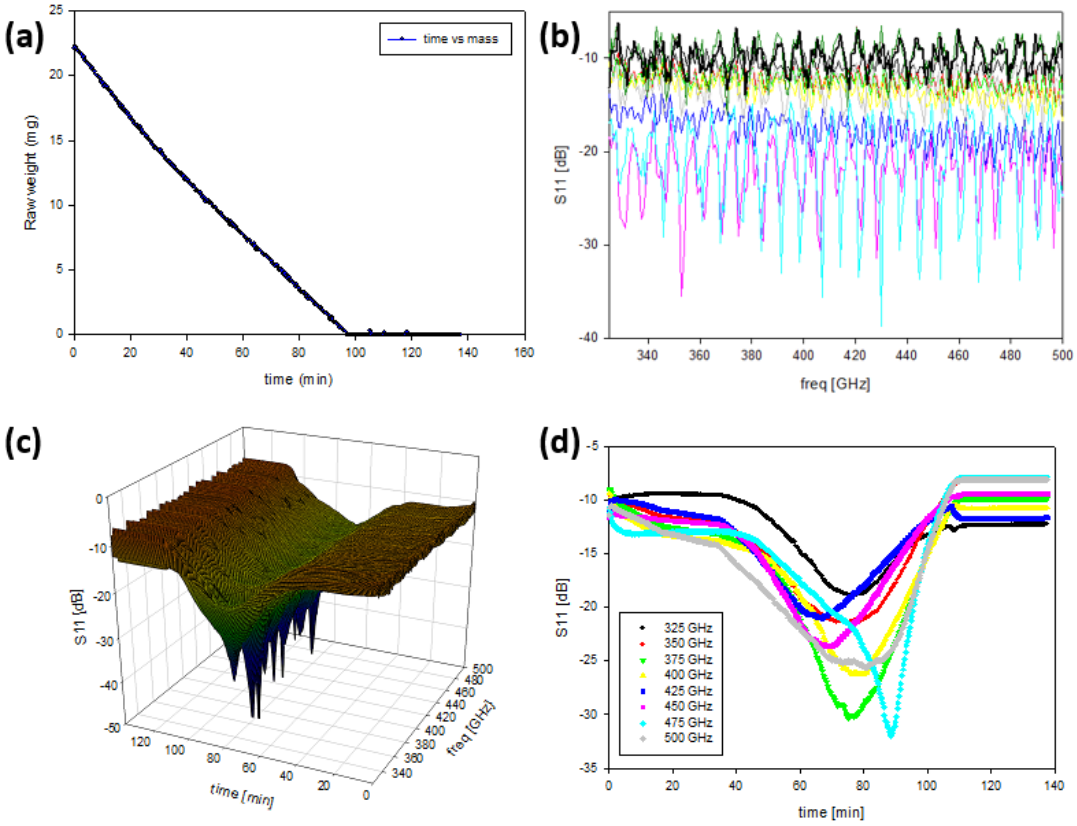

Figure 32. Measurement results of the frequency response with plastic backing.

Eight sets of point measurement were taken every 15 min during two hours, by sweeping the frequency from 325 GHz to 500 GHz. The water immersed tissue was placed on an electronic scale for the measurement of weight change while experiment. Figure 32 (a) plots how the raw weight changes with time. The eight S11 measurements were overlapped with different colors in

figure (b). The x axis marks the frequency range and S11 values are shown as dB with y axis. To better visualize the results, the data was replotted in 3-D format in figure (c) and replotted with the x-axis of time and curves of different frequencies in figure (d). As in the figures, the frequency dependent property is obviously shown here but the intense periodic variation, which is believed to be the standing waves between the antenna and the backing plate, is severely obscuring the real information. This standing wave effect was observed with the metal backing as well.

4.5.3 New testing system for Chalmers

The severe standing waves are considered to be caused by the confocal behavior inherited in the testing setup, and verified with standing wave analysis. UCLA was asked to help solve this problem.

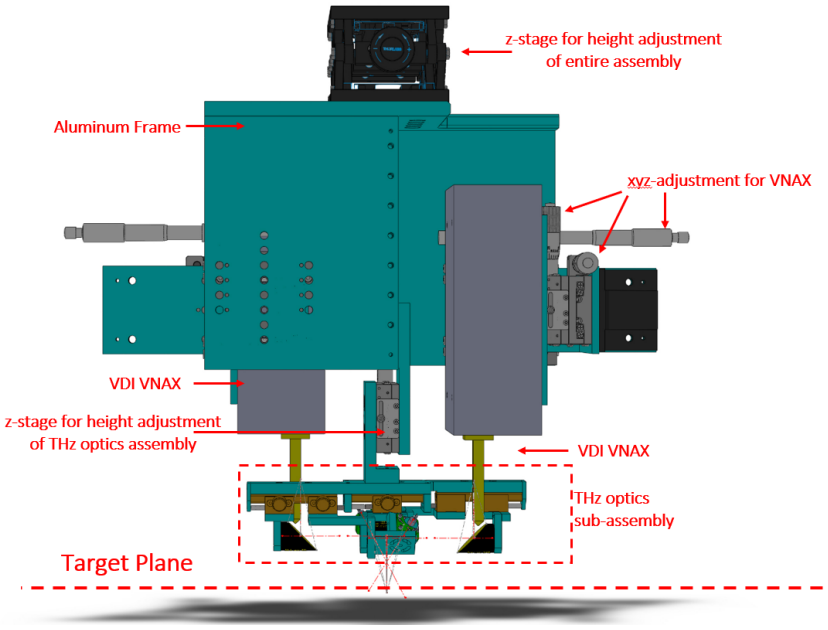

Figure 33. Design of the new testing system for CUT.

As shown in Figure 33, a new system was designed by UCLA to exacerbate the confocal behavior with the hope of reducing standing waves. Two copies of them are being machined and built. One will be sent to Chalmers and the other copy will be kept with UCLA researchers for remote assistant. Experiments will be redone with this new system and hopefully a precise

mapping between relative phase data and water content gradient will be obtained.

Another design in Figure 34 for water backing of the sample was completed to help mimic the aqueous humor of the eye, which is the real backing material for the cornea. In this design, an opening of the size of 5 mm is cut on the top of an empty ball, which is connected with a cylinder with a tube. When a cornea phantom is placed on top of the opening, this design not only allows a water backing of the sample but also allows the adjustment of backing pressure with the height of water in the cylinder.

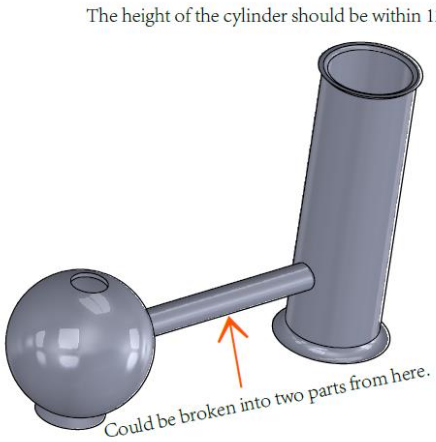

Figure 34. Backing setup to mimic the aqueous humor of the eye.

CHAPTER 5: **THz Optics Design**

5.1 Off-Axis Parabolic Mirrors

Parabolic mirror is a reflective mirror used to collect electromagnetic waves or mechanical waves, for example light and sound. Its surface is generated by revolving a parabola around its axis. Off-Axis Parabolic mirror (OAP) is simply a side section of a parent parabolic mirror, as shown in Figure 35 (a). OAPs have some very useful properties. First, when collimated light incident from the planar plane to the OAP, it will get focused at the focal point of the OAP mirror. On the other hand, a source with spherical wave fronts that located at the OAP focal point will get collimated after the OAP reflection. This provides it the ability to switch from its clear aperture pane to focal plane easily. Second, only a part of parabolic mirror is used, which not only makes sure the incident light and outgoing light won't overlap, and also avoids possible interference between the focus and any mechanical parts. This characteristic makes it extremely easy to access the focal point for placement of sources, detectors and other associated hardware mounting. Third, OAP has very high energy collection efficiency and also could avoid chromatic aberrations even over very wide wavelength range. For all the above listed qualities, OAPs are the most frequently used optical element used in our THz design. The 90 degree OAP mirrors usually look like the mirrors shown in Figure 35 (b).

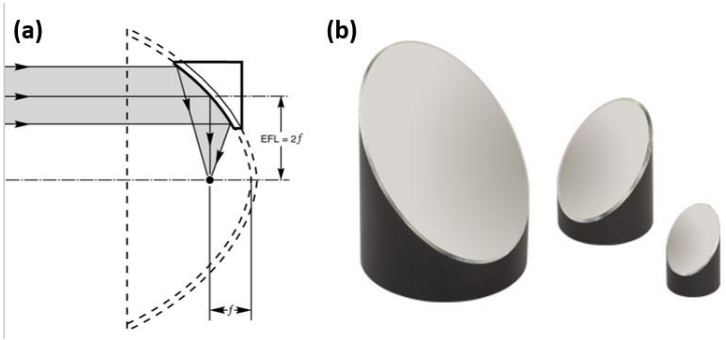

Figure 35. OAP mirrors

However, OAPs can also be difficult to align and hard to obtain good imaging quality when used improperly. For example, if the incident beam is not parallel to the optical axis, comatic aberration will be produced because of the angular displacement. Beam distortion and beam center shift are also commonly seen in OAP applications. As shown in Figure 36 [81], when a Gaussian point source radiates from the focal point of the OAP and incidents to the mirror, the reflected outcoming collimated beam will be distorted and undergo an obvious center shift.

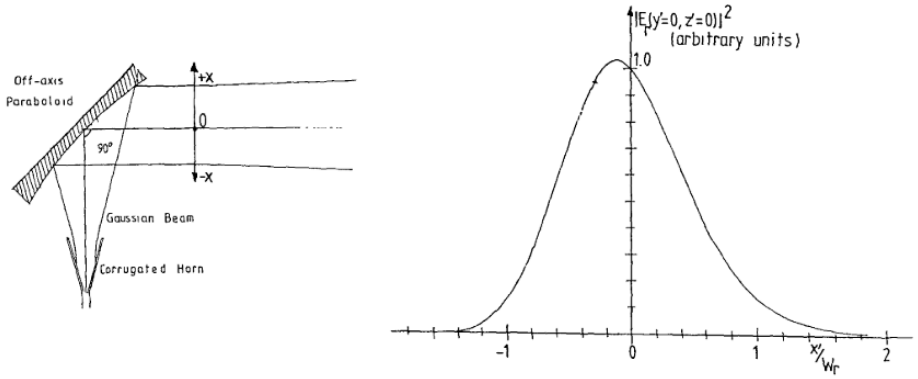

Figure 36. Reflection of a Gaussian beam from an OAP

5.2 Beam Center Shift and Compensation

5.2.1 Single OAP System

ASAP, or the Advanced System Analysis Program, is optical simulation software used in optical engineering. It is a non-sequential ray tracing tool that can handle both incoherent and coherent light sources. In our series of work, we found it a very powerful ray tracing tool for our THz optics system design. However, the fact that the size of OAPs used our system is only within ~100 wavelengths of THz radiation, made it really hard to simulate with coherent sources, so we mainly utilized incoherent sources here. Despite of this, it still gives us very good simulation results.

Following the interesting thread of Gaussian beam center shifting, we successfully reproduced the center shift in our simulation with ASAP: NextGen (Breault Research Organization, Inc). As shown in Figure 37 (b), a Gaussian point source at the focal point of the OAP (diameter = 25.4 mm, effective focal length (EFL) = 25.4 mm) radiates, incidents on and get reflected by the OAP. We put two planes in the simulation for observation, with the first plane 3 mm away from the source and the second plane one EFL away from the center of the OAP. As seen in the figure (a), the point source before the OAP presents a perfect Gaussian beam profile and locates right on the OAP's focus and geometry center connecting line. After the OAP, the beam profile is distorted and the center is also shifted to one side a little bit. This intuitive result made it fun for some further investigation.

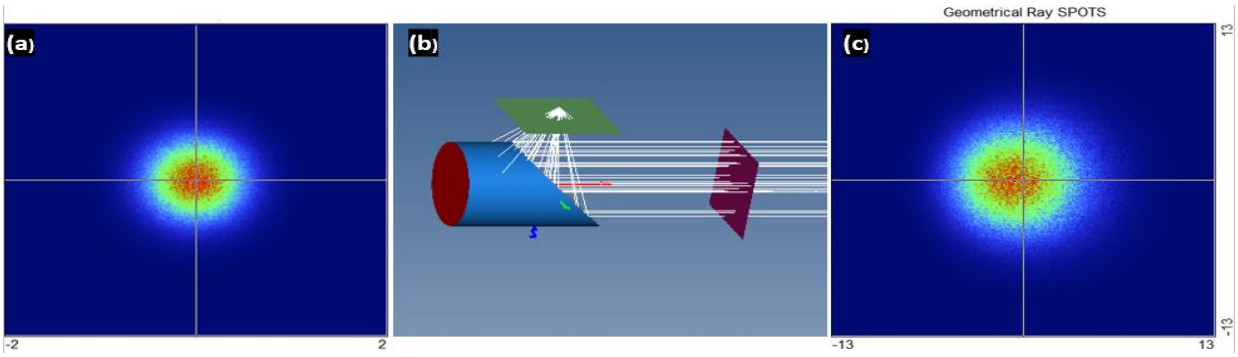

Figure 37. Demonstration of center shift of Gaussian beam from OAP

5.2.2 Double OAP System

If a number of OAPs are used in an optical train, it is necessary to understand how the beam is getting distorted in the propagation. The next step is to expand the simulation from single OAP system to a double mirror system. We computed two scenarios as shown in Figure 38 (I) and (II). In this simulation, we took the same OAP used in single mirror simulation, of which the diameter and EFL are both 25.4 mm. A Gaussian point source spreading at 5 degrees with 10E7 is adopted. In the two scenarios, the optical axis of both OAPs overlap and the clear apertures face each other while the centers are 2 EFLs away. The focal points of two OAPs face in opposite directions in the first simulation while the focal points are in the same direction in the second scenario. Three planes are placed right after the source, in the middle of the two mirrors and right before the detector plane respectively. As we can see in the figure, both the source profile and the profile after the first mirror presented the same result as we had in the single mirror simulation, not surprisingly. What interesting is the beam profile after the second mirror. In the setup with focal points pointing in different directions, the shift of center was exacerbated while it was canceled out and the center shifted back in the second setup. This simulation tells us that the beam center shifting effect caused by OAP asymmetricity could be minimized or even canceled out in a two-mirror system if the mirrors are configured properly. As a result, utilization of paired OAPs with the second setup in an optical train could minimize the side effect caused by OAP's asymmetricity. In the following sections, we will call the first setup as uncompensated setup and the second as compensated setup for convenience.

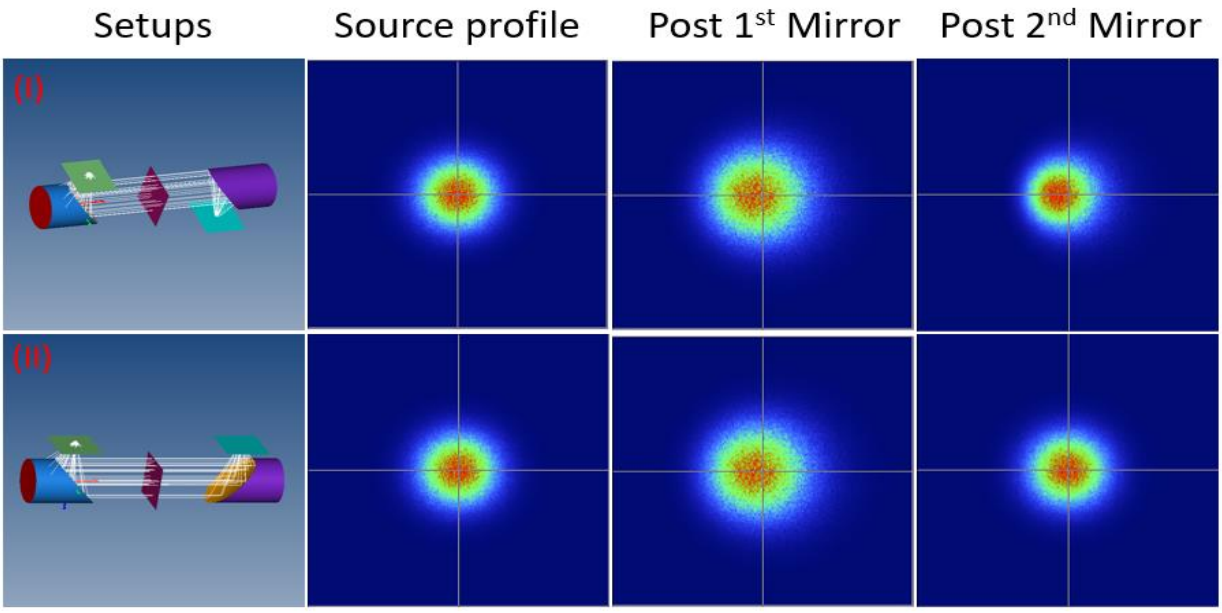

Figure 38. Two-OAP system beam center shift demo

5.2.3 Compensated vs Uncompensated Complex Systems

With this powerful tool, it is interesting to see how this finding will affect the overall imaging quality in complex THz imaging systems. In this section, we picked two systems for comparison. One is a system that was developed by the group years ago and there were several papers have been published [31], [46], [49], [82]. The second system was developed in my early PhD term to verify some optical properties of THz imaging systems. However, it was a pity that we didn't do any further experiments with it but maybe in the future. Back to the simulation, in the first system as we can see in Figure 39 (a), we have four OAPs numbered from 1 to 4. OAP1 is for source collimation as the source is colocated with the focal point of OAP1 and pointing towards the mirror. OAP2 and OAP3 function as the source focusing and reflected energy collimating mirrors. The two mirrors both face in the opposite direction where the THz beam coming from OAP1. In order to overlap the focal points of OAP2 and OAP3, the two mirrors are rotated along their optical axis towards each other. OAP4 is to focus the reflected energy from OAP3 and feed it to the detector. In order to avoid the physical interference of the source and detector, OAP4 is rotated for 90

degrees towards outside. As this is the first system developed in our group and given the information we had in previous two sections, we might easily notice that this system has employed several configurations that might decrease the imaging quality of the system.

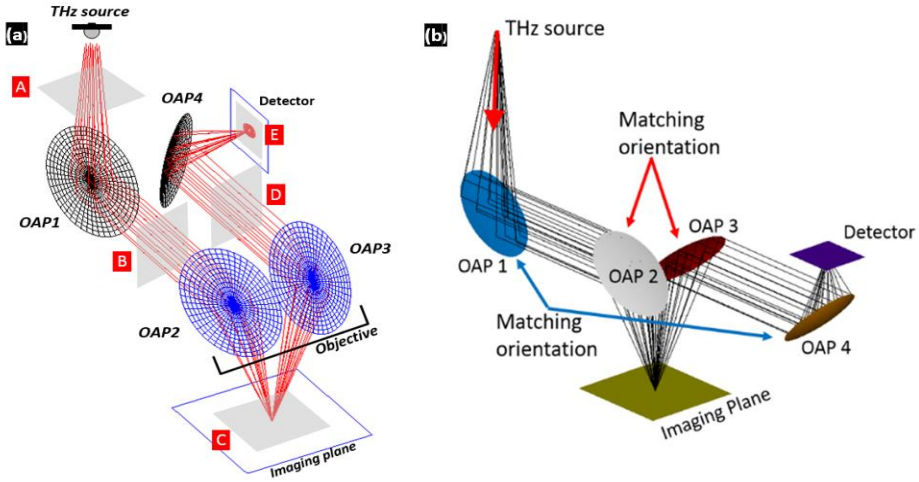

Figure 39. Compensated VS uncompensated complex systems

As the OAPs were only oriented in random directions that would realizing their basic focusing and collimating functions, the effects of center shifting and beam distortion were never taken into consideration. As shown in the layout, both the pair of OAP2 with OAP3 and the pair of OAP1 with OAP4 are in a uncompensated setup, which would accumulate the distortion and center shifting effect. Especially the pair of OAP1 with OAP4, based on some other studies [81], the rotation of OAP4 will make the polarization even worse and hence decreasing the coupling efficiency and imaging quality of the system. On the contrary, we tried to employ the compensated setups when possible while designing the new 2-D scanning THz system. As shown in Figure 39 (b), we tried to orient two objective mirrors, OAP2 and OAP3, in the compensated manner and made them facing towards opposite directions, which also gave us the space to mount source and detector and their associated hardware in preferred positions without any interference. Now OAP1 and OAP4 are also setup in the compensated manner.

In this round of simulation, a uniform emitting disk with diameter of 3 mm and an spreading angle of 5 degrees is used here for more intuitive observation of beam profile distortion and

shifting. In both scenarios, 10E7 rays emitting from the disk that located at the focal point of OAP1 incident on the mirror and get collimated. The wave propagates, incidents on OAP2 and was redirected and focused to the imaging plane which overlaps in height with both focal points of OAP2 and OAP3. Signal was reflected by the imaging plane and directed to OAP3, and again collimated and directed to OAP4, which is responsible for focusing the beam and feed it to the detector. A observation plane is placed at the detector plane and signals are acquired. As shown in Figure 40, left image is for compensated system and right for the uncompensated one. As the source is an average round emitting disk, the left image could be interpreted as a perfect image of the source we can get in the compensated system. While on the other hand, image of the source we got for the uncompensated system is dispersed and spread to a larger area than it in the compensated counterpart, which could affect the energy collection efficiency.

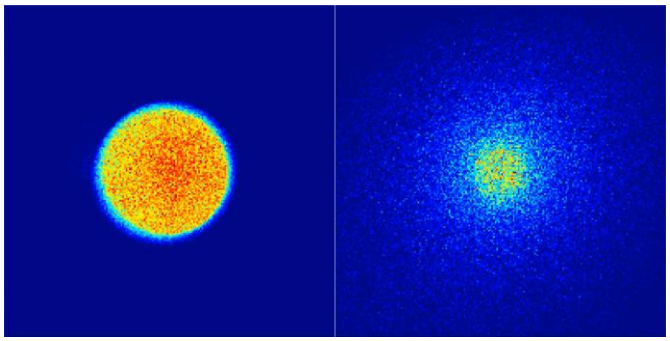

Figure 40. Detector plane image comparison while aligned

While with the two systems already setup in ASAP, we decided to explore how it will affect the images on the detector plane while displacing the imaging plane off the focal plane of the objective mirrors. The displacement was varied from +7 mm to -7 mm with the step of 0.25 mm. 5 typical scenarios are selected and displayed in Figure 41. They are the images on the detector plane when the displacement values are +7, +1.5, 0, -1.5, 7 mm respectively. As already seen in above, when the imaging plane is perfectly aligned with the focal plane of the objective mirrors, the compensated system yields a much better image of the source than that of uncompensated

system. Starting from +7 mm displacement, the compensated system has nearly no energy collected in the red circled area, where energy could be collected by the detector in the real world, while for the uncompensated system, dispersion of the light forms a light background across the whole plane. As the displacement becomes smaller, energy starts to shift into the red circle in the compensated system, while it's more likely to move and gather into the red circle for the uncompensated case. After the image plan reaches the focal plane and then leaves away from it, the energy moves out of the red circle in the compensated and moves disperses out of red circle in the other case. From this dynamic simulation, we can see that as the imaging plane is displaced from the focal plane, the energy collection inside the detector (red-circled area here) in the compensated system is faster and stronger than its counterpart here. We expect better spatial resolution and stronger signal (or signal to noise ratio) in the compensated system than that of the uncompensated. However, some ghost light appears in the compensated system for some unknown reasons, which could be the reflecting by the constructing edges.

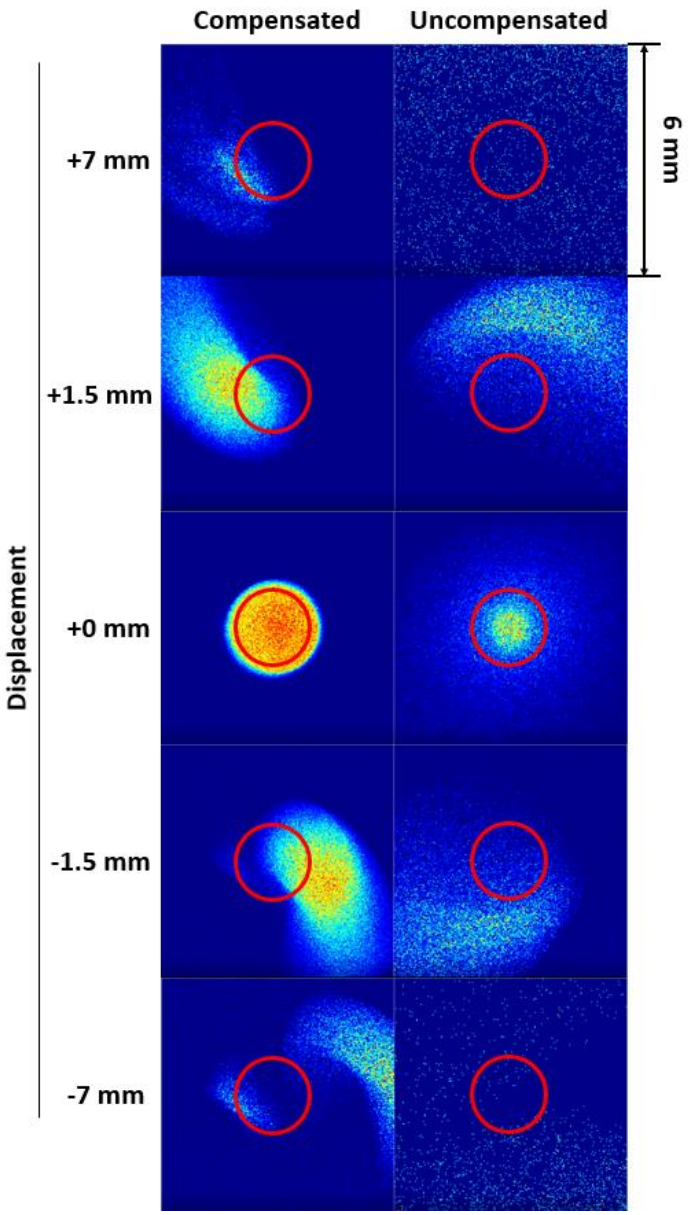

Figure 41. Dynamic comparison while displacing imaging plane

5.3 Focal Length Influence on Imaging Behavior

5.3.1 Comparison On Different EFL Combinations

While the two systems already setup in ASAP, we decided to explore the influence of different focal lengths of the OAPs on the imaging behavior. Since OAP2 and OAP3, the objective mirrors, are fixed in the system and focal points of which should overlap, the focal length of these two mirrors should be identical. OAP1 and OAP4 are for source collimating and energy focusing, they are also a pair of counterparts, so we only need to evaluate one of them. Hence, in the following simulations we varied the EFLs of OAP1 and OAP2(OAP3) among values of 25.4 mm, 50.8 mm and 76.2 mm, and listed the results as it in the comparison panel shown in Figure 42.

OAP1: 25.4 **OAP2,3:** 25.4	**OAP1:** 25.4 **OAP2,3:** 50.8	**OAP1:** 25.4 **OAP2,3:** 76.2
OAP1: 50.8 **OAP2,3:** 25.4	**OAP1:** 50.8 **OAP2,3:** 50.8	**OAP1:** 50.8 **OAP2,3:** 76.2
OAP1: 76.2 **OAP2,3:** 25.4	**OAP1:** 76.2 **OAP2,3:** 50.8	**OAP1:** 76.2 **OAP2,3:** 76.2

Figure 42. Comparison panel with parameter legend

The simulation results for scenario that imaging plane well aligned with objective focal plane is displayed in Figure 43. As we can see from the simulation, all nine combinations of different EFL present a good spherical image of the source, while the image size varies according to the EFL of OAP1. As we consider the following OAPs and OAP1 as one whole optical element and assign it a focal length of f2, and assign OAP1 a focal length of f1. The simulation shows that in this system it still agrees with the basic magnification equation for two-lens system:

$$m = \frac{f_2}{f_1} \tag{15}$$

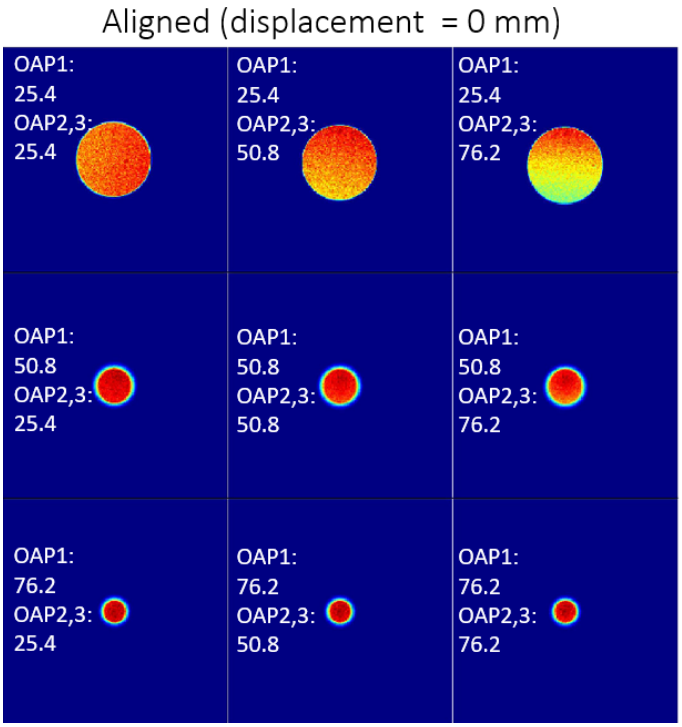

Figure 43. Aligned simulation results for different EFL comparison

Considering the EFL of OAP4 is 25.4 mm used in our simulation and pair of OAP2 and OAP3 doesn't contribute to the magnification variation, we can directly treat this system as a two-OAP system of OAP1 and OAP4. According to equation (15), the image spot size should decrease as the EFL of OAP1 increase, which is verified here in the simulation. The size of the image spot is one time, a half and a third of the size of the source when the EFL of OAP1 varies respectively. The different focal length combination leads to different imaging size on the detector plane, but this still falls into the traditional magnification theory. In real experiment, we want energy as concentrated as possible in the location of detector aperture for better coupling efficiency, so it looks like longer focal length of OAP1 is a better choice. Hence, higher directivity of source is always preferred.

In this simulation, we also tried to vary the displacement of the imaging plane as we did in the previous section. The displacement still varies from +7 mm to -7 mm with the step of 0.25 mm.

A dynamic video of the change was created and a snap in the beginning when the displacement equals +7 mm is shown in Figure 44. From the dynamic video, we can clearly see the shift of energy center by the displacement of imaging plane speeds up as EFL of OAP1 decreases. That is to say, shorter EFL of objective mirrors will exacerbate the confocality effect of the system.

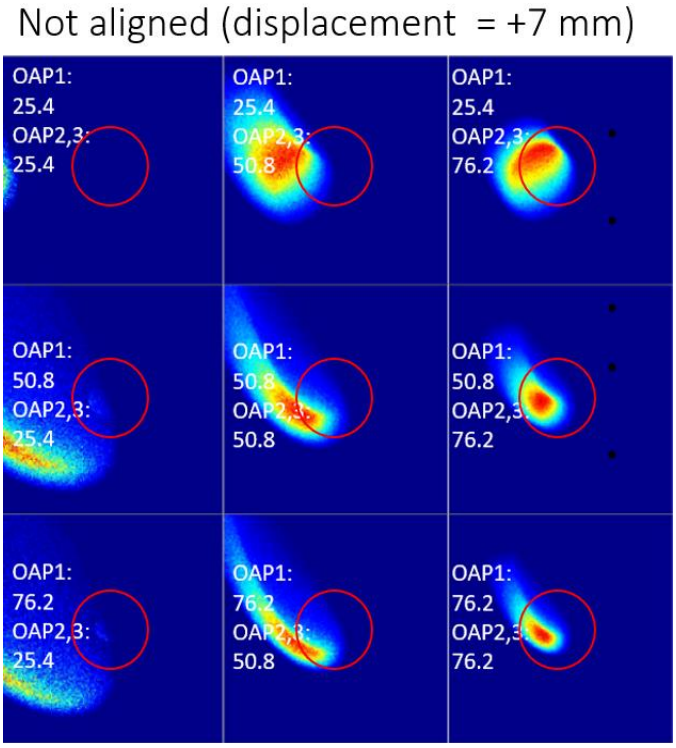

Figure 44. Displaced simulation results for different EFL comparison

This effect could be a double-edged sword. For applications, you want bigger depth of field to decrease the alignment sensitivity and make up for patient movements, it's a better choice to get a OAP with longer focal length. On the other hand, in some applications, if you want smaller depth of field, for example, like Chalmers' measurement system, confocality might be able to help them get rid of the standing waves, objective OAP with smaller focal length should work better for you.

5.3.2 Depth of Field and Knife-Edge Measurement

In our lab, we have systems of both setups discussed above. Here, I took some measurements with the second system I built in my first year in the lab. The Depth of Field (DOF) and knife-edge response were measured. As we can see in Figure 45, we scanned the displacement from -30 mm to 30mm and got the Full Width at Half Maximum (FWHM) of 2.0, 4.3, 11.2 mm for 1-inch, 2-inch and 3-inch mirrors respectively. It agrees well with the prediction we had in previous section. For the older system, previous measurement show that the DOF are 0.8, 4 and 11.7 mm for 1-inch, 2-inch and 3-inch mirrors respectively.

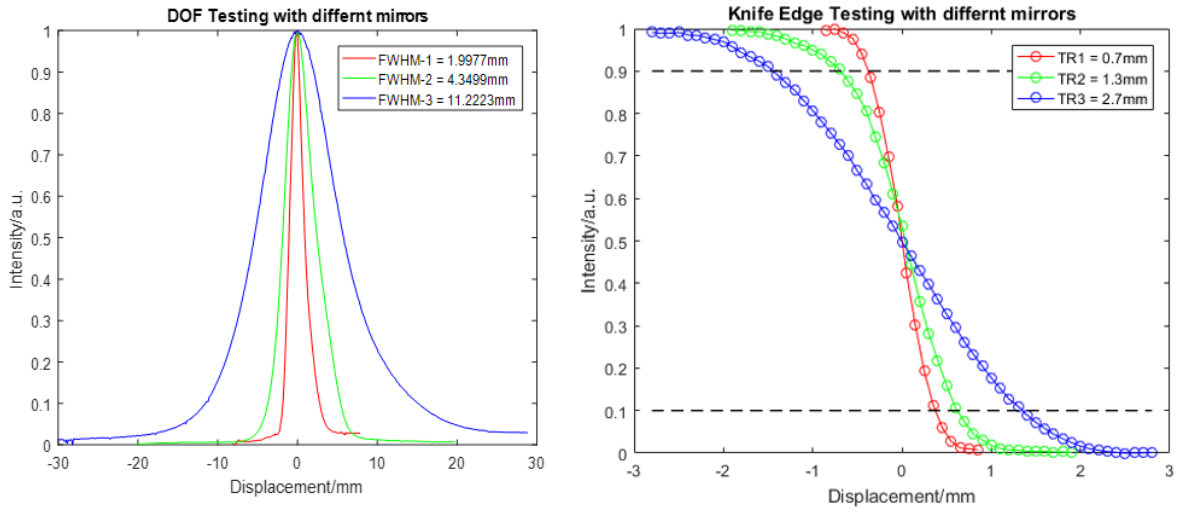

Figure 45. Experiment measurement of real system

The knife-edge measurement as shown in Figure 45 actually reflects the spot size on the imaging plane. According to equation below [83]

$$X_{10-90} = 1.28\, w_x \tag{16}$$

The spot sizes of the system on the target plane are 0.54 mm, 1.02 mm and 2.11 mm respectively for the EFL of objective mirrors to be 1 to 3 inches. Since we don't know the exact size of the source, so we have no idea what the real magnifications are. However, the ratios agree with our 2-lens magnification theory. The minor errors might due to the tilted imaging plane to the real focal plan of the objective mirrors and possible lens misalignment.

5.4 Angular Scanning System Design

5.4.1 Design of Angular Scanning System

With all the knowledge and information obtained from previous study, we can now start our design for the angular scanning system. As mentioned in the background work, one potential weakness of the rectilinear scan design is the relatively large transverse displacement necessary to scan a comparatively small angular FOV on the cornea. This relationship creates a limitation on image acquisition rate that may hinder translational feasibility.

A more efficient scanning mechanism in terms of the ratio of scanning optical translation with beam location on target is displayed in Figure 46. This design was motivated by scanning microscopy (e.g. confocal microscopy, optical coherence tomography) which typically employ galvometric or resonance mirrors to transform translation in the angular domain at some intermediary plane to transverse, planar translation at the imaging plane.

Standard optical system design decouple the azimuthal and elevation scan directions to separate planar mirrors whose axes are mutually orthogonal [84]. Due to the comparatively short Rayleigh lengths at the design wavelength, the angular scanning was designed with a single gimbal-mirror-like optical translation where rotational motion is about the center point of the mirror surface. This design allows for an overall shorter optical path compared to the rectilinear scanning design

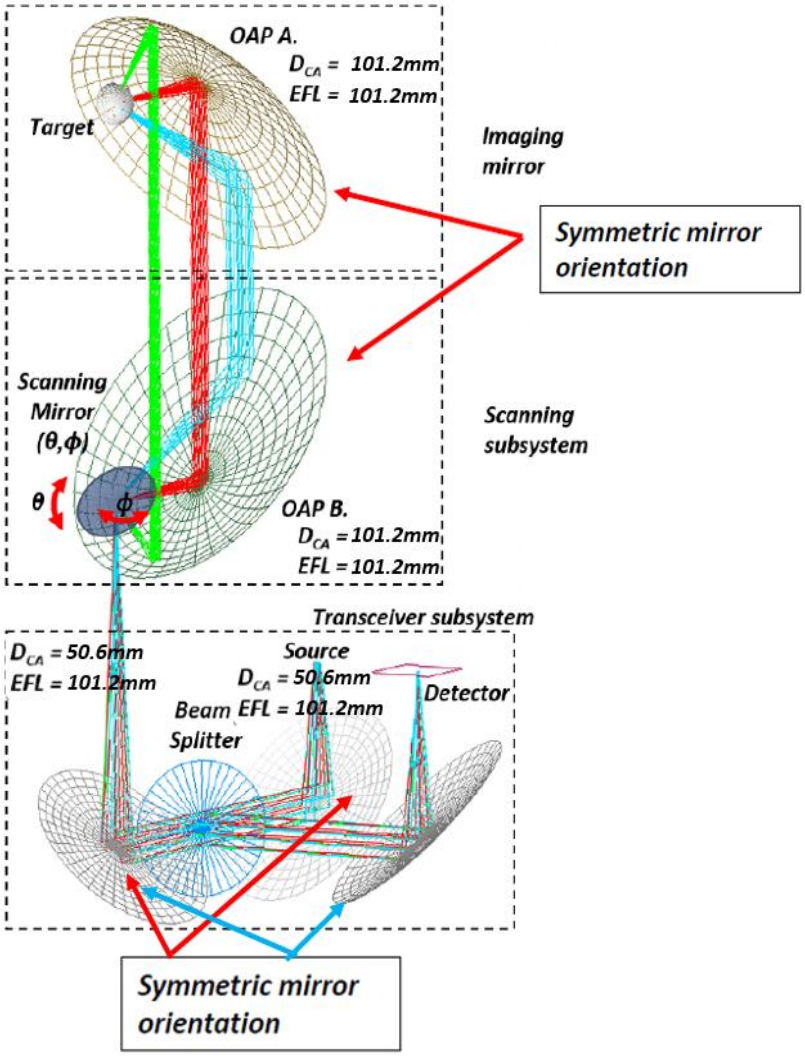

Figure 46. Double mirror, angular scanning imaging system design.

As discussed previously, transverse translation of a collimated beam results in the angular scanning of a focused beam at the target plane. In this angular implementation a second parabolic mirror, identical to the focusing objective, is added to the beam. The THz beam is focused onto the surface of the angular scanning mirror and then the diverging beam is directed to varying sub-segments of the added parabolic reflector. This angular scan results in the transverse translation of a collimated beam in the clear aperture plane of the focusing OAP.

There are two key benefits to this orientation. (1) Angular scanning at moderate speeds can produce rapid transverse translation in the collimated beam path and the total image acquisition

time can be greatly reduced. (2) The collimated beam diameter is a function of scanning angle resulting in a partial optimization of beam parameters with respect to the spot size on target. In the rectilinear scanning design (constant collimated beam diameter), larger beam diameters at the far edge of the OAP minimized the spot size while smaller beam diameters at the near edge of the OAP minimized the spot size[48]. This behavior is intrinsic to the angular scanning design as evidence by the ray paths will be talked in system analysis chapter.

As shown in the configuration, we oriented the two big OAP mirrors in the compensated “tip-to-tip” setup, and the same setup for the small mirrors for source, detector and focusing mirror for the rotating mirror. As the beam travels first from the source to the small OAPs and to the rotating mirror, the collimating mirror from the source and focusing mirror to the rotating mirror could be treated as a pair, which is also oriented in the compensated manner. As the beam travels back, the collimating mirror (as focusing previously) for spreading wave and focusing mirror for the source are also oriented the same way, even with the reflection of the half passing half reflecting beam splitter in the route. As you may noticed, we also employed longer focal length (4-inch) for the big objective mirror for less sensitivity on the alignment.

5.4.2 Simulation of Angular Scanning System

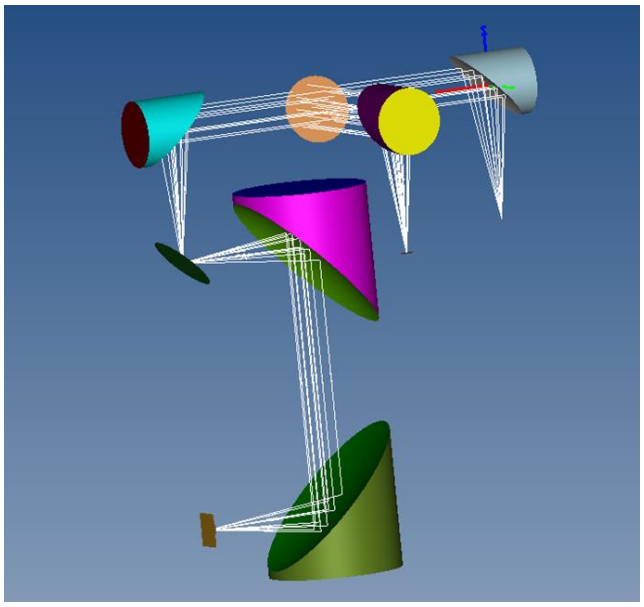

Figure 47. System reconstruction in ASAP

To verify our optical setup, the system is reconstructed in ASAP and a complete ray tracing was simulated. In the simulation, we used the same setup and parameters as they will be in the real world, as shown in Figure 46: three collimating and focusing OAPs (DCA=50.8mm, EFL=101.6mm), one 50/50 beam splitter, one reflecting scanning mirror and two OAPs (DCA=101.6mm, EFL=101.6mm) as imaging mirrors. The source is set to be an emitting disk with radius of 1 mm and half angle of 10 degrees at 460 μm wavelength. 65 by 65 iterations of simulations were gone through by varying the angles of the rotating mirrors from $\theta \in [-40°, 24°]$, $\varphi \in [-32°, 32°]$ with 1 degree interval in each direction, which covers the real world scanning range, $\theta \in [-37°, 23°]$, $\varphi \in [-30°, 30°]$. In each iteration, the rays followed the path as it is in the real world and an image of the source was acquired at the detector plane.

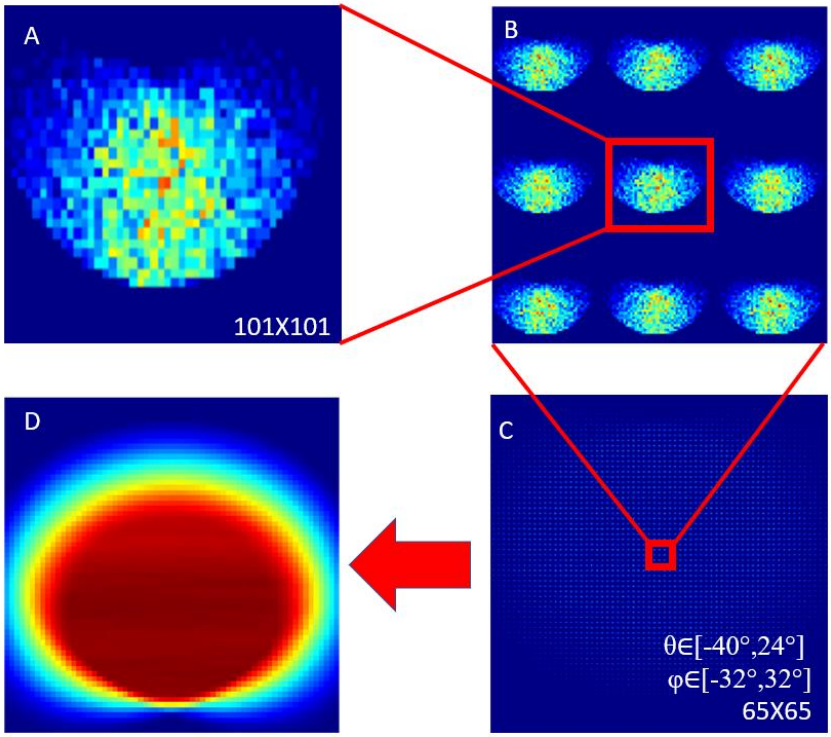

Figure 48. Simulation results on angular scanning system

In Figure 48, A is the image of the source collected at the detector plane. And by varying the rotating position of the mirrors, we can get the source images at the detector for different scanning angles, locally shown as it in B. I simulated 65 by 65 scenarios as it could be in the real world, and put them together to get image C. That is to say, every sub-image in C represents a complete simulation of the image of the source on the detector plane. The whole big picture has 65 by 65 images of the source at different angles ranging from $\theta \in [-40°, 24°]$, $\varphi \in [-32°, 32°]$ with 1 degree interval in each direction. By summing up the 101 by 101 values in each sub image, and treat it as a single pixel value. Combining all the simulation sub-images' sum, I got the simulation for scanning across the whole field of view, as shown in figure D. D reflects what the image that we can get will look like when the beam sweeps across the whole field of view. From this picture, we can see a very homogenous and flat image of the target ball across the whole field of view.

The ray tracing confirms the feasibility of the new setup and indicates a flat imaging of our sphere target, which decreases the coupling efficiency variability to an acceptable range.

5.4.3 Comparison with Rectilinear Scanning System

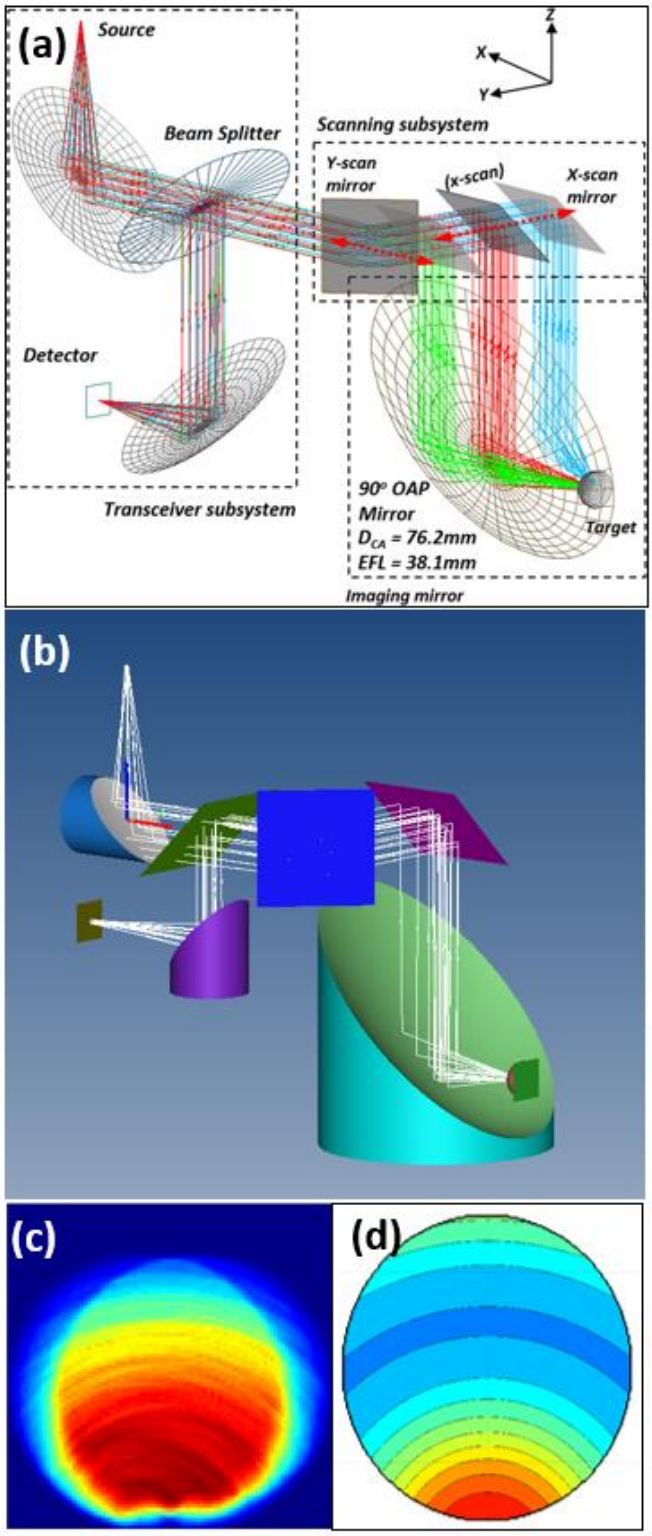

Figure 49. Complete simulation of rectilinear scanning system

Since we are now able to do full path simulation for a sphere target with a complex THz scanning system, I got very curious about what the simulation results will be for the previous rectilinear scanning system.

In Figure 49, figure (a) illustrates the setup of the system. Plane mirrors “x-scan” and “y-scan” are mutually orthogonal. Linear translation enables transverse positioning of collimated beam within the OAP clear aperture. The Rectilinear scan of the collimated beam in the clear aperture plane produces an angular scan in the focal plane. And the illumination beam is normal at all scan positions to the target sphere surface. The reflected beam path is collinear with the illumination beam path.

Figure (b) is the reconstructed rectilinear system within ASAP. We still employed all the parameters as they are in the real world. The source is set to be an emitting disk with radius of 1 mm and half angle of 10 degrees at 460 μm wavelength, same as it in the angular scanning system simulation. The mirrors “x-scan” and “y-scan” mirrors are scanned just let the whole beam could cover the clear aperture area of the objective mirror.

80 by 80 simulations were completed and the simulation data was combined to obtain the final image in figure (c). Visually, it looks not as favorable as the angular system, but agrees very well with the previous quasioptical simulation. As the quasioptical simulation has already been verified with experiment data in the group’s previous work, we believe the ASAP simulation is also credible.

Next, we took the surf plot of the simulation results for the two systems and viewed them from different angles, plotted them out as in Figure 50. As the images show, we have much better image quality obtained from the angular scanning system than that from the rectilinear system. The image of the sphere target ball has more homogenous coupling efficiency and much less ripples (theory inherited noise), thus better signal to noise ratio.

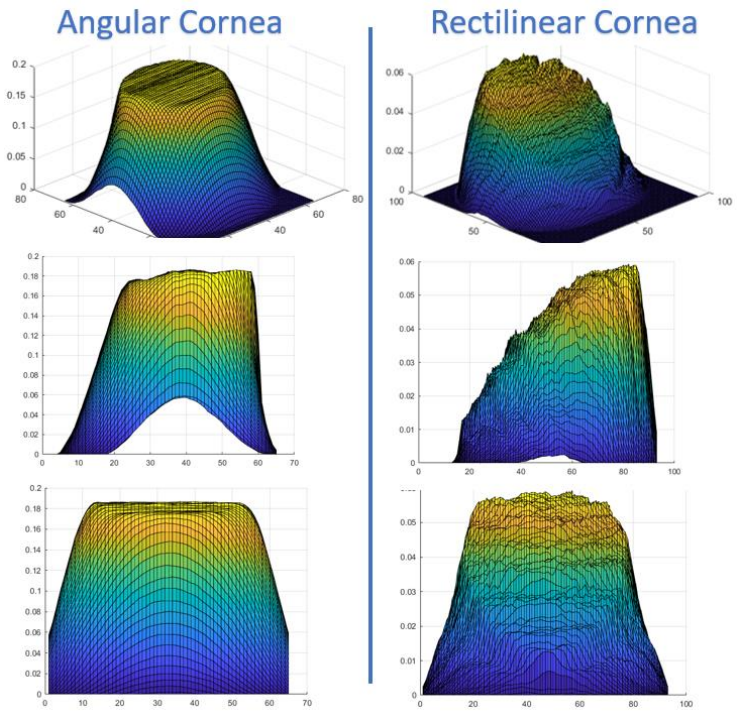

Figure 50. Surf plots comparison between angular scanning and rectilinear scanning systems.

5.5 Speed Estimation from Mechanical Point of View

Let alone the better imaging quality, we should never forget this angular system is designed for much faster scanning speed. Considering the current technology available, like galvometric or resonance mirrors, the complete scan could be done within microseconds. Video rate scanning could be easily achieved and the mechanical motion will never again be the limit for top of our corneal scanning system. It is likely the future speed limitation will shift to electronic side, like how fast your acquisition is and how fast your modulation of source could be, etc..

CHAPTER 6: **SYSTEM ANALYSIS**

A crucial concern we had for the system design is that ray tracing in ASAP might not be able to reflect all the design details and not enough for system characterization. We think it is necessary to have other approaches to verify the correctness of the design and give us more quantitative details about the system.

6.1 Quasioptical Analysis

Quaisioptical analysis approach was first investigated here. To simplify the process, we picked out one most important part out of the optical train for our analysis, as the THz waves starting from the rotating mirror to the two big objective OAPS, to the target, and then back to the rotating mirror through the OAPS.

As we can see that, the OAPs are orders bigger than the scale of THz wave cross-section. Whenever the THz beams interact with the OAP mirror, it only interacts with a small area of the surface of the mirror. Given a reasonable spreading angle to the spreading beam starting from the rotating mirror, the interacting segment only spans moderate changes in curvature and focal length. In the near edge end, the focal length is short, hence the cross profile that being reflected by the OAP is also small compared to the far edge. For the far edge end, even though the focal length is longer than that at the near edge, the asymmetricity induced here can be made up for flatter surface at the far edge. For the observations above, we are confident to use a thin lens whose focal length is equal to the central beam path length from the mirror surface to the focus. To take one step further, we can simplify this part of optical system into a thin lens optical train.

6.1.1 Problem Setup

The quasioptical setup and problem definition for the angularly scanned system are based on the thin-lens-optical-train simplification, as displayed in Figure 51 (a) and (b) respectively. The mirror front surface centroid is coincident with the focal point of OAP 1 and the cornea center of

curvature (CoC) is coincident with the focal point of OAP 2. The beam angle theta is defined with respect to the z-axis (standard spherical coordinates).

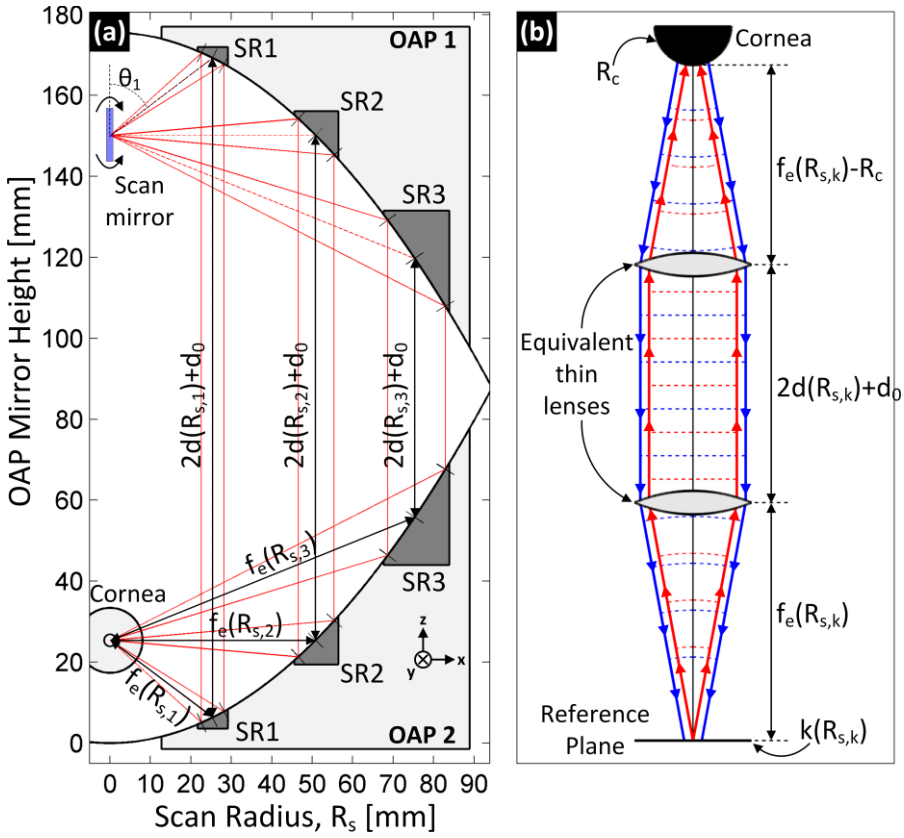

Figure 51. Ray path diagram of the double mirror, angular scanning system.
(a) Parabolic mirror segmentation and (b) thin lens equivalent of the overall beam path.

In Figure 51 (a), the beams are diverging from the scanning mirror at a half angle of 5°. The beam centroids deflected towards sub-reflectors 1, 2 and 3 (SR1, SR2, and SR3) form angles of 125°, 90°, and 63°, respectively with the vertical axis. These beams result in collimated beam diameters (in the limit of geometric optics) of 5.54 mm, 8.89 mm, and 14.25 mm. The equivalent quasioptical thin lens problem is displayed in Figure 51 (b) and the representative ABCD matrices are given in equations below:

$$R_S = 2f_p/(1+\cos\theta) \tag{17}$$

$$M_{P\to C} = \begin{bmatrix} R_C f_e^{-1} & f_e - R_C \\ f_e^{-1} & 1 \end{bmatrix} \begin{bmatrix} 1 & 2d + d_0 \\ 0 & 1 \end{bmatrix} \begin{bmatrix} 1 & f_e \\ -f_e^{-1} & 0 \end{bmatrix} \tag{18}$$

$$M_{C\to P} = \begin{bmatrix} 0 & f_e \\ -f_e^{-1} & 1 \end{bmatrix} \begin{bmatrix} 1 & 2d + d_0 \\ 0 & 1 \end{bmatrix} \begin{bmatrix} 1 & f_e - R_C \\ -f_e^{-1} & R_C f_e^{-1} \end{bmatrix} \tag{19}$$

$$M_C = \begin{bmatrix} 1 & 0 \\ 2 * R_C^{-1} & 1 \end{bmatrix} \tag{20}$$

The centroid of the reference, angularly scanned plane is located at the focal point of OAP1. The beam travels a free space path length of $f_e(R_s)$, is collimated by a thin lens of $f_e(R_s)$, travels a free space path length of $2d(R_s)$ + d_0 where d_0 is the tip-to-tip separation of the two OAPs, is focused by a thin lens of focal length $f_e(R_s)$, and then travels $f_e(R_s)$ – R_c to the corneal surface. This path is described in Equation (18) and the reverse is described in Equation (19). The complete path is $M_{C\to P} M_C M_{P\to C}$ where M_C is defined in equation (20) and the angularly dependent scan radius is given in equation (17).

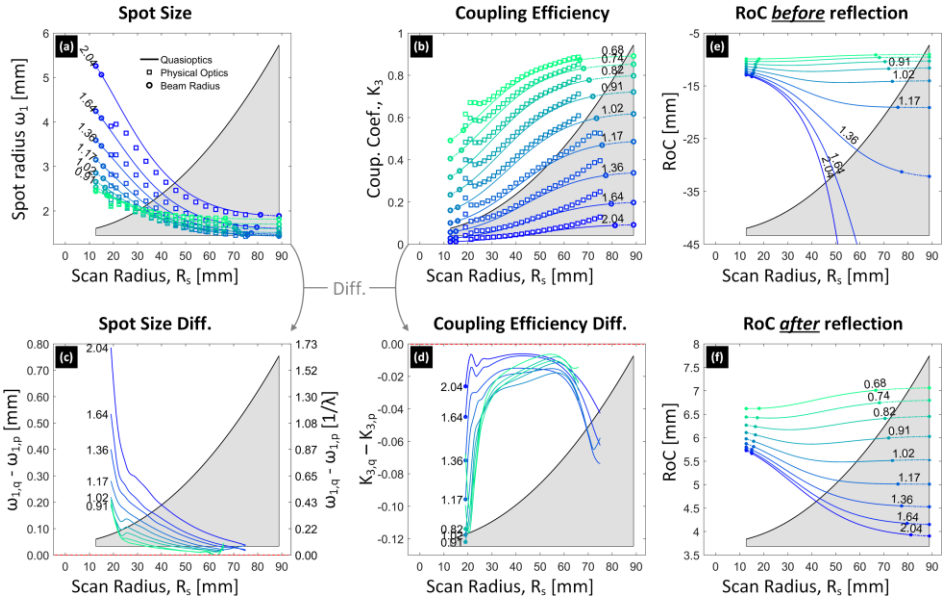

Figure 52. Quasioptical and physical optics analysis results.

Angular scanning system focused spot radius as a function of the input beam and radius (ω0). A scaled overlay of parabolic cross section is shown depicting the location of the collimated beam centroid. (a) Radius of spot size of the THz beam has on the target sphere as a function of input beam radius and scan radius. (b) Angular scanning system coupling coefficient between the input and output beam as a function of input beam centroid location. (c) Differential. (d) Differential. Radius of curvature of the focused beam immediately prior to the target surface (e) and immediately following reflection from the target surface (f).

6.1.2 Quasioptical Computation: Spot Size

The spot size computations as a function of radially dependent scanning position and spot size at the scanning mirror plane are shown in Figure 52 (a). To enable comparisons between these results and those in our previous work, the computed parameters are displayed as a function of collimated beam centroid location following collimation by OAP1. Additionally, the considered focused beam radii (ω_{02}) were the collimated beam radii utilized in the rectilinear scanning simulations, integer 4…12 mm [48], focused by a 76.2 mm CA, 38.1 mm parent focal length mirror. These were computed with the thin lens approximation and ABCD matrices ((21))

$$\omega_{0,2} = \frac{2\lambda^2 \omega_{0,1} f_p \left(4f_p^2 + 1\right)^{\frac{1}{2}}}{4\lambda^2 f_p^2 + \omega_{0,1}^4 \pi^2}, \qquad \omega_{0,1} = 4 \ldots 12 \tag{21}$$

Unlike the rectilinear system the angularly scanned system displays monotonically decreasing spot size for increased scan radius for all the considered input beam radii. Further, as the input spot size becomes smaller, the overall slope of the spot size curve drops and the spot size on target becomes nearly invariant to the scan mirror position. The net result is uniform spatial resolution as the input transverse extent is shrunk down to a point source.

Predictably, the largest computed field radius (ω_1 = 5.1 mm) was obtained with the largest input beam radius ($\omega_{0,2}$ = 2.04 mm) and smallest collimated beam location (R_s = 12 mm) corresponding to a beam path with the longest collimated section and the shortest Rayleigh range within the collimated path. However, the smallest focused field radius (ω_1 = 1.5 mm) was obtained with an input field radius of 1.02 mm at a collimated beam location of 75 mm. This input pair does not leverage the smallest input spot size nor the shortest EFL OAP segment and is another demonstration of competing factors that arise from not intercepting the beam at the focal point of the focusing optic. This concept is further evidenced by the varying crossover points between the larger and smaller spot size diameters. However, the effect is greatly reduced as compared to the rectilinear scanning system and inspection of Figure 52 (a) suggests that minimizing the input

beam radius results in the optimal input beam size. The tradeoff is a small increase in minimum focused beam waist, 1.75 mm vs 1.5 mm for the 1.02 mm and 0.68 mm input beams respectively, for a significant decrease in focused waist variation. This yields range of [1.5 mm, 2.5 mm] for the 0.68 mm beam and [3.25 mm, 1.5 mm] for the 1.02 mm beam.

6.1.3 Quasioptical Computation: Coupling Coefficient

The beam coupling coefficients for the two-mirror scanning system were computed with equations where the reference plane was defined as the scanning mirror plane. The results Figure 52 (b) are all monotonically *increasing* as a function of mirror radius, R_s, which is in contrast to the rectilinear case where every curve is monotonically *decreasing*[48]. This is due primarily to the collimated beam parameters of the mirror where larger R_s corresponds to increased collimated beam diameter and decreased collimated beam path length (Figure 51 (a)). A peak coupling efficiency of 0.9 is achieved with an input radius of $\omega_{0,2}$ = 0.68 mm and a scan radius of 88.9 mm.

6.1.4 Quasioptical Computation: Radius of Curvature

The radii of curvature of the beam immediately prior and following reflection from the cornea are displayed in Figure 52 (e) and (f) respectively. The 2.04 mm curve rapidly approaches -∞ for increasing R_s and confirms that the beam waist goes from inside the cornea to outside the cornea. However, all other curves remain finite, and negative, for the entire scan range (R_s) indicating a beam waist inside the cornea. Additionally, as the beam gets smaller, the radius of curvature plot converges to a flat curve that is effectively invariant to mirror position. For example, 0.68 mm and 0.74 mm radius beams produce a radius of curvature, immediately prior to the cornea, of -9.5 ± 0.3 mm and -10 ± 0.3 mm respectively confirming that the variable beam diameter system produces geometric optics like performance at small input beam diameters (e.g. point source)

The output beam radius of curvature in Figure 52 (e) is consistent with what is expected from the radius matching. The radii of curvature of the small input beam diameters are largely unperturbed. In contrast, the largest beam diameters with beam waists that traverse the corneal

surface behave the same as those in the rectilinear scan system[48].

It is interesting to note that, for example, the 0.68 mm, 0.74 mm, and 0.82 mm input beam radii produce pre-corneal reflection radii of curvature that differ, at max, ~ 1.5 mm from each other for an R_s yet their coupling coefficients differ by more than 20%. The denominator of equation includes ratios of input and output beam radii and input and output radii of curvature. These parameters did not change significantly between the cornea and OAP, nor did they vary much in the collimated section of a beam path. However, they can change rapidly over short distances around the reference plane. These issues suggest that the angular scanning system may be more difficult to couple to a transceiver system and/or more sensitive to misalignment; an issue that was explored in a later section.

6.2 Physical Optics Analysis

6.2.1 Physical Optics: Spot Size

Physical optics analysis was applied to the 2-mirror scanning system and two specific configurations are demonstrated in Figure 53: small input beam waist paired with a large scan radius (Figure 53(a)) and large input beam waist paired with a small scan radius (Figure 53(f)). These configurations resulted respectively in a large scan radius paired with a larger scan diameter and a small scan radius paired with smaller beam diameter.

The larger beam diameter and reduced reflector asymmetry about the beam centroid represented by the configuration in Figure 53(a) results in a focused beam with limited Gaussian mode content both in the x'-z' and y'-z' plane with good radial symmetry and a beam waist approximately coincident with the cornea CoC/OAP focal point. The configuration in Figure 53(f) resulted in substantial beam diffraction and significant beam asymmetry as a result of the short Rayleigh length of the collimated beam following reflection from the initial OAP.

The physical optics results are superimposed with a square marker (□) in Figure 52(a) and the differentials represented in Figure 52 (c). One immediate difference from the rectilinear

scanning system is the physical optics analysis predict 1/e field radii smaller than that computed with quasioptics for any input pair. The analysis also indicates that the two analysis methods converge as the input beam radius decreases. The maximum deviation between quasioptical and physical optics computations is 0.8 mm and occurs with an input beam radius of 2.04 mm at a scan radius R_s = 19 mm. This set of parameters produced significant diffraction as evidenced by Figure 53(f)-(j).

6.2.2 Physical Optics: Coupling Efficiency

The reflected beam magnitude and phase at the reference plane is displayed in Figure 53 (d)-(e) and Figure 53 (i)-(j). Quasioptical analysis predicts high coupling efficiency for the configuration in Figure 53 (a) and this is confirmed with a high radial asymmetry in the magnitude and the relative uniformity of the phase across the majority of the beam. Similarly, the configuration in Figure 53 (f) to result in poor coupling between input and output beams and this prediction is supported by the beam asymmetry, multiple beam extrema, and substantial field curvature indicated by the phase plot.

The physical optics results are superimposed with a square marker (□) in Figure 52 (b) and the differentials represented in Figure 52 (d). Similar to the beam radius results, physical optics predicts a coupling efficiency that is higher than the quasioptics analysis for any input beam radius and angle. The comparison also exhibits peak agreement between quasioptics and physical optics in the center of the mirror and diverging predicted coupling at the edges of the mirror with the largest discrepancies occurring at the near edge. These beam paths feature the longest collimated beam path lengths in the system paired with the maximum mirror asymmetry about the beam centroid. The magnitude of discrepancies between the two beam propagation techniques at these paths indicate the increased effects of beam asymmetry and diffraction on the performance of the angular scanning system as compared to the rectilinear scanning system[48].

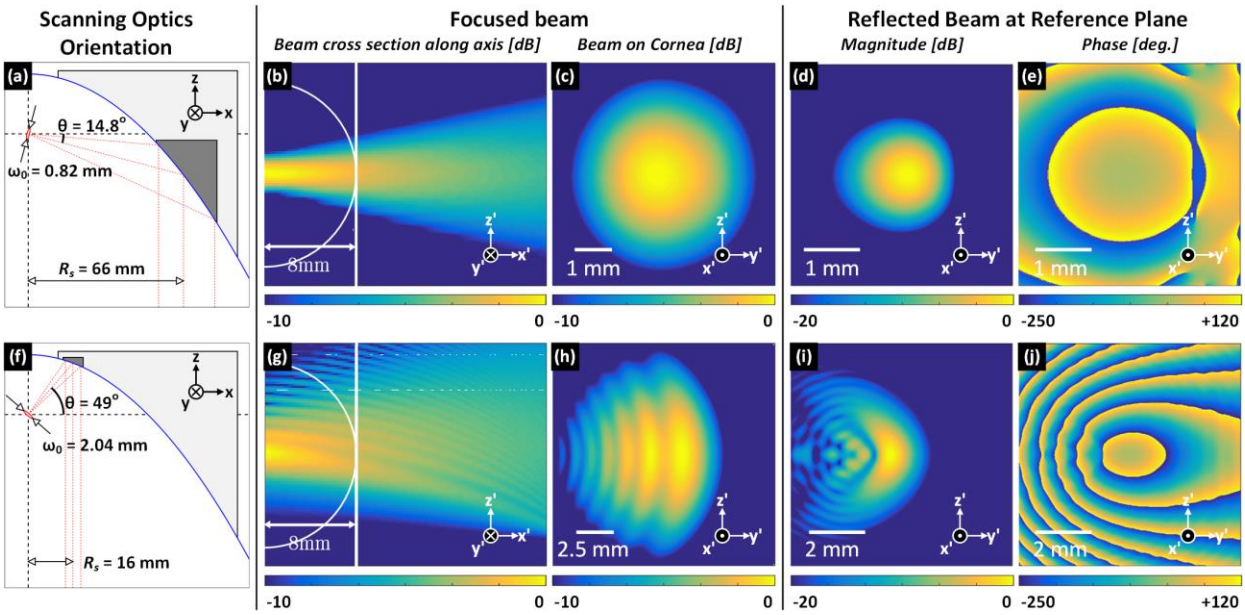

Figure 53. Physical optics simulation results.

(a) Layout for θ = -14.8º (R = 76.9 mm) and ω_0 = 0.82 mm. (b) cross section of beam in the x'-z' plane. section (c) beam profile on the y'-z' plane tangent to the cornea and coincident with the intersection of the focused beam centroid and corneal surface. Electric field magnitude (d) and phase (e) of the beam at the reference plane (x-y plane) following reflection from the cornea and recollimation from the OAP. (f) Layout for θ = +49.0º (R = 76.9 mm) and ω_0 = 2.04 mm. (g)-(j) same as (b)-(e). Note that in configuration (a) the fields are nearly Gaussian while in configuration (f) they are not due to the offset reflector configuration and possible diffraction

6.3 Gaussian beam propagation

As we discussed previously, OAP segments could be treated as thin lenses. Here we treat the whole system as a train of thin lenses and mirrors. As we know, Gaussian beams, like the THz source in our case, transform in an unorthodox manner. People usually use matrix transformations to solve the problem, but Self was able to develop a less rigorous but more insightful approach to this problem [85]. Under paraxial condition, by calculating the Rayleigh range and beam waist location following each individual optical element, the transformations of a Gaussian beam through simple optics could be modeled. The location of the beam waist is calculated with equation (22), where s is the object distance, s" is the image distance, f is the focal length of the lens and z_R as the Rayleigh length.

$$\frac{1}{s + z_R^2/(s-f)} + \frac{1}{s"} = \frac{1}{f} \tag{22}$$

The magnification is given by equation (15), where w_0" is the waist of image beam, and the w_0 as the original beam waist.

$$\mathrm{m} = \frac{w_0"}{w_0} = \frac{1}{\sqrt{(1-\frac{s}{f})^2 + (z_R/f)^2}} \tag{23}$$

New Rayleigh length is calculated in equation (24)

$$z_R" = m^2 z_R \tag{24}$$

In our case, we treated each OAP as thin lens with its own focal length and flat mirror with a thin lens with a focal length of -∞ with intervals as they should be in our system. We simulated the maximum and minimum pathlength scenarios that could be achieved by adjusting the distance between the two big OAPs, the results are shown as it in Figure (a) and (b). As the results shows us the radius of the beam spot on the target are 1.895 and 1.947 mm for the maximum and

minimum distance respectively. And the results agrees with our prediction from quasioptical and physical optics analysis. This method intuitively shows us how the THz beams propagate in the system and how the system parameter affect the imaging quality.

From previous discussion, it shows that ray tracing (either ABCD matrix or ASAP) is sufficient for our THz imaging system design and optimization.

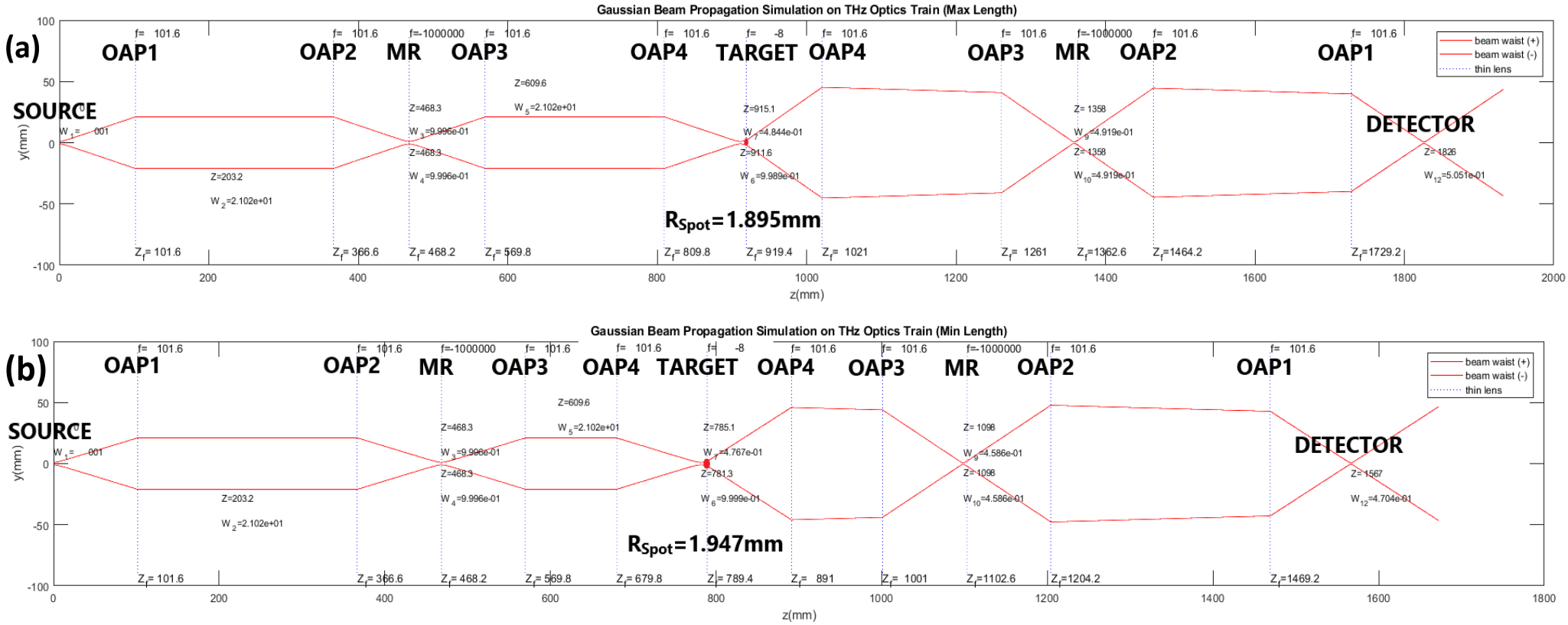

Figure 54. Gaussian beam propagation for complete system simulation

6.4 Alignment Sensitivity Analysis

Signal sensitivity as a function of target misalignment was explored for the rectilinear and scanning systems with non-sequential ray tracing (ASAP, Breault Inc.). The systems were arranged as shown in Figure 46 and Figure 49, with the optical elements placed at the minimum allowable separation, thus reducing the free space path length for each optics train. A reference reflector with an 8 mm RoC was placed with its CoC coincident with the focal point of the focusing/scanning mirror in each system. The detector was modeled as a circular aperture measuring 2 mm on a side thus mimicking the zero bias Schottky diode package. The source was modeled as a pencil beam with a 2-degree divergence angle corresponding to the 26 dB directivity output of a circular feedhorn. This produced a ~ 10 mm collimated beam radius.

In both systems, the scanning mirrors were positioned such that the centroid of the focused beam was collinear with the optical axis of the reference reflector. Then the rays from the source were traced to the corneal surface, reflected, and traced back to the receiver. The total flux intercepted by the detector aperture in each system was quantified as the reference level of each perfectly aligned system.

The reference reflector position was then displaced transversely in two dimensions in a plane defined by the surface normal to the mirror and corneal optical axes and coincident with the reference reflector apex. The concept is demonstrated pictorially in Figure 54 (a) where the transverse plane is denoted by the axes X’ and Y’. The plane was 1.2 mm x 1.2 mm and discretized into a set of points with 0.2 mm center-to-center separation. At each transverse location, the source rays were retraced through the system and the total flux normalized by the reference flux to ascertain relative reductions in collected signal as a function of decentration.

The results of the simulation for the rectilinear scanning and double angular scanning systems are shown in Figure 54 (b) and (c), respectively, where the axes correspond to the deviation between the reference reflector optical axis and focused beam centroid. The color bar corresponds to the relative collected flux. The angular scanning system demonstrated a

substantial increase in sensitivity to non-optimal alignment as compared to the rectilinear system characterized by a full width half max (FWHM) of 0.4 mm x 0.25 mm and ~ 0.8 mm x 0.8 mm for the angular and rectilinear systems, respectively. The apparent asymmetry in the rectilinear system is due to the overall asymmetry of the system using only one off-axis parabolic (OAP) mirror for the scanning function. This result contrasts with the mirror symmetry along both axes in the angular system because of the matched mirrored configuration of the OAP mirror pair

With consideration of the two-pass path, the rectilinear system beam path interfaces with four (x4) parabolic surfaces, while the angular scanning system interfaces with eight (x8). When an OAP mirror focal point is misaligned with the target surface, the collected beam can be collimated on a path not parallel with the optical axis of the mirror, resulting in a transverse walk-off of the beam after focusing from a subsequent OAP and/or complete beam walk-off in the collimated beam path. Analysis of the traced rays is consistent with this theory.

It was anticipated that the misalignment issues with patients would be caused by involuntary radial movements of the eyes known as Saccades [86] while longitudinal movements would be constrained with the proper chin and head rests. Also, it is important to note that the ray tracing simulation does not take into consideration field and beam pattern matching and therefore serves as both an upper bound on alignment sensitivity. More importantly, a relative analysis between the systems that should give a good indication of expected trends computed with physical optics.

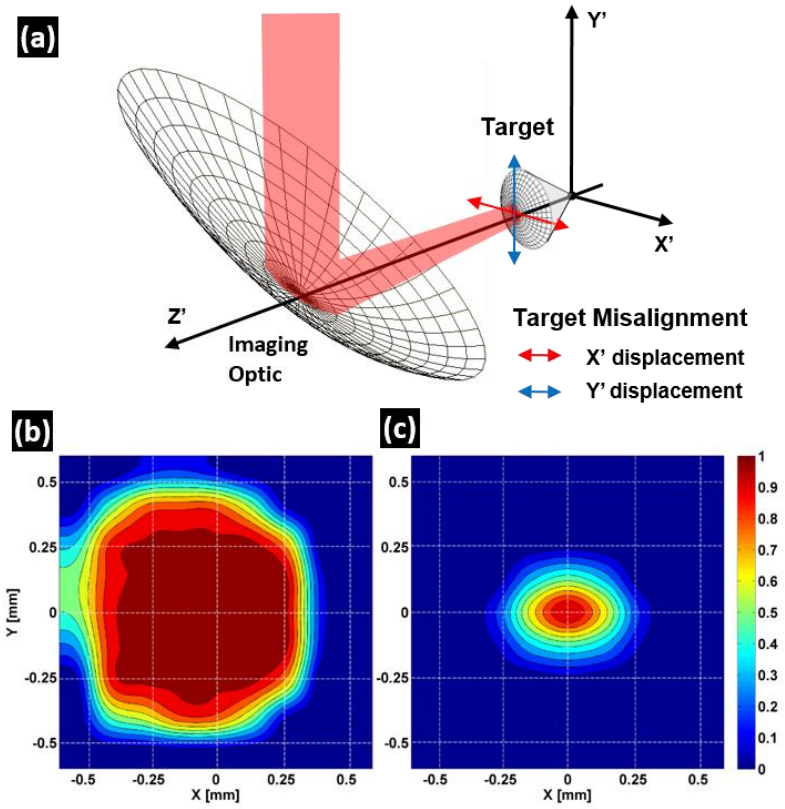

Figure 54. Target alignment sensitivity analysis

(a) The cornea is displaced from the ideal location in the transverse plane (x', y'), simulating decentration of the patient's cornea due to misalignment. An estimate of coupling efficiency was computed by tabulating the fraction of the returning beam cross section collected by a circular detector aperture with 2 mm edges, placed at the "detector" location indicated in the two system designs (b) Collected signal, for the rectilinear scanning system, as a function of corneal apex transverse location. The signal is normalized to the optimal alignment (x = 0, y = 0) position where red corresponds to more signal and blue to less. (c) Same as (b) but for the angular scanning system. The asymmetry apparent in the rectilinear case is due to the overall asymmetry of the system using only one imaging mirror.

CHAPTER 7: SYSTEM INSTRUMENTATION

7.1 System Overview

A prototype system was constructed for our experiments. As shown in the block diagram in Figure 55, it plots general construction logic for the system elements, including the source, detector, mechanical automation, signal modulation and acquisition and data management. Underneath the diagram plot, basic parameters are also summarized here.

In the system, signal from an radio frequency oscillator (RF XO, Micro Lambda Wireless, Inc) is amplified and frequency multiplied by the Amplifier-Multiplier Chain (AMC, Virginia Diode, Virginia) to a tunable 630-680 GHz spectral region as out THz source. The source has an ouptput power of around 0.8 mW with output bem directivity of 26dB at 12.5 degrees. The source could be frequency and amplitude modulated at the same time A zero-bias Schottky diode (ZBD, Virginia Diode, Virginia) with detection bandwidth of 500 – 700 GHz works as the signal detector. The detector also has a directional gain around 26 dB. The combination of high responsivity over 1000V/W and low noise equivalent power (NEP) of ~ 4 $\mathrm{pW}/\sqrt{Hz}$, allows it for relatively accurate measurement with low noise level. Both the source and detector are coupled to a diagonal feedhorn antennas with 26 dB of gain and aperture dimensions of 2.4 mm by 2.4 mm.

Because of the coherence nature of the THz source and the specularity of the target, or the cornea here, THz waves could form obvious standing waves across the whole optical train from the source to the optical elements (OAPs, mirrors and target) to the detector. Signal variations by optical pathlength induced standing waves could be a significant confounder for our signal measurement, so the output was frequency modulated to provide a frequency bandwidth that covers the expected full etalon period of the optical path so as to minimize the standing wave effect. The source is also amplitude modulated with an TTL signal from a Lock-in Amplifier (LIA, RS830, Stanford Research System, VA) at 1 kHz, the rectified signal from the ZBD is fed back to

the LIA and demodulated, filtered with a constant time of 3 ms.

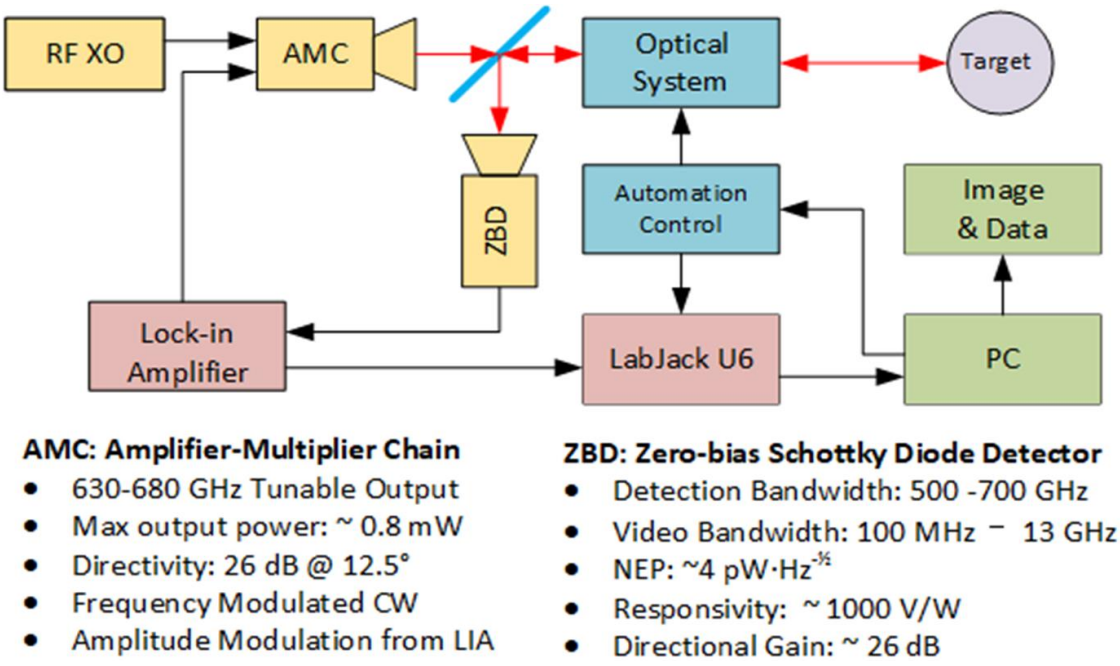

Figure 55. Block diagram of prototype system for THz imaging

A Graphic User Interface (GUI) was developed and installed for the general control and coordination for the system. As shown in the system diagram, the personal computer (PC) where the GUI is installed, connects to the LabJack U6 (LabJack, CO) which reads data from the LIA and location flags from the motors, to the automation control center which actuate the scanning movements of the optical system and also is responsible for data manipulation, storage and real time image display.

7.2 THz source and Detector Setup

7.2.1 Source Setup

A chained combination of permanent magnet YIG-tuned oscillator (Model NO.: MLPM-1498BF) and a AMC works as the THz source for our system. For the oscillator, its free running frequency range is 13.13-14.2 GHz. With a frequency control voltage from 0-10 V, the output frequency could be adjusted through out the free running frequency range. In our system, the voltage is tuned to be 4.7 V and generates an output RF signal centered at 13.55 GHz. A frequency modulation signal is applied the oscillator at a rate of 100 KHz. The amplitude of the modulation signal is at its allowed maximum value, 10 V, generating a frequency modulated range of 25 MHz. LIA is generating a TTL signal at 1 kHz for the amplitude modulation, 5V for full attenuation and 0V for full power output. All the powers are connected as in the Figure 56 (a). Figure (b) are the power setup image in the lab.

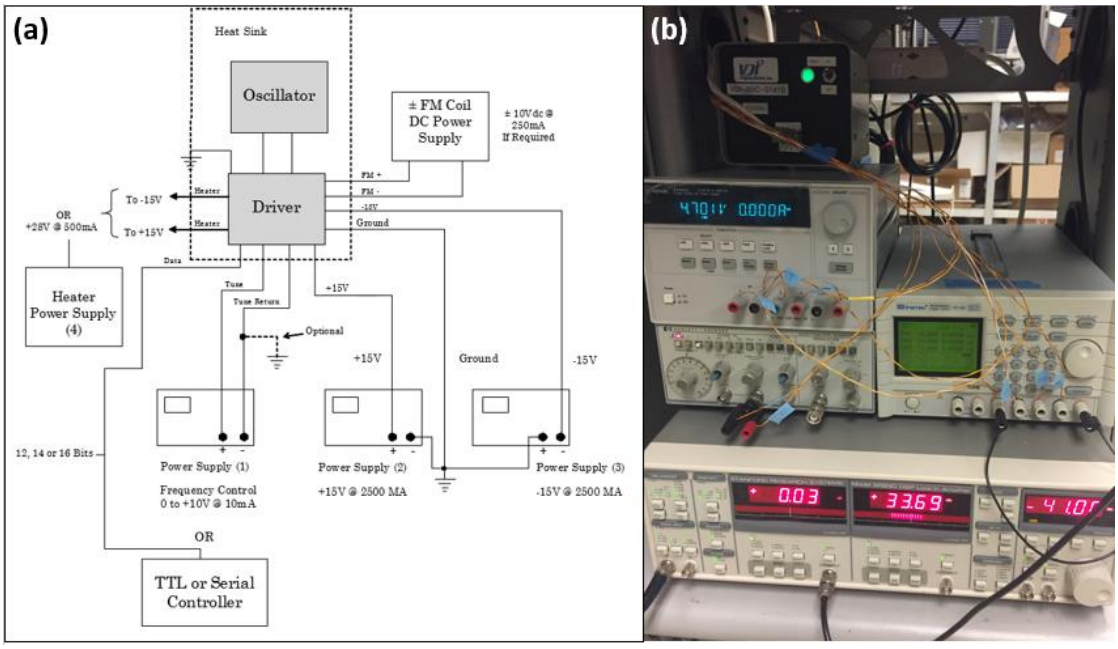

Figure 56. Power supply diagram and real system setup for the oscillator with driver.
(a) Diagram for power hook-up; (b) Real setup for the system.

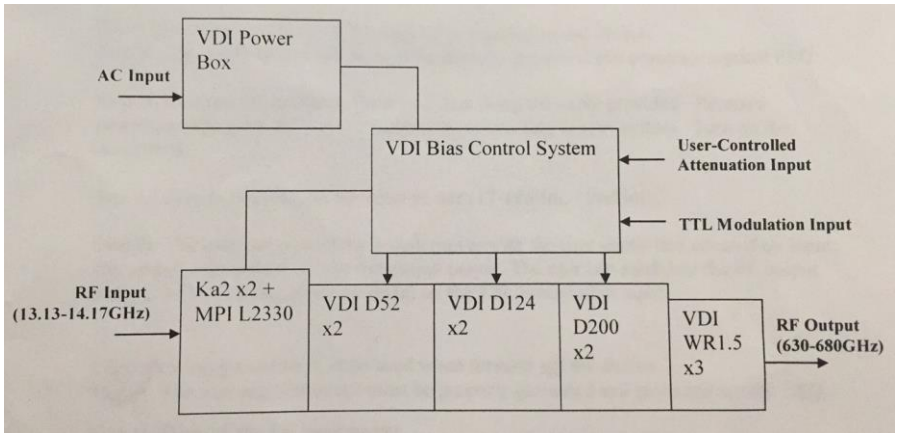

Figure 57. Inner diagram of the amplifier multiplier chain.

As shown in Figure 57, RF input from the oscillator undergoes 5 stages of frequency multiplier and gets a total of 48 times frequency increase. That is to say, we will get a RF signal output at the frequency of 650 GHz and a frequency modulation of 1.2 GHz at the rate of 100 kHz, given our previous oscillator setup. A diagonal feedhorn antennas with 26 dB of gain and aperture dimensions of 2.4 mm by 2.4 mm is coupled to the output of the AMC and generates the THz waves needed for the experiment.

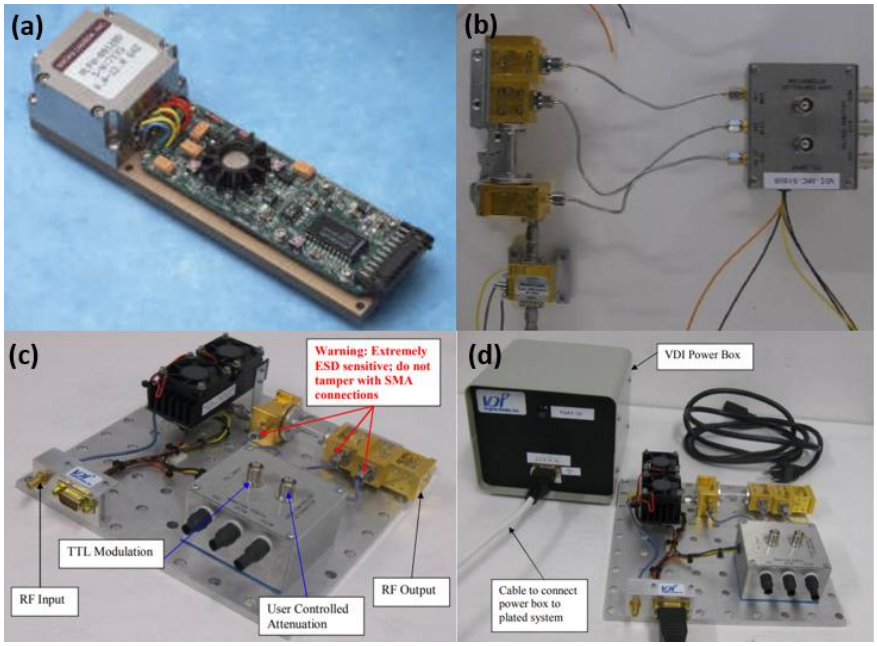

Figure 58. Photos of subparts of THz source.

(a) Permanent magnet YIG-tuned oscillator with analog and FM driver; (b) Amplifier-multiplier chain with modulating module;(c) AMC mounted on board; (d) AMC board and VDI power box.

These products, as shown in Figure 58, are extremely sensitive to Electrostatic discharge (ESD), strict handling procedure must be followed while turning on and off the equipment. Usually, the user is required to properly ground the working bench and user self before any handling of equipment. After hooking up the source subsystem as indicated previously, we can turn on the power box and slowly increase the output power of the oscillator to around 17 dBm (keep smaller than 20 dBm). For the first time, this should be measured accordingly, but can be set and ready for use in the future. Then we can turn on the FM and AM modulation signal and the source should be ready for testing. When turning off the source, we just follow an opposite order.

7.2.2 Detector

The model number of the detector used in our system is WR1.5ZBD and has a relatively flat responsivity of around 1700 v/W curve over our interested band, ~650 GHz, as shown in Figure 59 [87]. Again, a diagonal feedhorn antennas with 26 dB of gain and aperture dimensions of 2.4 mm by 2.4 mm is coupled to the detector. This is also ESD sensitive element and proper grounding should be made for any handling. The signal from the ZBD is directly ready to be fed into the LIA for further processing.

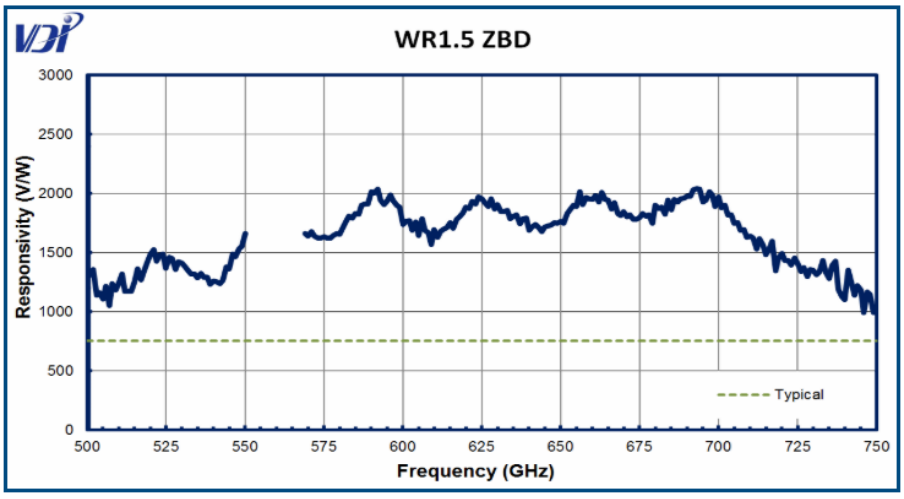

Figure 59. Responsivity curve of WR1.5ZBD.

7.3 Mechanical Design of the System

7.3.1 Overview Design

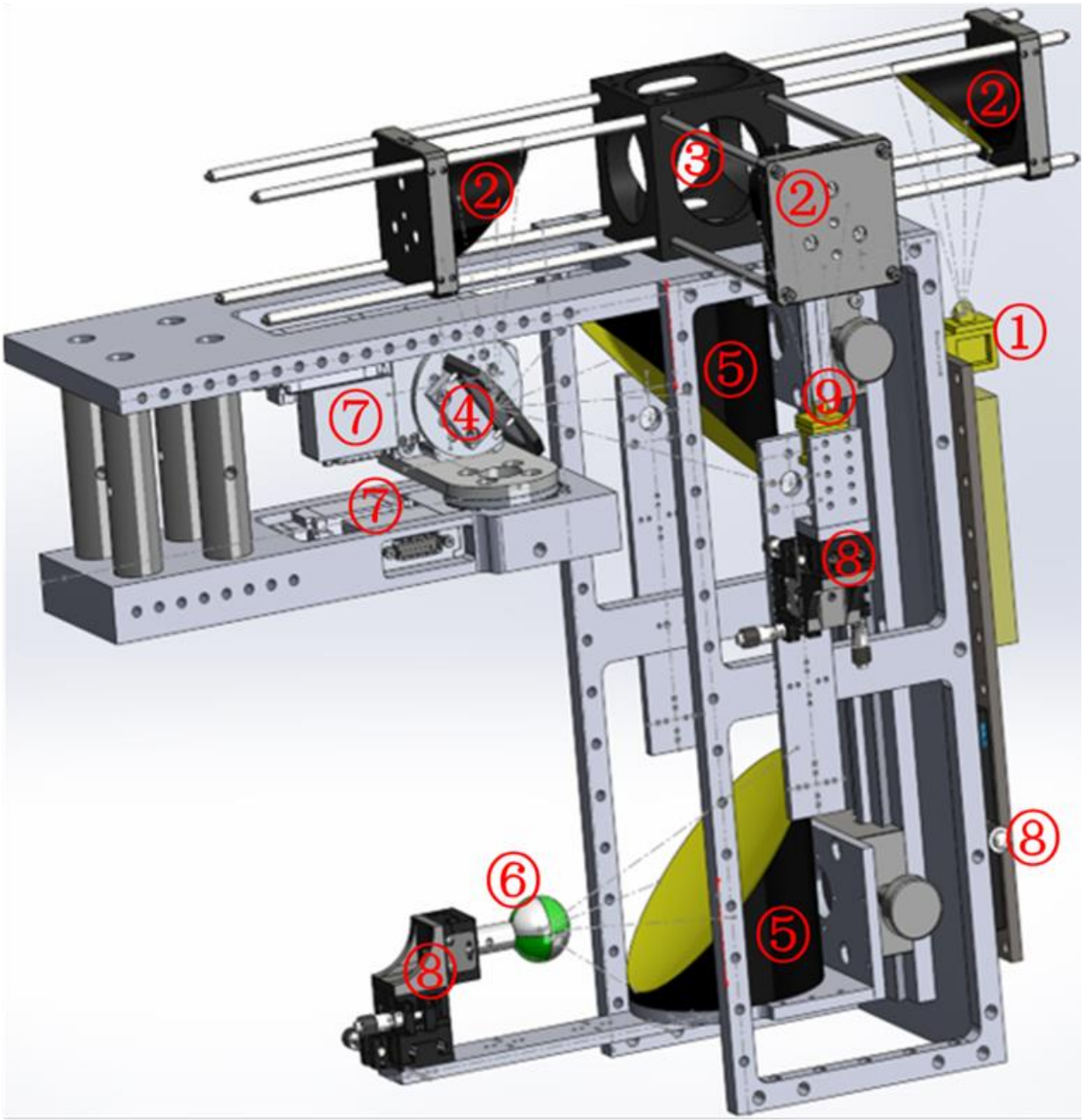

Figure 60. SolidWorks model of the optical system.

① THz Source, ② 2-4-inch OAP, ③ beam splitter, ④ scanning mirror, ⑤ 4-4-inch OAP, ⑥ target ball, ⑦ rotary step motor, ⑧ 3-axis translational stage, ⑨ detector.

As shown in Figure 60, a SolidWorks model was created for the machining of our prototype

system. The mechanical design strictly followed our optical design discussed in the optics design chapter, including the parameters of elements. As we can see in the figure, there are 9 different types of elements that consist the core parts of the system. The main function of the design is to hold these core elements in position accurately and allow for necessary movements for some certain parts, for example, the rotation of rotary motors, sliding of objective mirror and target, and precise minor adjustment for the alignment of source, detector and target.

In order to achieve best functioning outcome, we must guarantee the precision of overall assembly of all the components, thus machining precision of each component and the relative location are the key. On the other hand, we also want to minimize the cost of the system. Maybe it's not 100% necessary in science research, but it is still a good habit to do this when designing a complex mechanical system. In order to meet the two requirements above, we followed three design rules as following. First, use existing parts (commercially available or free in the lab) when possible. Selecting a proper available product as part of your design not only can help meeting the precision required, but also can help you save time and money. Second, ensure alignment accuracy and make it easy for future assembling. This is key to the design and you probably won't want to spend tons of time aligning and assembling the parts. Third, use symmetric design when possible and try to co-use parts (same part for different function). This rule is to help decrease the machining cost, as the unit price usually drops when the quantity of the same components increases. The three rules will be reflected in the detailed design subsections.

7.3.2 Rotating Mirror Assembly



Figure 61. Photo of Rotary motor, RSW60C-E03.

RSW60C-E03, as shown in Figure 61, was selected as the actuator for the scanning mirror. The overall dimension of the motor is 147 mm by 75 mm by 32 mm. It has a max continuous torque of 105 N·m, which is enough for us as we are only actuating the weight of the motor itself and a mirror that can be neglected. The motor has a max speed of 450° /s, which is slower than our best expectation but still acceptable for the prototype. The accuracy is 0.08° , which might cause some miscounting of flags but overall still acceptable, as the speed and accuracy are always a pair of contradictions. That was also the reason we selected this motor as a tradeoff.

Two of these motors were purchased to assemble a two-axis rotary stage to allow the mirror to rotate in both θ and φ directions, as shown in Figure 62. The one on the bottom is the master motor, which moves at least from -30° to +30° , while the top one, slave motor, can rotate freely for 360° . The connectors for the two motors were designed and custom made to ensure accuracy and avoid interference with the system frame.

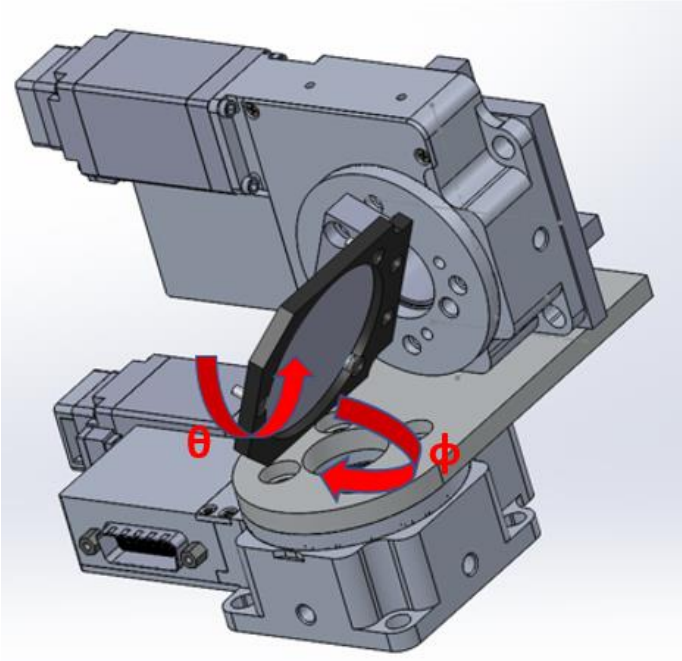

Figure 62. Assembly of 2-axis rotary stage and rotating mirror.

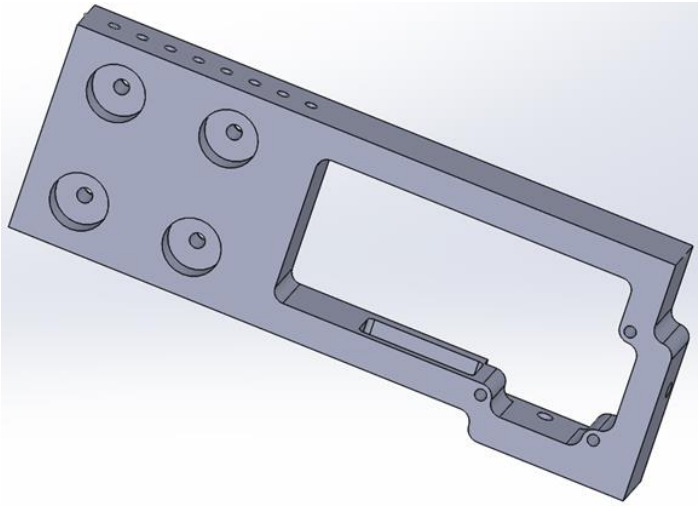

Figure 63. Holding frame for the rotary stage.

As the slave motor has bigger motion freedom than that of the master motor, it is better to use the master motor as the mounting hardware to the entire system. As shown in Figure 63, a holder was designed holder to enable mounting, motion of the stage and holes for communicating cords to come through. In this design, we employed complex curve and position marks to ensure the location precision of the rotary stage, thus of the rotating mirror.

The mirror, rotary stage and the holder are assembled as below. The whole piece is connected to the system frame using four 1-inch posts from Thorlabs.

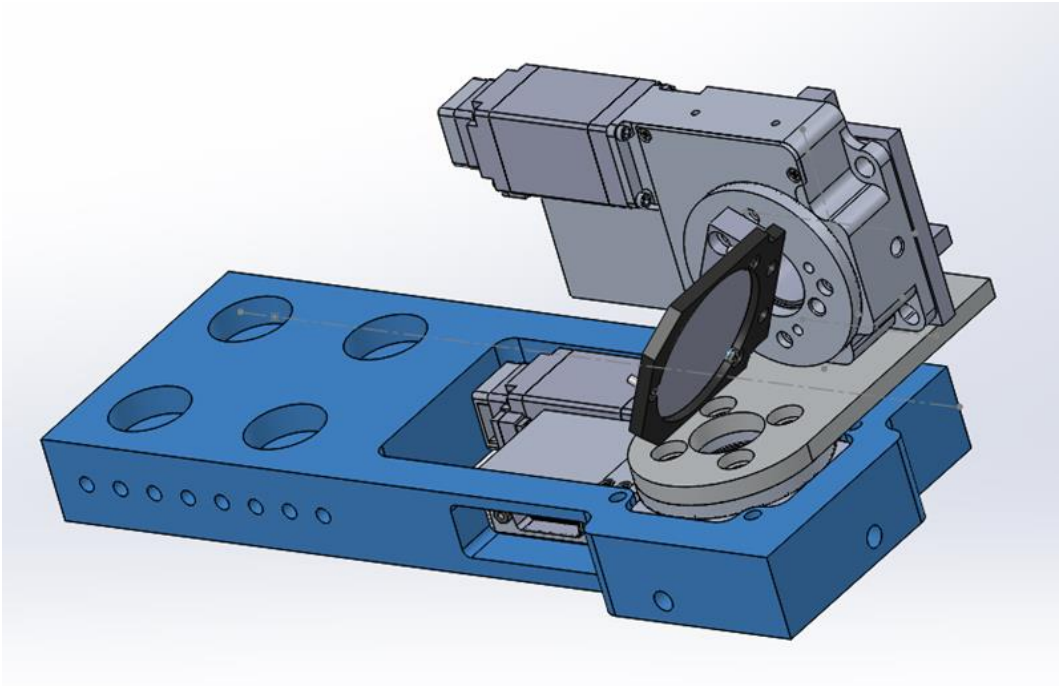

Figure 64. Sub-assembly of mirror, rotary stage and its holder.

7.3.3 Linear Motion

In the design of the system, there are several places we need linear motion elements, like for the positioning of THz source (the AMC board), THz detector (ZBD), the target ball, and the travel distance adjustment for OAPs. Based on different requirements, we have three different solutions to these functions.

For the travel distance adjustment for the big objective OAPs, a long translational stage is adopted here. As in our optics design, we wanted the two OAPs oriented in a compensated “tip-to-tip” manner, that is to say, the relative angle of the two mirrors are fixed and only the relative distance is changeable and a linear translation stage is perfect for this application. The two mirrors are mounted to custom made brackets and then connected to a knob stage with dove slots that just fit to the translation stage. The mirror bracket thickness was carefully calculated so that when

the top mirror touches the frame top plate, the center of the mirror and the rotation center of the scanning mirror will be on the same height for convenient alignment. The distance between the OAPs could be adjusted by moving the other big OAP on the stage. We had a stage with 12 inch free travel distance which allows enough space for the human head in future clinical trials. The target ball and its 3-axis translation stage assembly is connected to the objective mirror with a multifunction bridge, as shown in Figure 65 (a).

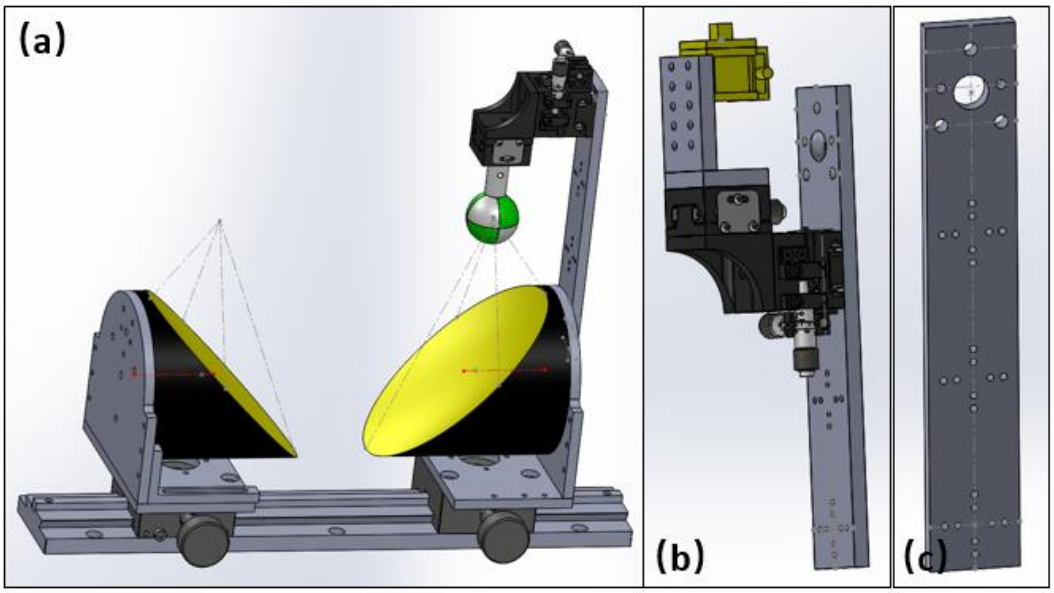

Figure 65. (a) Rack-mirror-target assembly; (b) Detector mounted on multifunction bridge.

Three single-axis stages with actuator screw were assembled to a 3-axis stage to allow a quarter inch movements in all xyz directions for both the detector and target. As we used the same stages in the two scenarios, it is cost saving to co-use the connecting bridge. As in Figure 65 (c), 3 patterns of 3-axis stage mounting holes were put on different location on the bridge for easy swap of applications between target and detector mounting. The bridge used for detector mounting is displayed in Figure 65 (b).

The positioning of small OAPs are through the Thorlabs cubic cage and construction rods, as shown from different angles in Figure 66. In the alignment of OAPs, it is crucial to have the optical axis of different OAPs overlap in the space, and this scheme perfectly solved this problem.

The draw back to this scheme is that there is no clear mark for the positioning for angle and distance of the OAPs. We will talk our solution in our alignment section.

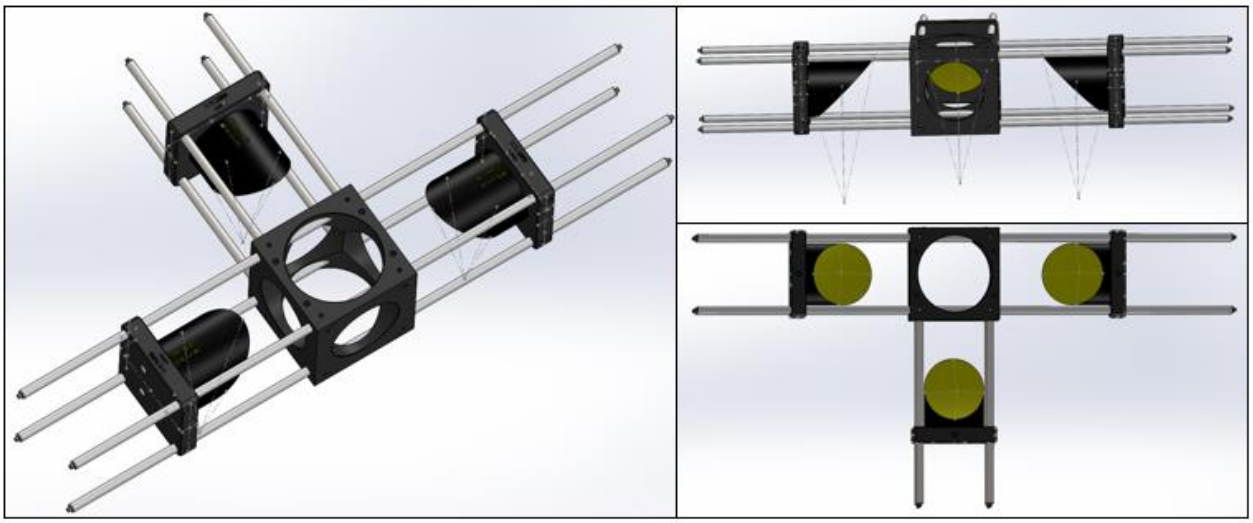

Figure 66. Align focusing OAPs using Thorlabs cubic cage and construction rods

The positioning of source was achieved with the combination of a 2-axis translation stage and the sliding of the collimating OAP. The 2-axis stage is responsible for the location adjustment on the plane parallel to the AMC board and the sliding of the OAPs helps align the source in the other dimension.

In this part, we tried to use as much available parts we can. On one side, this simplified our design work; on the other hand, it also saves money while maintaining the alignment accuracy.

7.3.4 System Assembling and Optical Elements Alignment

Thanks to previous carefully detailed design work, the assembling of the system turned out to be much easier than I anticipated. The system could be assembled in various orders. Sub-assemblies, like Zaber-frame assembly, source-stage assembly, rack-OAPs assembly, cage-mirror assembly, stage/detector-detector-bridge assemblies, and the system frame assembly could all be assembled independently. And it is also easy to put different sub-assemblies to the system fame assembly, for accessing holes have been left at necessary locations.

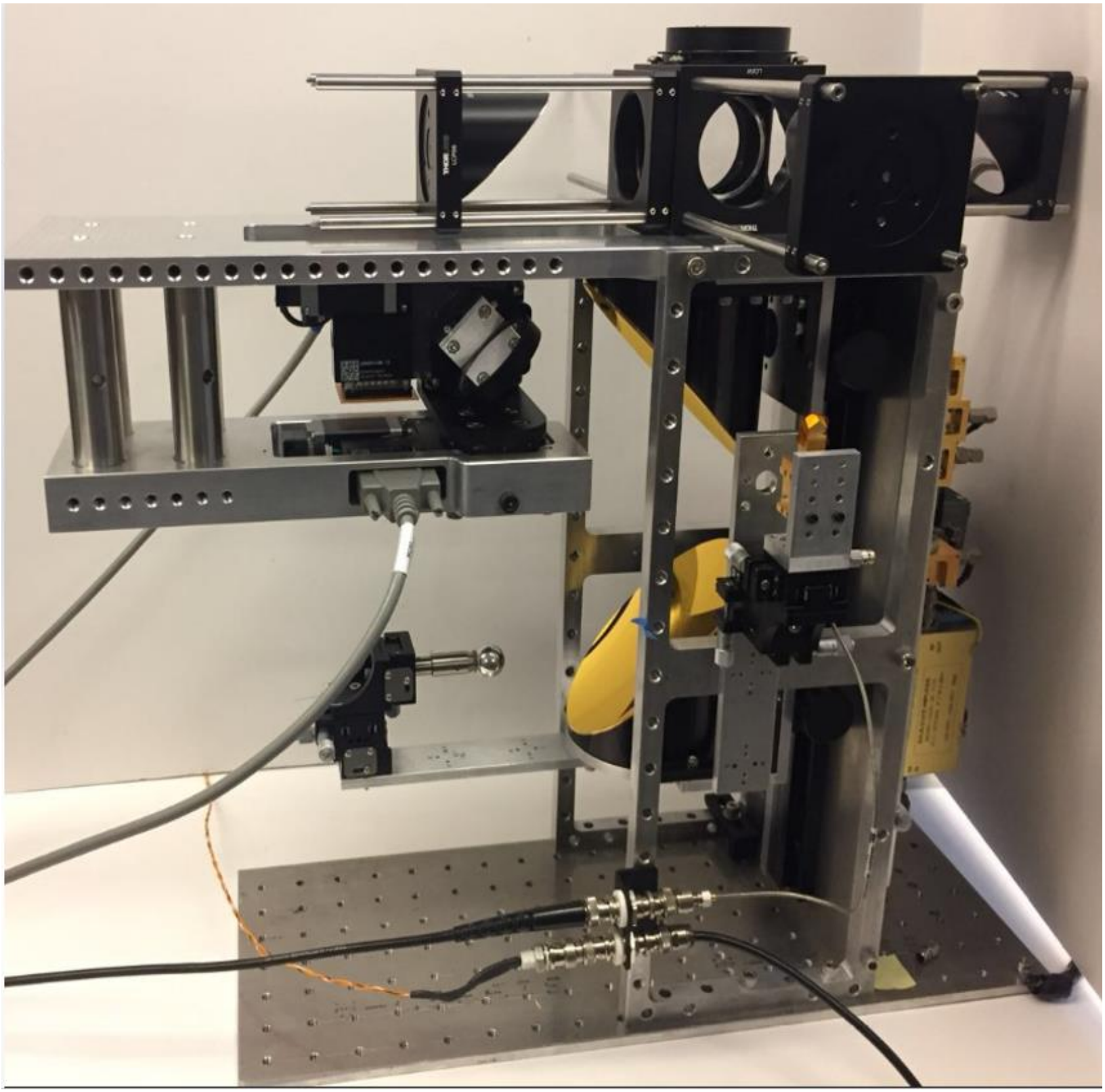

Figure 69. Readily assembled angular scanning THz imaging system.

The mechanical design actually considered for most of the positioning problems in the system, which made the alignment easier. For example, the thickness of the big OAP connecting bracket mentioned previously, will help the center of the OAP and rotating center of the scanning mirror in the same height when the bracket touches the upper plate of the frame. The carefully designed Zaber frame and the accurately placed holes for the posts guarantee the 2 dimension alignment between scanning mirror center and the according focusing OAP focus.

The alignment needed in the system occur where the small OAP slides. A plate that fits to the cage construction rods was modified for mounting of small laser heads that shoots 4 parallel laser beams for the alignment. Before the alignment, the angle of the OAPs were made sure perfectly pointing down. First, align the detector with its focusing OAP. Mount four construction rods on the opposite side of the detector where is empty in the system. Place the laser head plate on the four rods, find the point where the four laser beams overlap in space after the focusing OAP for the detector. Adjusting the focusing OAP and 3-axis translation stage's position and make sure the detector horn aperture overlaps with the converging spot of the laser. Lock the OAP. Second, adjust the beam splitter angle. Take off the OAP above the scanning mirror, move the laser head plate to its position. Rotate the beam splitter until the converging laser point again overlaps with the detector horn aperture. Lock the OAP. Third, align the AMC plate with its focusing OAP. The laser head plate remains above the scanning mirror, find the converging laser point after the source focusing OAP in space. Adjust the 2-axis translation stage underneath the AMC board and slide the above focusing OAP so that the converging laser point overlaps with the source horn aperture. Lock the OAP. Lastly, align focusing OAP to the scanning mirror. Move laser head plate back to the empty rods, and put back the OAP above the scanning mirror. Rotate the scanning mirror to the flat position, and slide the OAP and let the converging laser spot locate at the center of the mirror. Lock the OAP. After these steps, all the OAPs and source, detector should be perfectly aligned and good for testing.

7.4 Rotary Motor Motion Control

The motion control of the scanning mirror is an important part of work while designing the system. A stepper motor controller, X-MCB2, was purchased to drive the 2-axis rotary stages. In this controller, four isolated digital inputs, four isolated digital outputs and four analog inputs are built. An event-driven trigger system allows the device to be programmed for standalone operation based on I/O, time or movement stimuli. Both series of commands and single orders could be sent via serial port.

The motion controlling code made full use of above characteristics of the controller to run a simple but robust scanning pattern. For the top motor, two triggers were set by the movement stimuli. When the top motor rotates every degrees of the axis resolution's value, the motor sent one flag, positive pulse signal, through the digital output; another flag is sent when the motor rotates every round. The second flag is sent to the digital input of the controller. Both of the two flags are sent to two of the digital inputs on LabJack U6. The flag sent to the controller will trigger the bottom motor to move the step of the axis resolution. A digital output from LabJack U6 is connected with another digital input on the X-MCB2. The schematic of the connection board created for the connection between LabJack and X-MCB2 is shown in Figure 68.

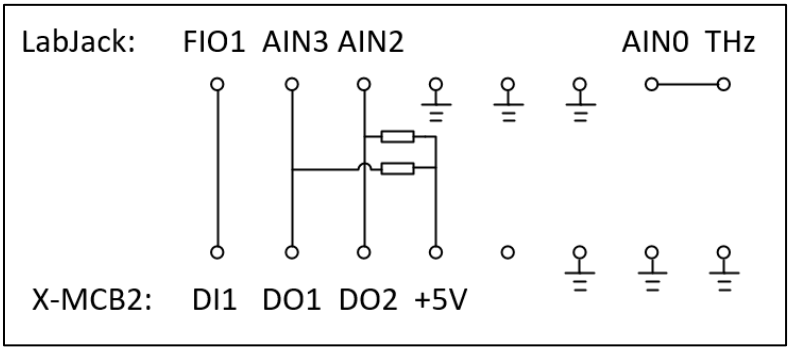

Figure 68. Connection schematic for LabJack Figure 68and X-MCB2.

When the GUI sends an order to the LabJack U6, U6 gives an positive pulse to DI1 on X-MCB2, which triggers the initializing of scanning. In the initializing process, the bottom motor

moves to -30 degree position, and then top motor move rotations of 60/resolution. While the top motor rotating, the two flags will be triggered. And in turn, the second flags will trigger the bottom motor move one step to the positive direction until top motor finishes all the rotations. And then the bottom motor will be in the positive 30 degree position. After the completion of the scanning process, the motors will return to their default positions, reflecting the THz beam to the center of the top big OAP. The two flags by the top motor are sent to LabJack AIN2 and AIN3 for further data management in the GUI in the following section.

7.5 Graphic User Interface (GUI) Design

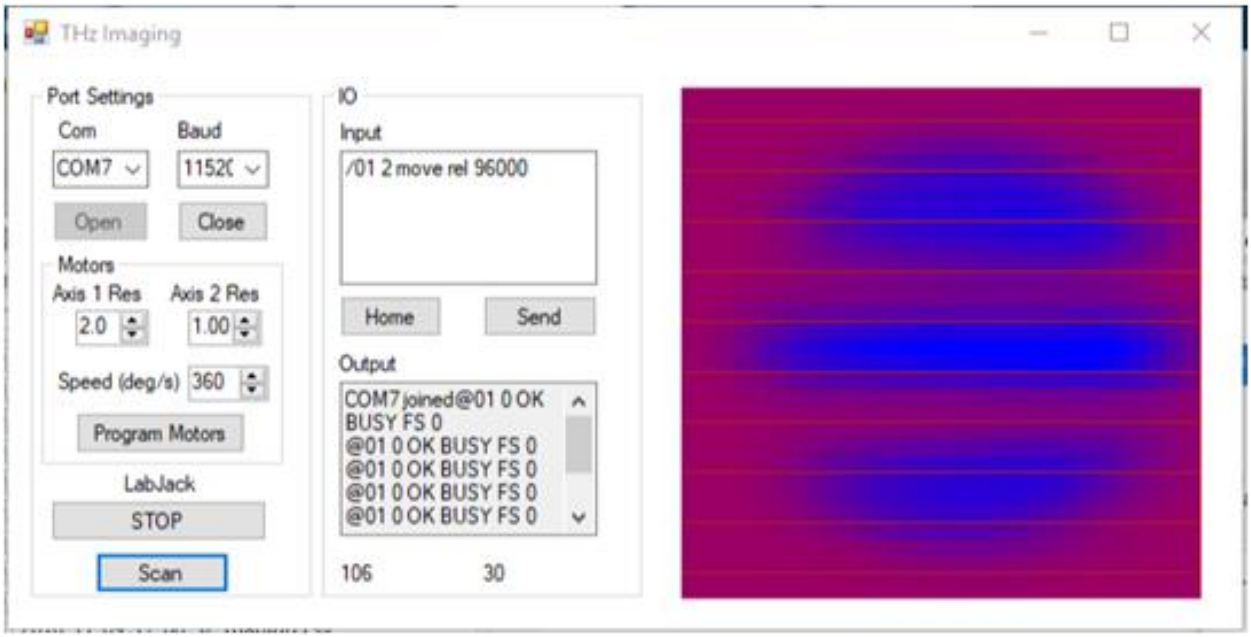

Figure 69. GUI for the angular scanning THz imaging system

A graphic user interface was developed for the angular scanning THz imaging system. The three main functions of the GUI are communicating with the user, motion control and data management.

The GUI communicate with motor controller via serial port. In the GUI, user can search for available COM ports and baud rate to connect with the controller. The user can setup the system scanning parameters, for example the scanning resolutions for both axis and scanning speed of

the motor. By clicking the “Program Motor” bottom, previously talked motor motion logic with the set parameter in the GUI will be coded to the controller and ready for use whenever needed. You only need to re write the code to the motor controller when you need to change parameters. LabJack is also connected to the PC via serial port and can be detected and connected automatically by clicking the connect button for LabJack. When the LabJack is connected, you can start the scanning by clicking the “Scan” button anytime. The trigger signal is sent from FIO1 on U6 to DI1 on X-MCB2 to trigger the motion pattern coded previously.

The LabJack U6 continuously reads the THz data from the output of LIA on the AIN0, and status of the two flags on AIN2 and AIN3 while the system scanning. Once the scanning starts, the three channels of complete raw data will be stored in three columns in a file called the original data file. As the flags’ status change, the synchronized THz data will be picked out and stored in another file called pixeled file. In this file, every change of the fast flag will increase the column number where the THz data will be stored, and change of slow flag will increase the row number where it will be stored. As you may know, this file could plot the 360 degree THz map that the THz beam has swept. However, only 60 out of 360 degrees contains useful information, so in the third file carefully picks out the useful data that covers the area when the beam sweeps over the objective mirror. This file is also stored and called as mapped file. All of these are being completed while the scanning process and the values and the position information are used for displaying the image to the user real-time.

CHAPTER 8: IMAGING FOR CHARACTERIZATION

8.1 Coupling Efficiency Characterization

8.1.1 System Setup

A brass ball with 3/8" = 9.525 mm radii of curvature was first imaged as a demo target to evaluate the uniformity of the imaging across the field of view and how it fits the simulated coupling efficiency in the system analysis chapter.

The brass ball as shown in Figure 71 (a) is mounted to a 3-axis micro translation stage by a connecting rod purchased from Thorlabs as shown in figure (b). The assembly is attached to the objective mirror bracket with the multifunction bridge. The details are described in our system instrumentation chapter.

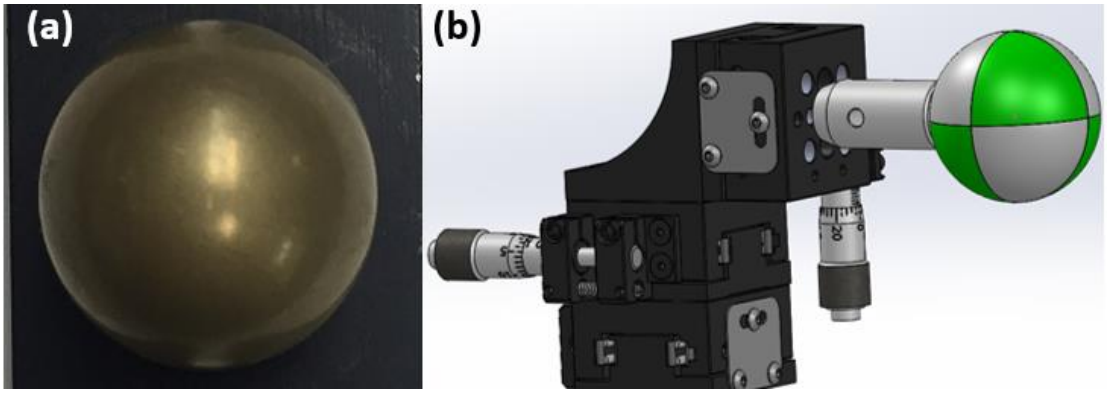

Figure 72. Mounting the target ball.

For this experiment, target alignment is crucial to the final imaging results. As we analyzed previously in the analysis chapter, the imaging quality is very sensitive to the misalignment. Here we have a few tricks that we can follow to make sure it is well aligned. First step, make sure you can see some signal reflected by the target ball with coarse adjustment of the translation stage. If you are not sure whether the read out value is real signal or background, just wave your hands between the target ball and mirror. If you can see obvious signal change, congrats, the detector

is picking up reflecting signal from the target. Second, by carefully fine adjustment of the translation stage, find a position where maximum value occurs. Third, rotate the mirror in φ direction by 10 degrees, and you will see signal drop. Adjust the translation stage in forward and backward direction to find the position where the readout closest to the previous value. The ball should now be well aligned and ready for testing. You can still use the same strategy to verify the position in our directions.

The electronic setup is described in details in the system instrumentation chapter. Here we just click the “Scan” button on the GUI and wait for the image to be displayed.

8.1.2 Imaging Results

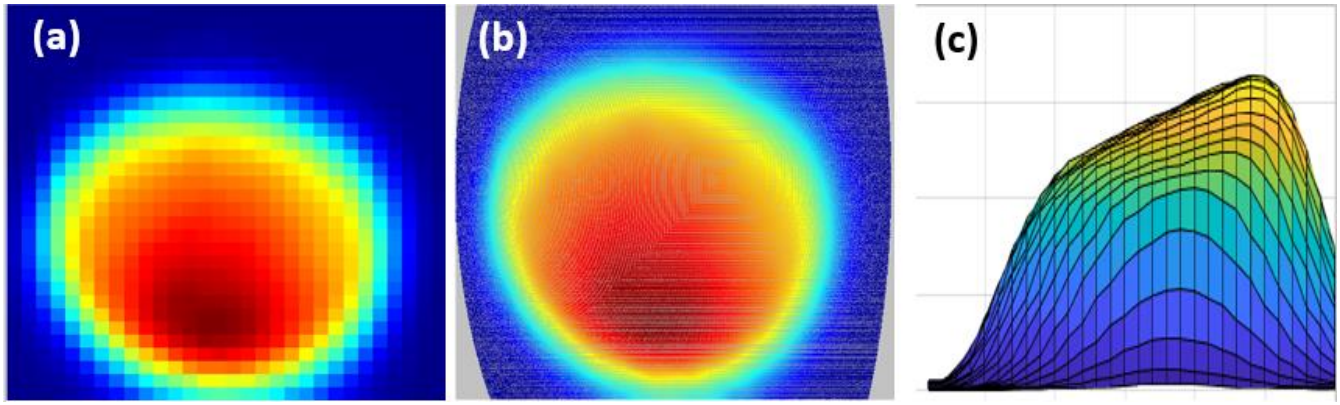

Figure 71. Imaging of a brass characterization ball

The raw data directly read from the “Mapped File” displays as it is in Figure 71 (a) when the scanning resolution is set to be 2 degrees for both axis. The resolution of the data is digitally raised by interpolation and mapped to a 3-D sphere surface and the image displays as in Figure 71 (b). From the 2D raw data and the registered image, we also see the great ease of the coordinates transformation of this setup compared to the previous version. Figure (c) is the side view of the raw data surf plot depending on the scan radius, which gives us a more intuitive grasp on the coupling efficiency.

8.1.3 Analysis

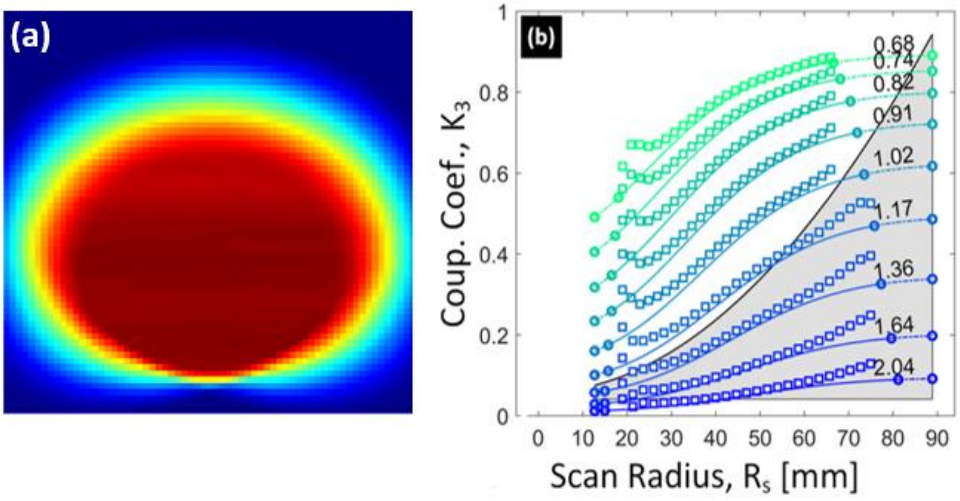

Figure 74. Review of coupling efficiency simulation results

Figure 74 helps to refresh the simulation results we had in our previous chapters with ASAP, quausioptics and physical optics. As Figure 71 (a) and (b) show us, the brass target ball yielded a relatively flat image across the whole field of view, and matches well with the ASAP simulation in Figure 74 (a). As in both the experiment data image and simulation results, we can see it is symmetric across the φ direction and has a maximum around the center line of the image, while the signal intensity generally increases as the beam scan radius increases, where larger R_s corresponds to increased collimated beam diameter and decreased collimated beam path length.

By comparing the Figure 71 (c) and Figure 74 (b), we can see in quausioptics and physical optics the coupling efficiency both increased monotonically across the whole scan radius change while the real measurement experienced a monotonically increase and then a monotonically decrease. And another point to note is at both far edge and near edge, the experiment data presents a fast drop towards the edges. This is likely caused by the beam truncation and edge current occurred at the edge. This drop is observed around the whole edge area.

Circled by the rapid intensity dropping area at the edge, a much flatter area stands out and matches extremely well with our simulation prediction. This proves the successful of our

simulation and as well as the system instrumentation and alignment accuracy. However, this also indicates that our precise imaging area is a little bit smaller than we expected because of the beam expansion while propagating. In future applications, we either can extend the precise imaging area by replacing the current objective OAP with one with bigger surface, or compensate it with a background calibration image. Another possible approach is to limit the interested imaging area to the flat region in order to get theoretical homogeneous signals everywhere. In this way, the imaging speed limit can also be increased by a few times. The alignment setup could be reused for all the following experiments in this chapter simply by changing the target ball without further tuning.

8.2 Spatial Resolution Characterization

8.2.1 Setup and Imaging Results

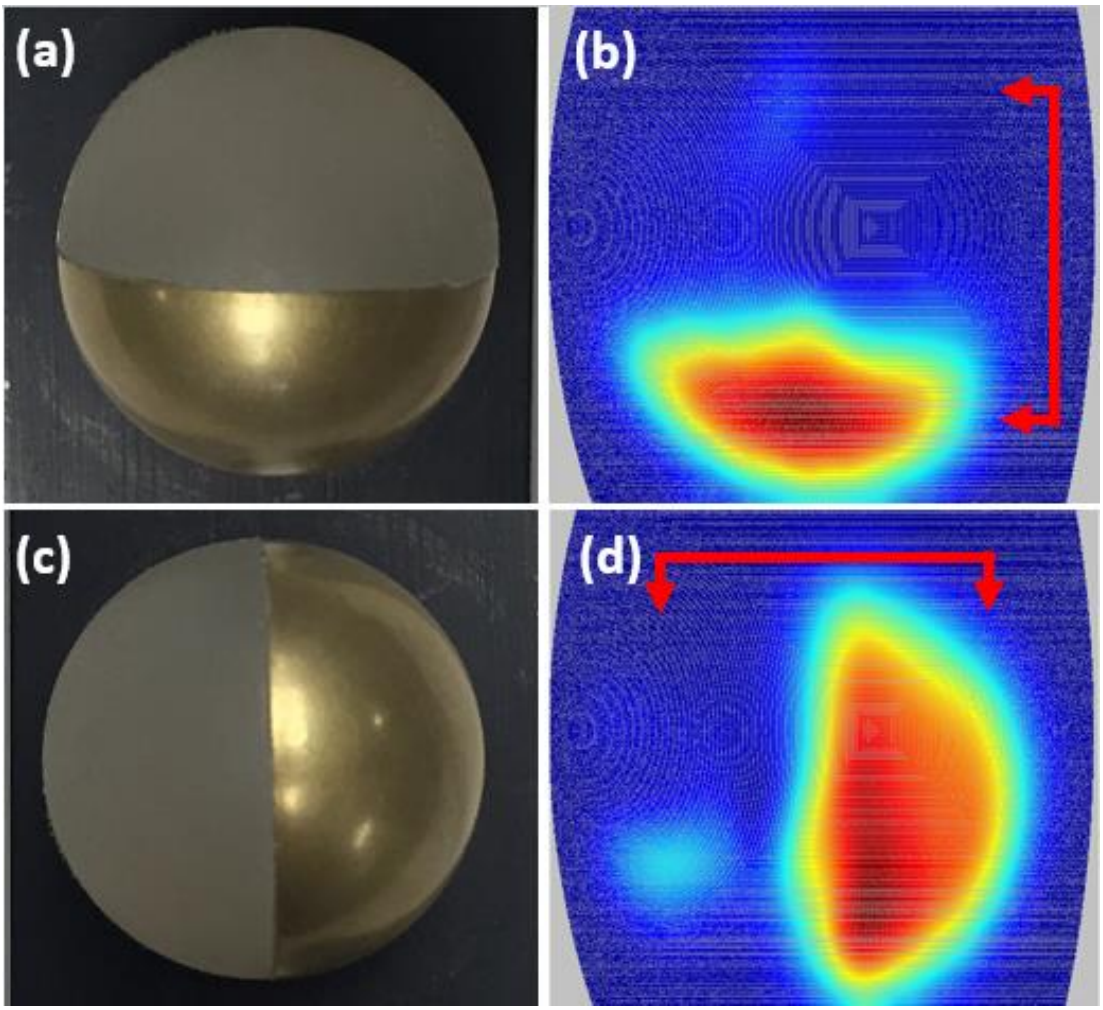

Figure 75. Imaging results of hemisphere target ball.

The two-hemisphere target was designed to characterize our spatial resolution of the optical system in both horizontal and vertical directions. The two hemispheres were cut from a brass ball and a polypropylene ball, both with radii of curvature of 3/8" = 9.525 mm. The target was assembled with the two hemispheres. The two-hemisphere target was first scanned with the joint seam appearing horizontally, and then with the joint seam vertically. The imaging is completed with the same GUI as above. 30 by 30 pixels were acquired with a step resolution of 2 degrees. The data is read and stored automatically. Figure 75 (a) and (c) are the visual image of the targets

with horizontal and vertical seam respectively and figure (b) and (d) are the registered 3-D imaging of the data accordingly.

8.2.2 Analysis

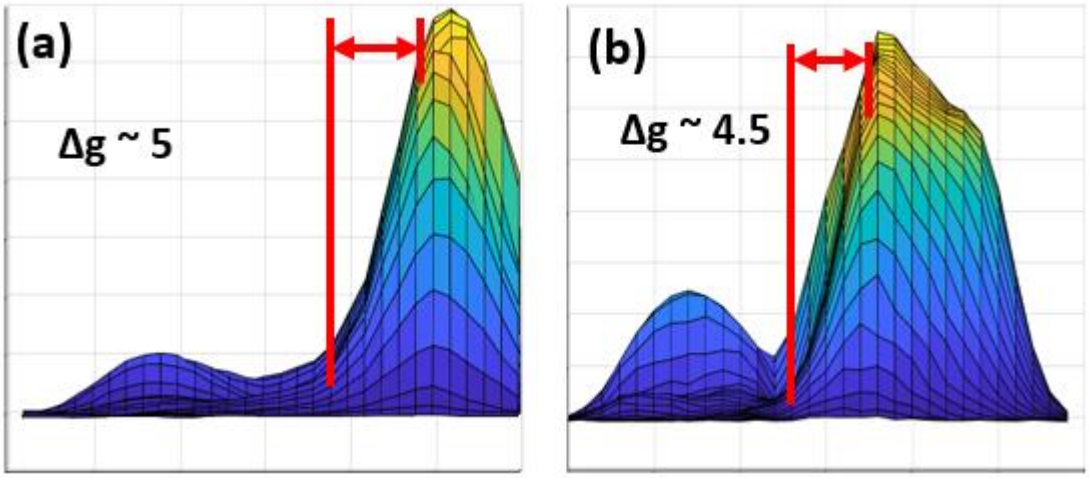

Figure 76. Knife-edge response measurement for hemisphere target. (a) Response measurement in θ direction; (b) Response measurement in φ direction.

Figure 76 plots the intensity profile of the imaging, roughly representing the step response of the scanned results perpendicular to joint of the hemispheres. The step response measurement very well verified our prediction. As in Figure 76 (a) and (b), the 10-90% rising resolution in both vertical and horizontal directions falls in 4 to 5 grids, 8 to 10 degrees, corresponding to a spot radius of 1 to 1.3 mm, which is close to our previous spot size calculations displayed in Figure 77, where we predicted as a range of [1.5 mm, 2.5mm] in quasioptical computation and 1.9 mm of radius in the Gaussian beam propagation. Figure 77 (a) is the review of spot size simulation in quasioptics and physical optics, (b) is the target, objective mirror part of the whole optics train simulation, where the spot size was noted.

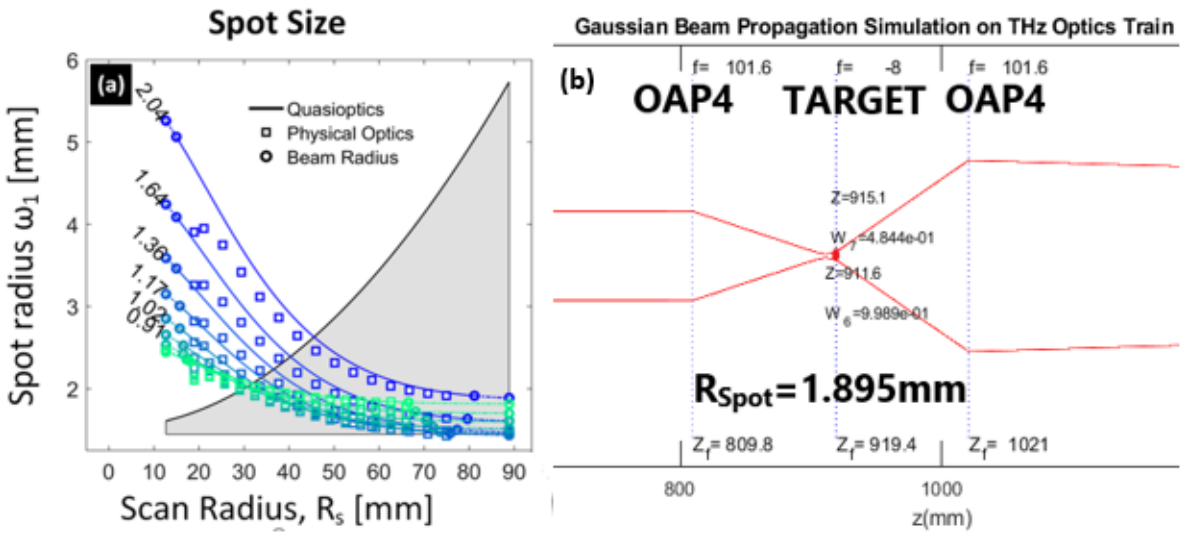

Figure 77. Review of spot size simulation results.

8.3 Corneal Phantom Imaging

8.3.1 Setup and Imaging and Results

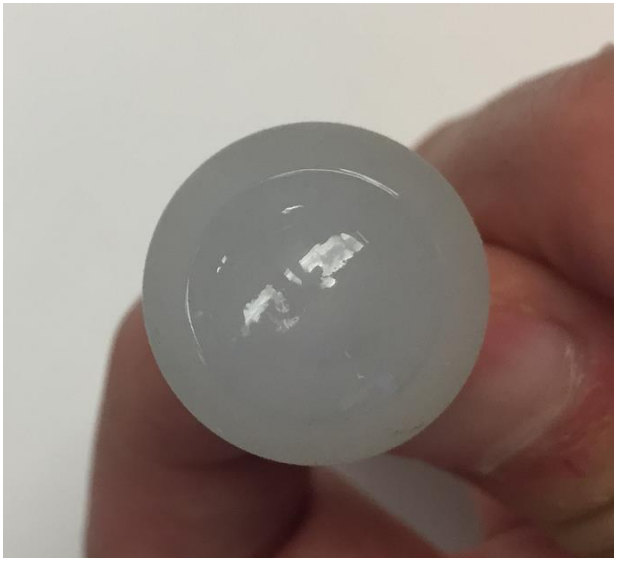

Figure 78. Visual image of the corneal phantom imaged.

A corneal phantom (soft contact lens 31% nelfilcon A, 69% water in isotonic phosphate-acetate buffered saline) with plastic background was imaged to explore the water content imaging capability of the system. The contact lens taken directly from the solution was positioned on the

polypropylene ball, the solution was left to evaporate under lab environment and images were acquired using our THz system. In Figure 78 is the visible image of the target, a contact lens attached to a polypropylene ball, with curvature radii of 3/8" = 9.525 mm.

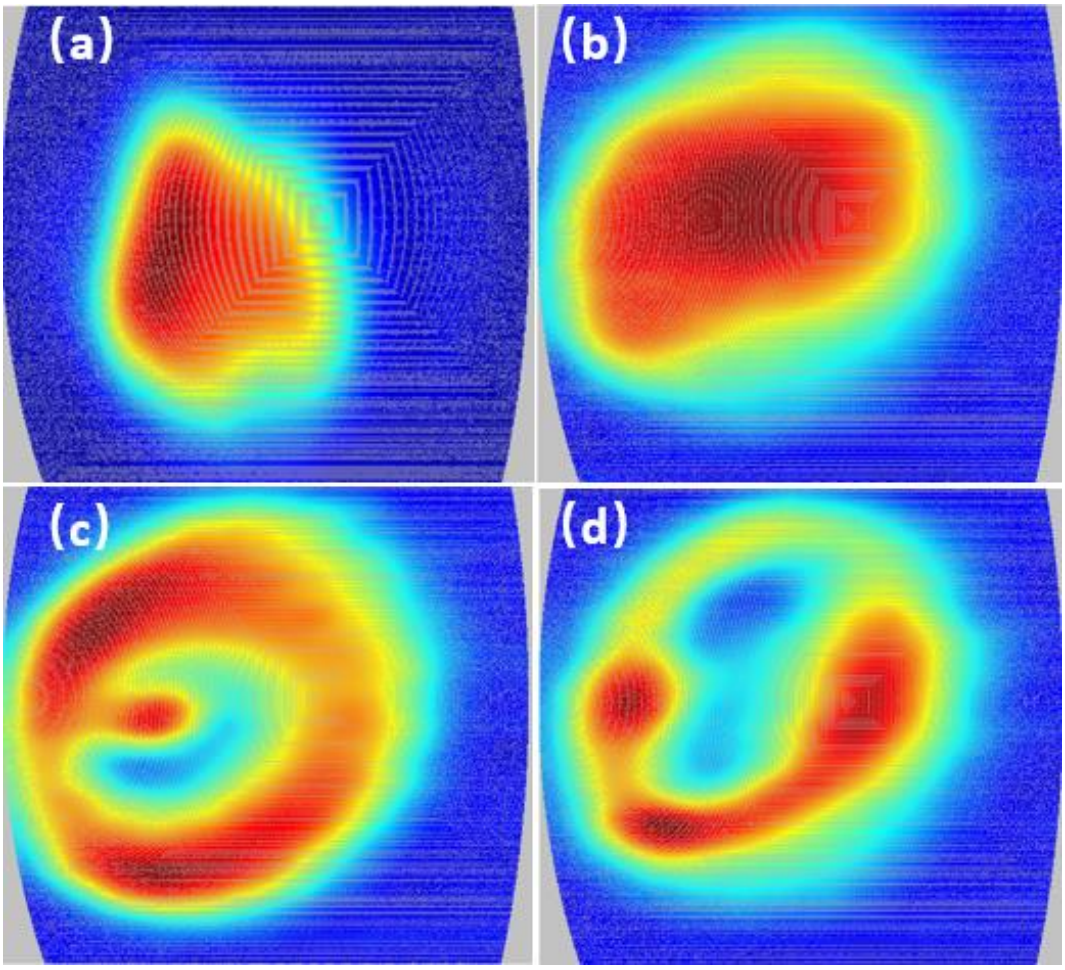

Figure 79. Images of corneal phantom.

(a) Phantom THz image taken right after being attached closely to the ball; (a) Phantom THz image taken 3 minutes after image (a); (c) Phantom THz image taken right after being attached to the ball with an air bubble inside; (a) Phantom THz image taken 3 minutes after image (c);

8.3.2 Analysis

In Figure 79 (a) is the THz image immediately taken after the contact lens was attached to the ball, perfectly tight; in figure (c), a bubble was intentionally left in the center area between the contact lens and the polypropylene ball, the ring-shape image very well reflected the existence of the bubble; figure (b) was taken 3 min after (a) was taken and figure (d) was taken 3 min after (c) was taken. The difference between (a) and (b) reflects the water content change, or the thickness change caused by water evaporation or both of the two factors. Comparing (c) and (d), we noticed the shift of the red color, which matches the possible migration of the water under the influence of gravity. In other words, this is a strong evidence that we might observed water migration on the contact lens with our system, however we are still unable to evaluate the water migration quantitively.

8.4 Speed Estimation

8.4.1 Mechanical Limit

Our rotary motor, RSW60C-E03, has a maximum speed of 1.25 rotations per second. As in our motion pattern, every step forward in φ direction takes a complete rotation in θ direction, so the time taken to complete 60/resolution rounds of rotation would be the time needed for a complete image. As in clinical scenario, we believe a 10 by 10 scanning would be informative enough for evaluation, so 8 seconds per image would be the maximum speed could be achieved. With modification of rotary stage motion pattern, for example , let the top motor rotates back and forth in θ direction only to cover the range where THz beams could reach the objective mirror, that is to say a 60 degree range, the scanning could be sped up by 6 times, which makes the speed limit to 1.3 s. Let's take a step further, if we only consider imaging the flat area that contains accurate image information, the speed limit could be within half seconds.

Considering the current technologies available, like galvometric or resonance mirrors, the complete scan could be done within microseconds. Video rate scanning could be easily achieved and the mechanical motion will never again be the limit of our system's scanning speed. It is likely the future speed limitation will shift to electronic side, like how fast your acquisition is and how fast your modulation of source could be, etc..

8.4.2 Electronical Limit

Since we realized the speed limit may lie in the electronic side, it is necessary to do a speed estimation from this perspective too. Experiments were designed for this purpose.

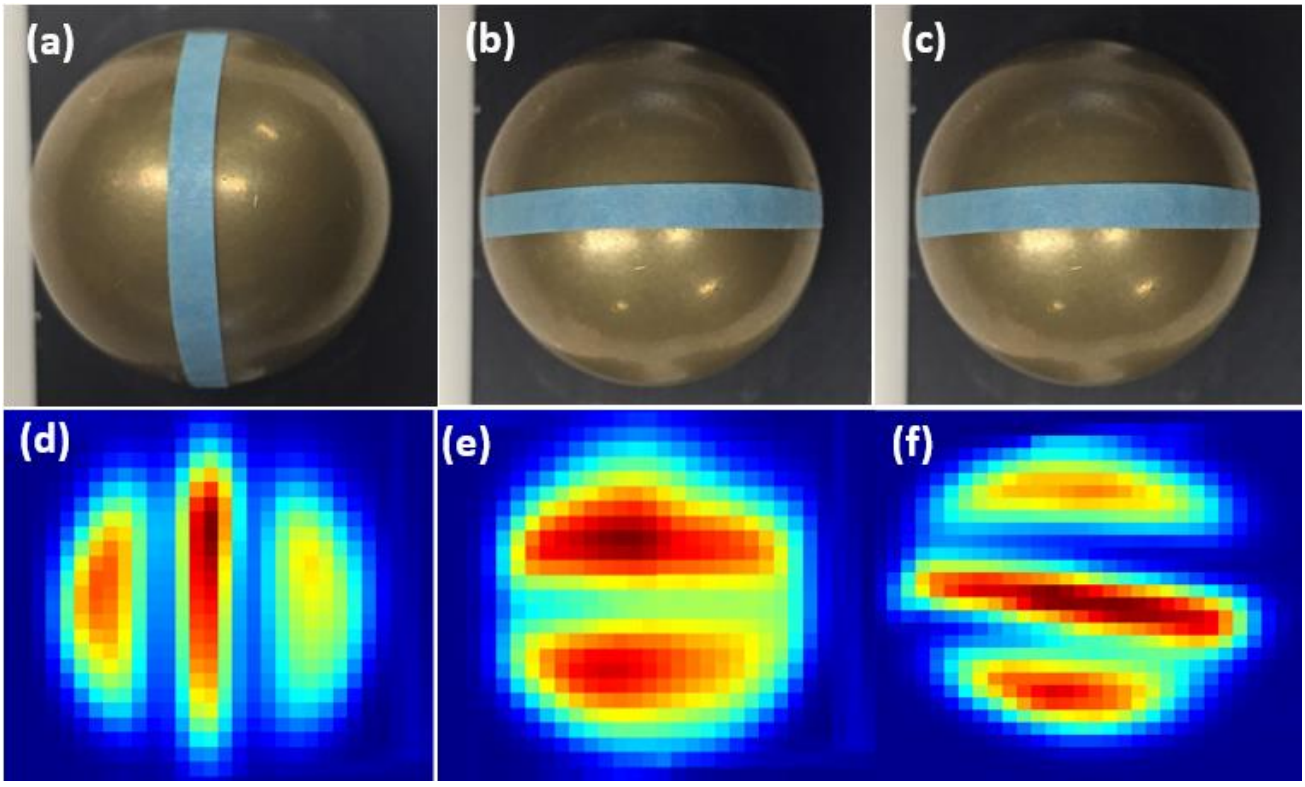

Figure 80. Comparison of imaging results under different scanning speed.

In this experiment, a 2 mm wide paper tape was positioned horizontally in the middle of the target and the image was taken; after that we repositioned the tape vertically in the middle of the target and took another image. In the first round of experiment, the motor speed was set to be 360 degrees per second, and two images are plotted as in Figure 80 (d) and (e). Figure (a) and (c) are the visual image of the target with according orientations.

Image of the brass ball with tape in the middle showed two dimmed strips adjacent to the highlighted center strip, which should be caused by the scattering effect when the THz beam sweeps over the geometrical abruption on the edges of the tape strip. However, in mage (e) we only see one dimmed strip which should be caused by the filer effect, or in other words, the

electronic limitation.

As in our setup, one motor moves one step in the horizontal direction, stops, waits for the second motor to finish one complete rotation and then move the next step. The second motor moves continuously in the vertical direction and data is acquired simultaneously. Considering limited signal sampling and possible signal filtering effect of the electronic setup in the system, especially adding on the fast scanning speed in the vertical direction which is 360 times faster than that in the horizontal direction, we may see decreased spatial resolution in the vertical direction when the scanning speed is set too high.

For the next step, we slowed down the motor to 180 degrees a second then 90 then 60.When the speed was set to 180 and 90, we started to see two dimmed strips appearing. When the speed was slowed down to 60 degrees per second, the two dimmed strips were clearly presented as in Figure 80 (c), which means our electronic speed limit is 60 degrees per second. In other words, with optimized motor motion pattern, the fastest scanning speed could achieved with our system is around 10 seconds. Even only imaging the flat imaging area, it would take at least 3 seconds to complete a scanning.

With faster electronic devices, we might be able to get much faster imaging speed. However, considering mechanical limit could be at the rate of kilohertz, it is still likely the imaging speed will be limited by the electronic devices. On the good side, a corneal imaging system as fast as a few frames per second is still reasonable to expect and will be good enough for clinical studies.

CHAPTER 9: CONCLUSION AND FUTURE WORK

9.1 Conclusions

First, a classical electromagnetic model of multi-layer dielectric slabs were adopted for simulation of cornea-THz interaction. Observed the reflective signal response based on variations of CTWC and CCT with sources centered at 100 GHz and 525 GHz respectively. The possibility of more accurate measurement combining magnitude and phase detection were also explored.

Second, this thesis explored the strengths and weaknesses of imaging with OAPs and found ways to use them correctly. Several basic setups were compared theoretically and verified experimentally. Symmetric compensated setup was proved to be useful in improving image qualities and different combinations of mirror focal length were crucial to confocality behavior and alignment sensitivity. Based the research, an optical design of a non-contact angular scanning imaging system was accomplished and fully simulated with ASAP. Much better image quality was achieved with this system compared to the previous system built by the group. Approaches of quasioptics, physical optics and Gaussian beam propagation methods were used independently for analysis of the system and they all had a good agreement.

Based on the optics design, a functioning THz imaging system was implemented afterwards. The electronic schematic of illumination source, detector and preliminary signal processing and data acquisition were explained. Carefully detailed mechanical design, machining and assembling of the system guaranteed the system to run as expected. Custom designed GUI enabled operators to control the system and acquire images with ease and efficiency.

System imaging quality and speed limit were characterized with preliminary images. The coupling efficiency of the system were characterized with a brass ball and verified our previous simulation results, proved the system has a homogenous energy coupling efficiency across the effective FOV. Images with strips-attached brass balls and knife-edge measurement with

hemisphere target ball characterized the spatial resolution to be around 1.3 mm with little distortion, agreed well with the predication made via different simulations. Images of cornea phantoms showed the capability of the system to identify abnormal geometry and water migration within the phantoms. The mechanical speed limit of the current system is 8 seconds per image and could be sped up to 1.3 seconds per frame with optimized motion pattern. The potential physical speed could reach a few kilo-frames per second with proper technologies, like galvometric and resonance mirrors. However, the electronic setup is limiting the current system speed to 10 seconds per frame with fine resolution. We believe this optical setup will be able to provide images at video rate with better mechanical and electronic equipment in the future.

9.2 Future Work

9.2.1 Speeding Up Further

As we noticed, the system was designed here as a proof of concept for a potential optical setup for fast imaging of the cornea. The instrumentation efforts were mostly made in validation of the optical setup. The scanning speed of the system is far from reaching its limit. Replacing the rotating motors with faster mechanical components is very promising to advance the system to the video-rate imaging club. However, considering the electronic limitations of the system, it is time consuming and expensive, so it could be saved for future researchers who have obtained good, convincing clinical data with the system and are fully funded and ready for really large scale of clinical trials.

For the current stage, it is much easier and cheaper to optimize the motor patterns and change the electronic settings of the current system to get an acceptable imaging speed for small scale of clinical trial. If we only scan within 60 degrees of the whole 360 degrees of space with the top mirror rotating back and forth, we are likely to easily increase the scanning speed by 6 times. Considering a 10 by 10 pixel scanning over the field of cornea, it is likely to reach a imaging speed of 1.3 seconds per image from the original speed of 8 seconds per image, given the maximum speed of the motors is 450 º /s. If it only takes 1~2 seconds to generate the map of the water content of the cornea, it would be applicable in most clinical settings.

9.2.2 Clinical Trials

It is necessary to have the system tested in a real ophthalmology clinic setting before any possible translation of this technology could come true. It is beneficial for understanding the unique constraints associated with operating THz components in the clinical environment.

Before taking this crucial step into the clinic, several preparations should be made. The first one is the above mentioned speed raising. Second, since the current setup of the system was only for imaging characterization with target balls, we need to think for how to accommodating a

human head for corneal imaging. We can simply remove the balance base plate and extend the distance between the big OAPs until it can allow a head in with the knob of the translation stage. Third, add an alignment assistant mechanism to this system, like a chin rest frame and visual camera for aligning.

With a pilot human trial to understand possible limitations of the system and possible iterations of system, a large-scale clinical trial on patients undergoing corneal graft surgery would be taken.

9.2.3 Phase Detection

As it in the EM modeling chapter showed us, it was very exciting to see the possibility of combining the measurement of magnitude and phase detection to get more accurate information on water content and hydration distribution modes. We will be pleased to assist our collaborators in Chalmers' university with their experiments. We will be helping them with the system assembling and possible modifications. We will also provide them the custom made glass tank for water-backing measurement for the tissues, in order to get a closer mimic of the cornea scenario.

9.3 Final Words

Because of the lack of accurate, direct, non-invasive methods for CTWC measurement, numerous corneal diseases associated with abnormal CTWC are being detected through visual assessment where the water content is sufficiently high to make the cornea appear cloudy. THz imaging technique offers an opportunity to diagnose the abnormal water content change at an early stage before it could be visually detected. Early detection will allow for early intervention and thus results in better patient outcome. If this comes to reality, it could be a revolutionary tool for the ophthalmology field.

Given the easy access to the corneal tissue and cornea's low variation and homogenous composition compared to other human tissues, it is a perfect research topic to test out the capabilities of THz imaging in medical filed. The progress made by the group in engineering the system to a quasi-testable equipment in clinic is quite inspiring. We are excited to see how this is going to turn out.

While system engineers try to develop feasible systems with current available sources and detectors, scientists and device engineers never stopped for inventing more advanced THz elements, like more powerful sources and low noise detector arrays with good responsivity. Whichever way people take, it is sure to benefit the whole field.

Another point, this time we happened to use THz for CTWC mapping and it showed us some hope, but it doesn't mean that we will be confined to this forever. We are still open to explore other possible applications for THz, feasible technologies for CTWC, and hence never stop the steps to use our knowledge and skills to make this a healthier and better world.

References:

[1] J.-H. Son, *Terahertz biomedical science and technology*. 2014.

[2] Saeedkia and Daryoosh, *Handbook of terahertz technology for imaging, sensing and communications || Optoelectronic techniques for the generation and detection of terahertz waves*, 1st Editio. WP Woodhead Publishing, 2013.

[3] H. A. Hafez, X. Chai, and A. Ibrahim, "Related content Intense terahertz radiation and their applications," *J. Phys. D Appl. Phys. Top. Rev. • OPEN ACCESS*, vol. 50, p. 43001, 2017.

[4] G. Dammertz *et al.*, "Development of a 140-ghz 1-mw continuous wave gyrotron for the w7-x stellarator," *IEEE Trans. Plasma Sci.*, vol. 30, no. 3, pp. 808–818, Jun. 2002.

[5] T. Idehara and S. P. Sabchevski, "Review Article Gyrotrons for High-Power Terahertz Science and Technology at FIR UF."

[6] B. Gorshunov *et al.*, "Terahertz BWO-Spectrosopy," *Int. J. Infrared Millimeter Waves*, vol. 26, no. 9, pp. 1217–1240, Sep. 2005.

[7] H. B. Zhang, K. Mitobe, and N. Yoshimura, "Conference Series OPEN ACCESS To cite this article: Artem N Perov et al," *J. Phys. Conf. Ser*, vol. 486, p. 12027, 2014.

[8] G. P. Gallerano, "OVERVIEW OF TERAHERTZ RADIATION SOURCES."

[9] V. A. Gorobets, B. F. Kuntsevich, and V. O. Petukhov, "Terahertz Gas Laser," in *2006 Joint 31st International Conference on Infrared Millimeter Waves and 14th International Conference on Teraherz Electronics*, 2006, pp. 218–218.

[10] L. Xu, C. A. Curwen, P. W. C. Hon, Q.-S. Chen, T. Itoh, and B. S. Williams, "Metasurface external cavity laser," *Appl. Phys. Lett.*, vol. 107, no. 22, p. 221105, Nov. 2015.

[11] L. Consolino, F. Cappelli, M. Siciliani de Cumis, and P. De Natale, "QCL-based frequency metrology from the mid-infrared to the THz range: a review," *Nanophotonics*, vol. 0, no. 0, Oct. 2018.

[12] Z. D. Taylor, E. R. Brown, J. E. Bjarnason, M. P. Hanson, and A. C. Gossard, "Resonant-optical-cavity photoconductive switch with 05% conversion efficiency and 10W peak power," *Opt. Lett.*, vol. 31, no. 11, p. 1729, Jun. 2006.

[13] N. M. Burford and M. O. El-Shenawee, "Review of terahertz photoconductive antenna technology," *Opt. Eng.*, vol. 56, no. 1, p. 010901, Jan. 2017.

[14] W.-D. Zhang, J. R. Middendorf, and E. R. Brown, "Demonstration of a GaAs-based 1550-nm continuous wave photomixer," *Appl. Phys. Lett.*, vol. 106, no. 2, p. 021119, Jan. 2015.

[15] N. T. Yardimci, S. Cakmakyapan, S. Hemmati, and M. Jarrahi, "A High-Power Broadband Terahertz Source Enabled by Three-Dimensional Light Confinement in a Plasmonic Nanocavity," *Sci. Rep.*, vol. 7, no. 1, p. 4166, Dec. 2017.

[16] N. T. Yardimci, S.-H. Yang, C. W. Berry, and M. Jarrahi, "High-Power Terahertz Generation Using Large-Area Plasmonic Photoconductive Emitters," *IEEE Trans. Terahertz Sci. Technol.*, vol. 5, no. 2, pp. 223–229, Mar. 2015.

[17] G. Danion, C. Hamel, L. Frein, F. Bondu, G. Loas, and M. Alouini, "Dual frequency laser with two continuously and widely tunable frequencies for optical referencing of GHz to THz beatnotes," *Opt. Express*, vol. 22, no. 15, p. 17673, Jul. 2014.

[18] J.-H. Son, *Terahertz biomedical science and technology*, 1st Editio. CRC Press.

[19] K. Nowak, P. P. Jarzab, and E. F. Plinski, "Limitations of the terahertz photomixer," *Rev. Sci. Instrum.*, vol. 82, no. 12, p. 123113, Dec. 2011.

[20] "Terahertz photoconductive switches | Hamamatsu Photonics." [Online]. Available: https://www.hamamatsu.com/us/en/product/lasers/laser-related-products/terahertz-photoconductive-switches/index.html. [Accessed: 24-Oct-2018].

[21] "Photoconductive Switches : TOPTICA Photonics." [Online]. Available: https://www.toptica.com/products/terahertz-systems/time-domain/photoconductive-

switches/. [Accessed: 24-Oct-2018].
[22] O. Momeni and E. Afshari, “High Power Terahertz and Millimeter-Wave Oscillator Design: A Systematic Approach,” *IEEE J. Solid-State Circuits*, vol. 46, no. 3, p. 583, 2011.
[23] J. M. Chamberlain, R. E. Miles, C. E. Collins, and D. P. Steenson, “Introduction to Terahertz Solid-State Devices,” in *New Directions in Terahertz Technology*, Dordrecht: Springer Netherlands, 1997, pp. 3–27.
[24] P. Zhao, D. Woolard, M. Lasater, C. T. Kelley, and R. Trew, “Terahertz-Frequency Quantum Oscillator Operating in the Positive Differential Resistance Region.”
[25] C. M. M. O’Sullivan, J. A. Murphy, and Society of Photo-optical Instrumentation Engineers., *Field guide to terahertz sources, detectors, and optics*. SPIE, 2012.
[26] Z. D. Taylor, “Active THz Imaging for Medical Applications,” 2009.
[27] “Terahertz TDS (pulsed) and FDS imaging | TeraSense.” [Online]. Available: http://terasense.com/applications/tds-fds-systems/. [Accessed: 31-Oct-2018].
[28] R. J. B. Dietz *et al.*, “All fiber-coupled THz-TDS system with kHz measurement rate based on electronically controlled optical sampling,” *Opt. Lett.*, vol. 39, no. 22, p. 6482, Nov. 2014.
[29] S. Sung *et al.*, “Fast-scanning THz medical imaging system for clinical application,” 2012, vol. 8496, p. 84960S.
[30] P. Helminger, J. K. Messer, and F. C. De Lucia, “Continuously tunable coherent spectroscopy for the 0.1–1.0-THz region,” *Appl. Phys. Lett.*, vol. 42, no. 4, pp. 309–310, Feb. 1983.
[31] P. Tewari *et al.*, “In vivo terahertz imaging of rat skin burns,” *J. Biomed. Opt.*, vol. 17, no. 4, p. 040503, 2012.
[32] Z. D. Taylor *et al.*, “Reflective terahertz imaging of porcine skin burns,” *Opt. Lett.*, vol. 33, no. 11, p. 1258, Jun. 2008.
[33] U. Frisk *et al.*, “The Odin satellite,” *Astron. Astrophys.*, vol. 402, no. 3, pp. L27–L34, May 2003.
[34] N. C. Administrator, “Superconducting Submillimeter-Wave Limb-Emission Sounder (SMILES),” 2015.
[35] S. Barbieri *et al.*, “Coherent sampling of active mode-locked terahertz quantum cascade lasers and frequency synthesis,” *Nat. Photonics*, vol. 5, no. 5, pp. 306–313, May 2011.
[36] K.-E. (Kai-E. Peiponen, A. Zeitler, and M. Kuwata-Gonokami, *Terahertz spectroscopy and imaging*. Springer, 2013.
[37] R. Appleby and R. N. Anderton, “Millimeter-Wave and Submillimeter-Wave Imaging for Security and Surveillance,” *Proc. IEEE*, vol. 95, no. 8, pp. 1683–1690, Aug. 2007.
[38] J. F. Federici *et al.*, “THz imaging and sensing for security applications-explosives, weapons and drugs Related content THz imaging and sensing for security applications-explosives, weapons and drugs,” *Semicond. Sci. Technol*, vol. 20, pp. 266–280, 2005.
[39] “Terahertz security body scanner | TeraSense.” [Online]. Available: http://terasense.com/products/body-scanner/. [Accessed: 05-Nov-2018].
[40] “TSA to test technology for long-range passenger screening | Business | postbulletin.com.” [Online]. Available: https://www.postbulletin.com/news/business/tsa-to-test-technology-for-long-range-passenger-screening/article_a07ea7c8-bf31-5f03-b064-4f487ed806fa.html. [Accessed: 05-Nov-2018].
[41] B. B. Hu and M. C. Nuss, “Imaging with terahertz waves,” 1995.
[42] A. J. Fitzgerald *et al.*, “Terahertz imaging of breast cancer, a feasibility study,” in *Infrared and Millimeter Waves, Conference Digest of the 2004 Joint 29th International Conference on 2004 and 12th International Conference on Terahertz Electronics, 2004.*, pp. 823–824.
[43] R. M. Woodward, V. P. Wallace, D. D. Arnone, E. H. Linfield, and M. Pepper, “Terahertz pulsed imaging of skin cancer in the time and frequency domain.,” *J. Biol. Phys.*, vol. 29, no. 2–3, pp. 257–9, Jun. 2003.

[44] Y. C. Sim, J. Y. Park, K.-M. Ahn, C. Park, and J.-H. Son, “Terahertz imaging of excised oral cancer at frozen temperature,” *Biomed. Opt. Express*, vol. 4, no. 8, p. 1413, Aug. 2013.
[45] G. G. Hernandez-Cardoso *et al.*, “Terahertz imaging for early screening of diabetic foot syndrome: A proof of concept,” *Sci. Rep.*, vol. 7, no. 1, p. 42124, Dec. 2017.
[46] N. Bajwa *et al.*, “Non-invasive terahertz imaging of tissue water content for flap viability assessment,” *Biomed. Opt. Express*, vol. 8, no. 1, p. 460, Jan. 2017.
[47] S. Sung *et al.*, “THz Imaging System for in vivo Human Cornea,” *IEEE Trans. Terahertz Sci. Technol.*, vol. 8, no. 1, pp. 27–37, Jan. 2018.
[48] S. Sung *et al.*, “Optical System Design for Noncontact, Normal Incidence, THz Imaging of in vivo Human Cornea,” *IEEE Trans. Terahertz Sci. Technol.*, vol. 8, no. 1, pp. 1–12, Jan. 2018.
[49] Z. D. Taylor *et al.*, “THz and mm-Wave Sensing of Corneal Tissue Water Content: In Vivo Sensing and Imaging Results,” *IEEE Trans. Terahertz Sci. Technol.*, vol. 5, no. 2, pp. 184–196, Mar. 2015.
[50] Z. D. Taylor *et al.*, “THz and mm-Wave Sensing of Corneal Tissue Water Content: Electromagnetic Modeling and Analysis,” *IEEE Trans. Terahertz Sci. Technol.*, vol. 5, no. 2, pp. 170–183, Mar. 2015.
[51] D. Bennett *et al.*, “Assessment of corneal hydration sensing in the terahertz band: *in vivo* results at 100 GHz,” *J. Biomed. Opt.*, vol. 17, no. 9, p. 0970081, Sep. 2012.
[52] B. Wright and C. J. Connon, Eds., *Corneal Regenerative Medicine*, vol. 1014. Totowa, NJ: Humana Press, 2013.
[53] B. Zuberbuhler, S. Tuft, D. Gartry, and D. Spokes, *Corneal Surgery*. Berlin, Heidelberg: Springer Berlin Heidelberg, 2013.
[54] L. A. Remington, *Clinical anatomy and physiology of the visual system*, 3rd Editio. Elsevier/Butterworth-Heinemann, 2012.
[55] K. M. Meek and C. Knupp, “Corneal structure and transparency.,” *Prog. Retin. Eye Res.*, vol. 49, pp. 1–16, Nov. 2015.
[56] D. W. C. Lorenzetti, M. H. Uotila, N. Parikh, and H. E. Kaufman, “Central Cornea Guttata: Incidence in the General Population,” *Am. J. Ophthalmol.*, vol. 64, no. 6, pp. 1155–1158, Oct. 1967.
[57] T. Reinhard and F. Larkin, Eds., *Cornea and External Eye Disease*. Berlin, Heidelberg: Springer Berlin Heidelberg, 2008.
[58] J. Hjortdal, I. B. Pedersen, S. Bak-Nielsen, and A. Ivarsen, “Graft Rejection and Graft Failure After Penetrating Keratoplasty or Posterior Lamellar Keratoplasty for Fuchs Endothelial Dystrophy,” *Cornea*, vol. 32, no. 5, pp. e60–e63, May 2013.
[59] M. C. Bartels, I. I. N. Doxiadis, T. P. Colen, and W. H. Beekhuis, “Long-term outcome in high-risk corneal transplantation and the influence of HLA-A and HLA-B matching.,” *Cornea*, vol. 22, no. 6, pp. 552–6, Aug. 2003.
[60] M. Kaur, A. Tomar, F. Shaikh, R. Falera, L. M. S. Bageshwar, and J. S. Titiyal, “Sealing clear corneal incisions in cataract surgery,” *Expert Rev. Ophthalmol.*, vol. 13, no. 1, pp. 47–55, Jan. 2018.
[61] I. A. Chaudhry, “Measurement of central corneal thickness in health and disease.,” *Saudi J. Ophthalmol. Off. J. Saudi Ophthalmol. Soc.*, vol. 23, no. 3–4, pp. 179–80, Oct. 2009.
[62] M. J. Doughty and M. L. Zaman, “Human Corneal Thickness and Its Impact on Intraocular Pressure Measures: A Review and Meta-analysis Approach,” *Surv. Ophthalmol.*, vol. 44, no. 5, pp. 367–408, Mar. 2000.
[63] E. Hekimoglu, M. K. Erol, D. Toslak, D. Turgut Coban, B. Doğan, and O. Yucel, “Comparison of Measurement of Central Corneal Thickness with Spectral Domain Optical Coherence Tomography and Standard Ultrasonic Pachymeter in Premature Infants.,” *J. Ophthalmol.*, vol. 2015, p. 129269, Jul. 2015.

[64] M. Ayala and R. Strandås, “Accuracy of optical coherence tomography (OCT) in pachymetry for glaucoma patients,” *BMC Ophthalmol.*, vol. 15, no. 1, p. 124, Dec. 2015.
[65] N. J. Bauer, J. P. Wicksted, F. H. Jongsma, W. F. March, F. Hendrikse, and M. Motamedi, “Noninvasive assessment of the hydration gradient across the cornea using confocal Raman spectroscopy.,” *Invest. Ophthalmol. Vis. Sci.*, vol. 39, no. 5, pp. 831–5, Apr. 1998.
[66] J. YTTEBORG and C. H. DOHLMAN, “Corneal Edema and Intraocular Pressure,” *Arch. Ophthalmol.*, vol. 74, no. 4, p. 477, Oct. 1965.
[67] M. Bechmann, M. J. Thiel, B. Roesen, S. Ullrich, M. W. Ulbig, and K. Ludwig, “Central corneal thickness determined with optical coherence tomography in various types of glaucoma,” *Br J Ophthalmol*, vol. 84, pp. 1233–1237, 2000.
[68] E. Ozyol and P. Özyol, “Comparison of central corneal thickness with four noncontact devices: An agreement analysis of swept-source technology.,” *Indian J. Ophthalmol.*, vol. 65, no. 6, pp. 461–465, Jun. 2017.
[69] B. T. Fisher, K. A. Masiello, M. H. Goldstein, and D. W. Hahn, “Assessment of transient changes in corneal hydration using confocal Raman spectroscopy.,” *Cornea*, vol. 22, no. 4, pp. 363–70, May 2003.
[70] S. W. Jeon, M. A. Shure, A. M. Rollins, and D. Huang, “Corneal hydration imaging using dual-wavelength optical coherence tomography,” 2004, p. 113.
[71] H. Aurich, C. Wirbelauer, J. Jaroszewski, C. Hartmann, and D. T. Pham, “Continuous measurement of corneal dehydration with online optical coherence pachymetry.,” *Cornea*, vol. 25, no. 2, pp. 182–4, Feb. 2006.
[72] D. Xia *et al.*, “Hydrated Human Corneal Stroma Revealed by Quantitative Dynamic Atomic Force Microscopy at Nanoscale,” *ACS Nano*, vol. 8, no. 7, pp. 6873–6882, Jul. 2014.
[73] “Handheld corneal hydrometer provides accurate measurement of refractive index.” [Online]. Available: https://www.healio.com/ophthalmology/cataract-surgery/news/print/ocular-surgery-news-europe-edition/%7B7a9342c6-997a-4bfc-9477-70088b9e9bbe%7D/handheld-corneal-hydrometer-provides-accurate-measurement-of-refractive-index. [Accessed: 23-Nov-2018].
[74] N. Bajwa, “In vivo terahertzimaging of tissue edemafor burn wound and flap assessment,” UCLA, 2016.
[75] J. O. Hjortdal, L. Erdmann, and T. Bek, “Fourier analysis of video-keratographic data. A tool for separation of spherical, regular astigmatic and irregular astigmatic corneal power components.,” *Ophthalmic Physiol. Opt.*, vol. 15, no. 3, pp. 171–85, May 1995.
[76] J. Schwiegerling and J. E. Greivenkamp, “Using corneal height maps and polynomial decomposition to determine corneal aberrations.,” *Optom. Vis. Sci.*, vol. 74, no. 11, pp. 906–16, Nov. 1997.
[77] R. A. Applegate and H. C. Howland, “Noninvasive measurement of corneal topography,” *IEEE Eng. Med. Biol. Mag.*, vol. 14, no. 1, pp. 30–42, 1995.
[78] D. A. G. Bruggeman, “Berechnung verschiedener physikalischer Konstanten von heterogenen Substanzen. I. Dielektrizitätskonstanten und Leitfähigkeiten der Mischkörper aus isotropen Substanzen,” *Ann. Phys.*, vol. 416, no. 7, pp. 636–664, Jan. 1935.
[79] G. A. Niklasson, C. G. Granqvist, and O. Hunderi, “Effective medium models for the optical properties of inhomogeneous materials,” *Appl. Opt.*, vol. 20, no. 1, p. 26, Jan. 1981.
[80] J. Xu, K. W. Plaxco, S. J. Allen, J. E. Bjarnason, and E. R. Brown, “0.15–3.72THz absorption of aqueous salts and saline solutions,” *Appl. Phys. Lett.*, vol. 90, no. 3, p. 031908, Jan. 2007.
[81] J. A. Murphy, “Distortion of a simple Gaussian beam on reflection from off-axis ellipsoidal mirrors,” *Int. J. Infrared Millimeter Waves*, vol. 8, no. 9, pp. 1165–1187, Sep. 1987.

[82] D. B. Bennett *et al.*, “Terahertz sensing in corneal tissues,” *J. Biomed. Opt.*, vol. 16, no. 5, p. 057003, May 2011.
[83] “Characterization of a Gaussian Laser Beam using a knife edge.”
[84] “Laser Scanning Confocal Microscopy | MicroscopyU.” [Online]. Available: https://www.microscopyu.com/tutorials/laser-scanning-confocal-microscopy. [Accessed: 08-Dec-2018].
[85] S. A. Self, “Focusing of spherical Gaussian beams,” *Appl. Opt.*, vol. 22, no. 5, p. 658, Mar. 1983.
[86] D. Purves *et al.*, “Types of Eye Movements and Their Functions,” 2001.
[87] “WR1.5ZBD.” [Online]. Available: https://www.vadiodes.com/en/products/detectors?id=123. [Accessed: 09-Dec-2018].